REAL TIME OPTICAL OBSERVATION OF THE SYNTHESIS OF NOVEL 2D MATERIALS AND INVESTIGATION OF THEIR FUNDAMENTAL PROPERTIES

A DISSERTATION SUBMITTED TO

THE GRADUATE SCHOOL OF ENGINEERING AND SCIENCE

OF BILKENT UNIVERSITY

IN PARTIAL FULFILLMENT OF THE REQUIREMENTS FOR

THE DEGREE OF

DOCTOR OF PHILOSOPHY

IN

MATERIALS SCIENCE AND NANOTECHNOLOGY

By

Hamid Reza Rasouli

March 2021

Real time optical observation of the synthesis of novel 2D materials and investigation of their fundamental properties
By Hamid Reza Rasouli
March 2021

We certify that we have read this dissertation and that in our opinion it is fully adequate, in scope and in quality, as a dissertation for the degree of Doctor of Philosophy.

Talip Serkan Kasırga(Advisor)

Selçuk Yerci

Serim Kayacan İlday

Kibum Kang

Fatih Ömer İlday

Approved for the Graduate School of Engineering and Science:

Ezhan Karaşan
Director of the Graduate School

ABSTRACT

REAL TIME OPTICAL OBSERVATION OF THE SYNTHESIS OF NOVEL 2D MATERIALS AND INVESTIGATION OF THEIR FUNDAMENTAL PROPERTIES

Hamid Reza Rasouli
Ph.D. in materials science and nanotechnology
Advisor: Talip Serkan Kasırga
March 2021

Two-dimensional transition metal dichalcogenide (2D TMDC) with superb physical and chemical properties, used as the active material for various devices. The on-going primary focus is their reliable high-throughput synthesis using processes compatible with the current semiconductor technology. At present, among the common approaches, chemical vapor deposition (CVD) has been considered as the most promising method for preparing large-area high-quality 2D materials. However, the lack of *in-situ* information during the growth in conventional CVD systems, makes it impractical to realize high-temperature phenomena. In this thesis, we developed a novel CVD chamber that allows real time optical observation and control of the crystal growth. Using this new CVD method, which we call real time optical-CVD, RTO-CVD in short, we elaborated the involved mechanisms in salt-assisted synthesis of TMDCs and their vertical/lateral heterostructures. Through direct visualization of WSe_2 monolayer growth, we identified that both vapour-solid-solid and vapour-liquid-solid growth routes are in an interplay. Then, we focused our attention to synthesize novel 2D materials such as V_2O_3 and K-MnO_2 nanosheets. We succeeded synthesis route in favor of high-quality single-crystalline V_2O_3 nanoplates whose 2D characteristic allows us to study their peculiar electrical and physical properties such as metal-insulator transition (MIT) and supercritical state. The electrical properties of both as-grown and transferred V_2O_3 crystals were investigated with respect to the V_2O_3 phase-stability diagram. We observed emergence of a novel crystal structure upon electron beam heating in selected area electron diffraction (SAED) experiments and correlated it to the supercritical state by means of high-temperature Raman spectroscopy. Finally, we introduced large-area ultra-thin layered MnO_2 crystals, spontaneously intercalated by potassium ions during the synthesis. The

charge transport in 2D K-MnO_2 devices was shown to be dominated by the in-plane ionic conductivity through the motion of hydrated K ions in the interlayer space. The K-MnO_2 crystals exhibited reversible layered-to-spinel phase transition accompanied by an optical contrast change based on the electrical and optical modulation of the potassium and the interlayer water concentration. We used the electric-field driven ionic motion in K-MnO_2 devices to demonstrate the memristive properties and elucidated the resistance-switching mechanisms via real-time analyses upon the measurements. K-MnO_2 memristors were artificially able to emulate neuromorphic synapse-like behaviors, namely short and long-term potentiation/depression as well as ionic coupling effects.

Keywords: 2D Materials, Transition Metal Dichalcogenide, CVD Growth, *in-situ* Analysis, V_2O_3 Nanoplate, K-MnO_2 Birnessite, 2D Memristors, Synaptic Emulation.

ÖZET

YENİ 2D MALZEMELERİN SENTEZİNİN GERÇEK ZAMANLI OPTİK GÖZLEMİ VE TEMEL ÖZELLİKLERİNİN İNCELENMESİ

Hamid Reza Rasouli
Malzeme bilimi ve Nanoteknoloji, Doktora
Tez Danışmanı: Talip Serkan Kasırga
Mart 2021

İki boyutlu geçiş metali kalkojenleri(GMK), üstün fiziksel ve kimyasal özellikleri ile çeşitli uygulama potansiyeline sahiptirler. Günümüzde bu malzemelerin elde edilmesinde birincil odak noktası, mevcut yarı iletken teknolojisiyle uyumlu işlemleri kullanan tekrarlanabilir ve yüksek verimli sentezleridir. Halihazırda, geniş alanlı ve yüksek kalitede iki boyutlu malzemeler hazırlamak için, kimyasal buhar biriktirme (KBB), yaygın yaklaşımlar arasında en umut verici yöntem olarak kabul edilmektedir. Ancak, büyüme esnasında gerçek zamanlı olarak büyütme bilgisinin eksikliği, geleneksel KBB sistemlerini yüksek sıcaklık olaylarının incelenmesinde kullanışsız kılmaktadır. Bu tezde, kristal büyümesinin gerçek zamanlı optik gözlemine ve kontrolüne olanak sağlayan yeni bir KBB haznesi geliştirdik. Gerçek zamanlı optik KBB, kısaca GZO-KBB olarak adlandırdığımız bu yeni KBB yöntemini kullanarak, GMDC'lerin tuz destekli sentezinde ve dikey/yatay heteroyapılarında devreye giren mekanizmaları ayrıntılarıyla inceledik. WSe_2 tek katmanlı büyümesinin doğrudan görüntülenmesiyle, hem buhar-katı-katı hem de buhar-sıvı-katı büyüme yollarının karşılıklı etkileşim içinde olduğunu saptadık. Ardından, V_2O_3 ve K-MnO_2 nanosheet gibi yeni iki boyutlu malzemeleri sentezlemeye odaklandık. İki boyut karakteristiği ile metal-yalıtkan geçişi (MYG) ve süperkritik durum gibi sıradışı elektriksel ve fiziksel özellikleri üzerine çalışmamızı sağlayan yüksek kalite tek kristalli V_2O_3 nanoplatlarını sentezlemeyi başardık. Hem büyütülmüş hem de aktarılmış V_2O_3 kristallerinin elektriksel özellikleri, V_2O_3 faz-kararlılık şemasına göre incelendi. Seçili alan elektron kırınımı (SAEK) deneylerinde, elektron ışın ısıtması üzerinden yeni kristal yapılarının oluşumunu gözlemledik ve bunu yüksek sıcaklık Raman spektroskopisi aracılığıyla süperkritik durumla ilişkilendirdik. Son olarak, geniş alanlı, ultra-ince katmanlı MnO_2 kristallerini, sentez sırasında

anlık olarak potasyum iyonları ekleyerek sunduk. İki boyutlu K-MnO_2 cihazlarındaki yük aktarımında, ara katmanda hidratlanmış K iyonlarının hareketi ile düzlem içi iyonik iletkenliğin baskın olduğu gösterildi. K-MnO_2 kristalleri, potasyumun elektriksel ve optik modülasyonuna ve ara tabaka su konsantrasyonuna dayalı bir optik kontrast değişiminin eşlik ettiği tersine çevrilebilir katmandan spinele faz geçişi sergiledi. K-MnO_2 cihazlarında elektrik alanı tahrikli iyonik hareketi, hafıza özelliklerini göstermek için kullandık ve ölçümler üzerine gerçek zamanlı analizlerle direnç-anahtarlama mekanizmalarını açıkladık. K-MnO_2 memristörleri, yapay nöromorfik sinaps benzeri davranışları, yani kısa ve uzun vadeli güçlendirme/zayıflatma ve iyonik eşleşme etkileri sergilediler.

Anahtar sözcükler: İki Boyutlu Malzemeler, Geçiş Metal Dikalkojenit, KBB Büyümesi, Yerinde Analiz, V_2O_3 Nanoplat, K-MO_2 Birnessit, İki-boyutlu Memristörler, Sinaptik Emülasyon.

Acknowledgement

First and foremost, praises and thanks to the God, the Almighty, for His showers of blessings throughout my PhD life.

I would like to express my deep and sincere gratitude to my research supervisor, Prof. Dr. Talip Serkan Kasırga for giving me the opportunity to do research and providing invaluable guidance throughout this research. I have been extremely lucky to have a supervisor who cared so much about my work, responded to my questions and queries so promptly. It was a great privilege and honor to work and study under his guidance. I wish to warmly appreciate the members of my dissertation committee: Prof. Selçuk Yerci, Prof. Serim Kayacan İlday, Prof. Kibum Kang and Prof. Fatih Ömer İlday for generously offering their time, support, guidance through the preparation and review of this document. Your discussions, ideas, and feedbacks have been absolutely constructive. I am greatly grateful to my collaborators for lending me their expertise and intuition to my scientific and technical problems, especially Prof. Kibum Kang and his research group at KAIST university, who provided experimental supports for K-MnO_2 study. I would like to acknowledge my friends and research colleagues, specifically Naveed Mehmood and Ali Sheraz for their valuable experimental contribution in SCM lab. I sincerely appreciate Prof. Volkan Demir, the director of UNAM and all the administration staff and operation team for their support and providing me such a fantastic environment to do research. I gratefully acknowledge the funding received during my PhD from Scientific and Technological Research Council of Turkey (TÜBİTAK) for the 1001-grants (116M226 and 118F061) and 1002 Hızli Destek Program that I granted as the principal investigator.

I am extremely grateful to my parents for their love, prayers, caring and sacrifices for educating and preparing me for my future. To my brother and sister, my father, mother and brother-in-law for their unconditional love and support. Finally, of course, is my rock, my inspiration, my lovely wife Mandana Aberoumand and my son Ariyo Rasouli who have made countless sacrifices to help me get to this point. Without you none of this would ever have been possible. She stood by me through all my ups and downs, constantly encouraged me while facing difficulties. You are my angel making every single moment of my life astonishing.

To the soul of this work

my life, my wife

Contents

List of Figures

List of Tables

Chapter 1

Introduction

Two-dimensional (2D) materials have attracted extensive research interests due to their excellent physical, chemical and mechanical properties. The emergence of such exciting field come out more striking after isolation of graphene[1], a single layer in-plane arrangement of carbon atoms with honeycomb structure, obtained by exfoliating its bulk source known as graphite using a scotch tape. Such a 2D semimetal material has shown field-effect mobility up to 100,000 cm^2/Vs, implying a new fascinating element to be utilized not only in metallic transistor application but also photonics and optoelectronics[2], energy production and storage[3] and biosensing[4] applications. However, it should be noted that graphene has portfolio applications along with lack of a bandgap, hindering its potential in semiconductor applications. Inspired by the success of graphene, alternative layered and non-layered 2D materials have become the focus of intense researches and tremendous efforts have been put on developing new exotic 2D materials to fulfill the required demands. Beyond graphene, 2D materials specifically transition metal dichalcogenides (TMDCs) cover insulators, metals, and semiconductors, such as hexagonal boron nitride (h-BN)[5], Niobium Disulfide (NbS_2)[6] , and molybdenum disulfide (MoS_2)[7], respectively.

There are several varieties in classification of 2D materials, one of which shown in figure 1.1, conveying a 2D library in terms of their stability. Before going

through the production of any atomically thin material, it should be noted that due to the poor stability of 2D films compared to their 3D counterparts, the library of practical 2D crystals is rather limited[8].

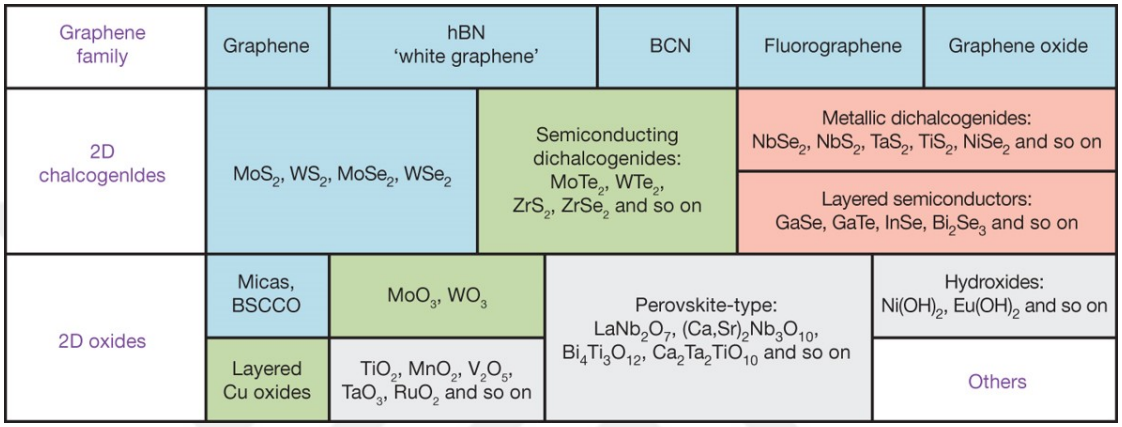

Figure 1.1: A sketch of 2D materials library. Shaded blue: Monolayers proved to be stable under ambient conditions (room temperature in air). Shaded green: probably stable in air. Shaded pink: unstable in air but that may be stable in inert atmosphere. Shaded grey: 3D compounds that have been successfully exfoliated down to monolayers. 'Others' indicates 2D crystals covering borides, carbides, nitrides and so on[8]. Copyright springer Nature 2013.

The 2D library is growing every year, followed by the layered materials that can be easily split into a subnanometer-thick crystals. However, this approach is strongly limited by the availability of 3D bulk source, hindering the proliferation of new 2D materials with unknown bulk root. Moreover, top-down methods (see figure 1.2) suffer from lack of scalability. For instance, mechanical exfoliation is almost the fastest and easiest method to obtain 2D crystals; however, the poorest one in terms of controlled thickness and size. To unravel the thickness controlling issue, liquid exfoliation methods have come into play and succeeded to form individual layers of various materials[9]. Nevertheless, in order to boost the efficiency, lithium-assisted liquid exfoliation is pertained but may results in excess intercalation of Li ions between the layers of a 2D product, changing its chemistry to an uncalled phase[10]. Therefore, the quality of solution-prepared 2D materials are of concern for most of applications.

With all these taken into account, artificial growth of novel 2D materials is in huge demand. There are several methods (see figure 1.2) for this purpose, each

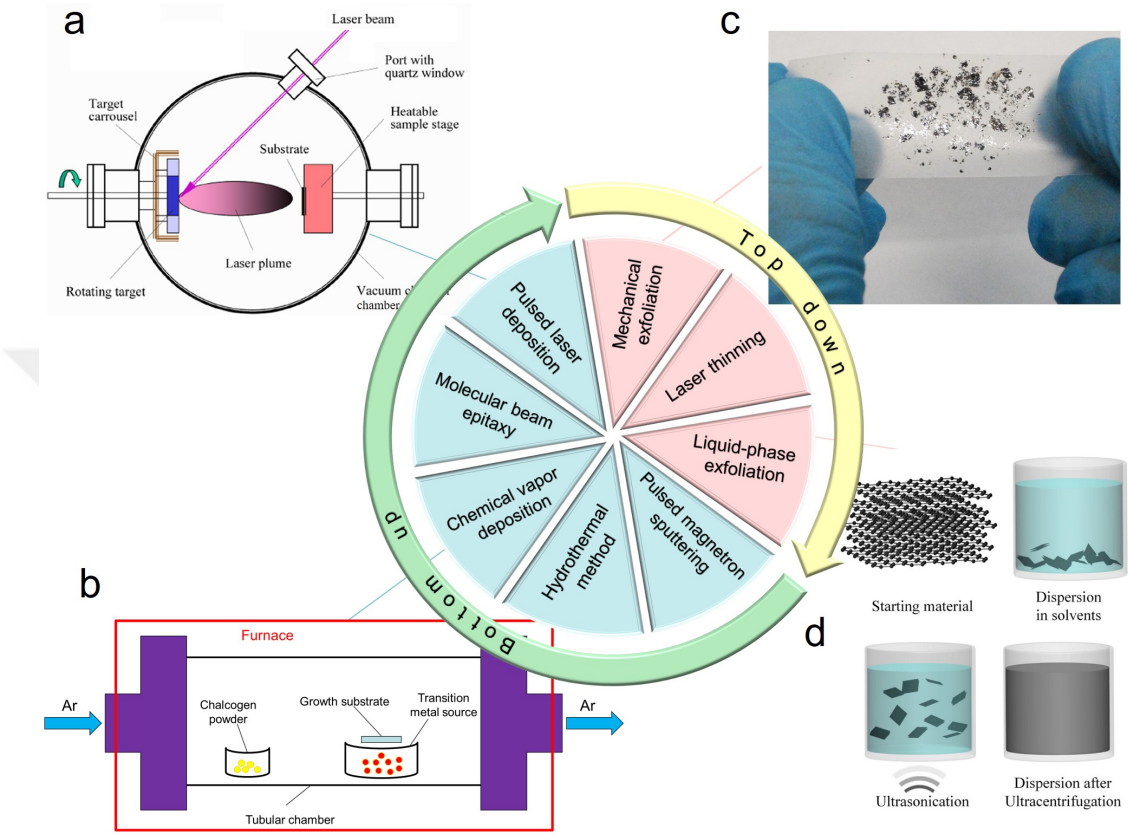

Figure 1.2: Fabrication methods of 2D materials from top-down to bottom-up methods. Schematics of (a) PLD and (b) CVD processes. (c) Mechanical exfoliation using a scotch-tape and (d) Schematics of various steps in liquid exfoliation process. Figure (a) is adopted from www.groups.ist.utl.pt. Figure (d) is reprinted with permission from [11] © The Optical Society.

of which has its own pros and cons. Among the bottom-up methods, Chemical Vapor Deposition (CVD) is a powerful method, and has been extensively used to grow not only 2D materials but their heterostructures in recent years, despite several challenges remaining. CVD and its modified versions like Metal-organic CVD (MOCVD) have been playing a key role to realize wafer-scale growth of continuous and homogeneous 2D films which are important for practical applications. Besides scalability, the properties of 2D products can be regulated in a CVD process. For example, number of layers, orientation (via lattice matching), morphology (shape and type of edge), phase (*in-situ* control or post treatment), quality and defect (via controlling the evaporation time) and doping can be tuned

and controlled via adjusting the growth parameters involved in a CVD process.

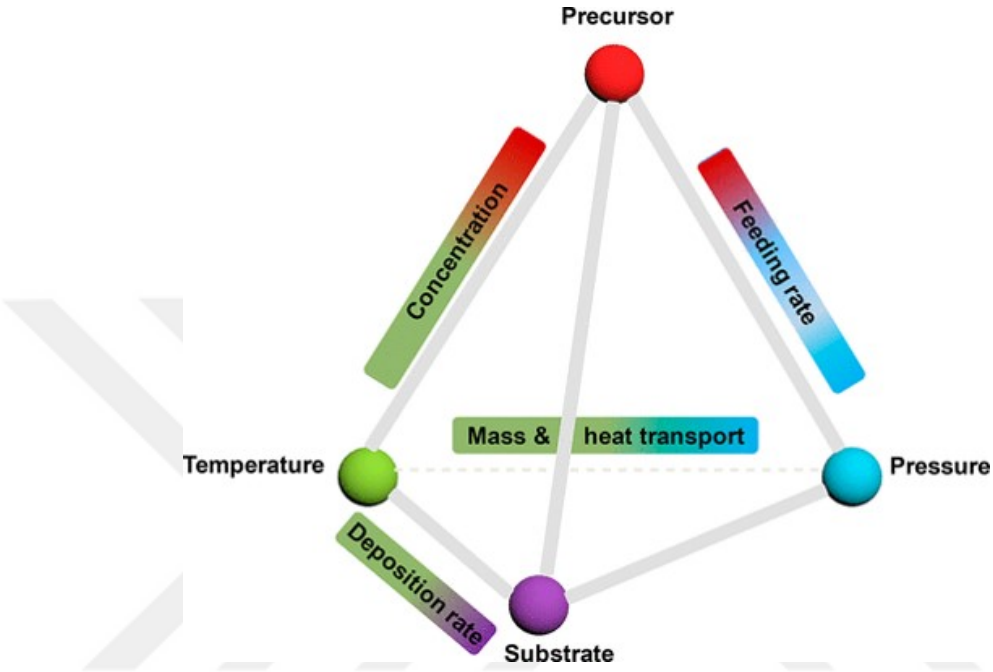

Figure 1.3: Schematic demonstration of various parameters involved in a CVD process, modifying the thermodynamics and kinetics of growth of 2D materials. Reprinted with permission from Ref[12]. Copyright (2018) American Chemical Society.

The size, morphology, phase and interfaces are the key features governing the properties of 2D materials. Controlling these factors can be achieved through logical design and careful adjustment of CVD growth processes. Consequently, understanding of how the growth parameters such as precursor, substrate, pressure and temperature act on mass and heat transport, interface reactions and thus the general mechanisms of the growth is highly crucial. The complexity arises from the fact that each of them is interconnected with the others as shown in figure 1.3. Upon a typical CVD process, no *in-situ* access is available during the growth. Any recipe optimization should be acquired via post-growth observation and characterization. This makes the optimization quite difficult and time-consuming since in order to direct the growth parameters towards the optimal condition, each of them should be changed individually and systematically resulting in a large number of trails mostly unfortunate. Besides the growth parameter complications, reproducibility is another major obstacle associates with

CVD processes. There are many optimized CVD recipes introduced in the literature, one would like to repeat them but mostly fail to work due to diversification of various factors such as chamber size and configuration, precursors amount and purity and precise growth temperature or rate, to name but a few. Therefore, there is no guaranty that all the optimized growth recipes will work everywhere.

1.1 Thesis motivation and outline

Finding a robust solution for the mentioned bothering problems is the primary concern of this thesis. Shedding light on the CVD growth process of 2D materials and revealing more information and details out of such a black-box is the main motivation of our work. As will be discussed in the following chapters, we have designed and fabricated a custom-made CVD chamber to optically access the growth and observe in real-time how 2D crystals formed at high temperatures in accordance with the effect of each growth parameter. Developing such a chamber has opened up a new world to not only reliably synthesize 2D crystals but also investigate the involved growth mechanisms upon the CVD process.

Chapter 2 gives more information about the design and fabrication of our CVD custom-made chamber. The challenge of integrating a CVD process with an optical microscope will be addressed along with the optical access design, heating and cooling systems.

Chapter 3 delivers how practically the chamber can come into play. For the first time, TMDCs growth has been observed at high temperatures, leading us to unravel the involved mechanisms in salt-assisted CVD grown TMDCs. We not only disclose their formations at growth temperatures but also study the reaction routes that are critical to the production of the desired layered thin crystals. Formation of monolayer WSe_2 and $MoSe_2$ along with their lateral/vertical heterostructures have been accomplished to show the versatile employment of the chamber.

Chapter 4 states the power of the chamber to develop recipes for novel 2D materials that have not been synthesized so far. We show synthesis of high-quality single-crystal V_2O_3 nanoplates with 2D characteristic allowing us to study their peculiar electrical and physical properties such as metal-insulator transition (MIT) and supercritical state.

Chapter 5 embraces novel synthesis of ultra-thin layered K-MnO_2 crystals, spontaneously intercalated with potassium ions upon the growth. The in-plane ionic conductivity will be discussed which has been realized for the first time in 2D community. Furthermore, dynamic phase transitions upon electrical and optical modulation of the ions is revealed accompiend with the effect of ambient moisture. The mechanisms behind K-MnO_2 memristive behavior is extensively investigated and finally emulation of neuromorphic synaptic functions is comprehended via 2D K-MnO_2 memristors.

Chapter 6 concludes the most important findings in the thesis and conveys the future insights about the potential research studies carried out via the real-time observation (RTO)-CVD chamber.

Chapter 2

Design and fabrication of the custom-made CVD chamber for *in-situ* optical access

The necessary design concerns to build a robust CVD chamber equipped with an optical access will be discussed in the following chapter. The main objective is how to emulate typical tubular CVD chamber functions along with ruling out its fundamental limitations such as lack of independent temperature zones. The design is further considering integration of an optical access to the growth, while the chamber is operating at high temperatures (> 800 °C).

2.1 Chamber design

Figure 2.1 shows he assembly of three main parts of the chamber: 1) The cooling base that holds the main cooling channels for the reactor, designed in a spiral pattern to increase the cooling efficiency. 2) the Reactor box as a housing for hermetically sealed electrical feedthroughs and the gas in/outlets. 3) The lid which is composed of lid body, sapphire window and its holder, assembled in a

vacuum tight way. There are 3-millimeter-diameter channels drilled inside the lid dedicated as another cooling path to keep the lid cool. All the bodies are machined out of 6061 Aluminium alloy as it offers 10 times higher thermal conductivity compared to 304 stainless steel.

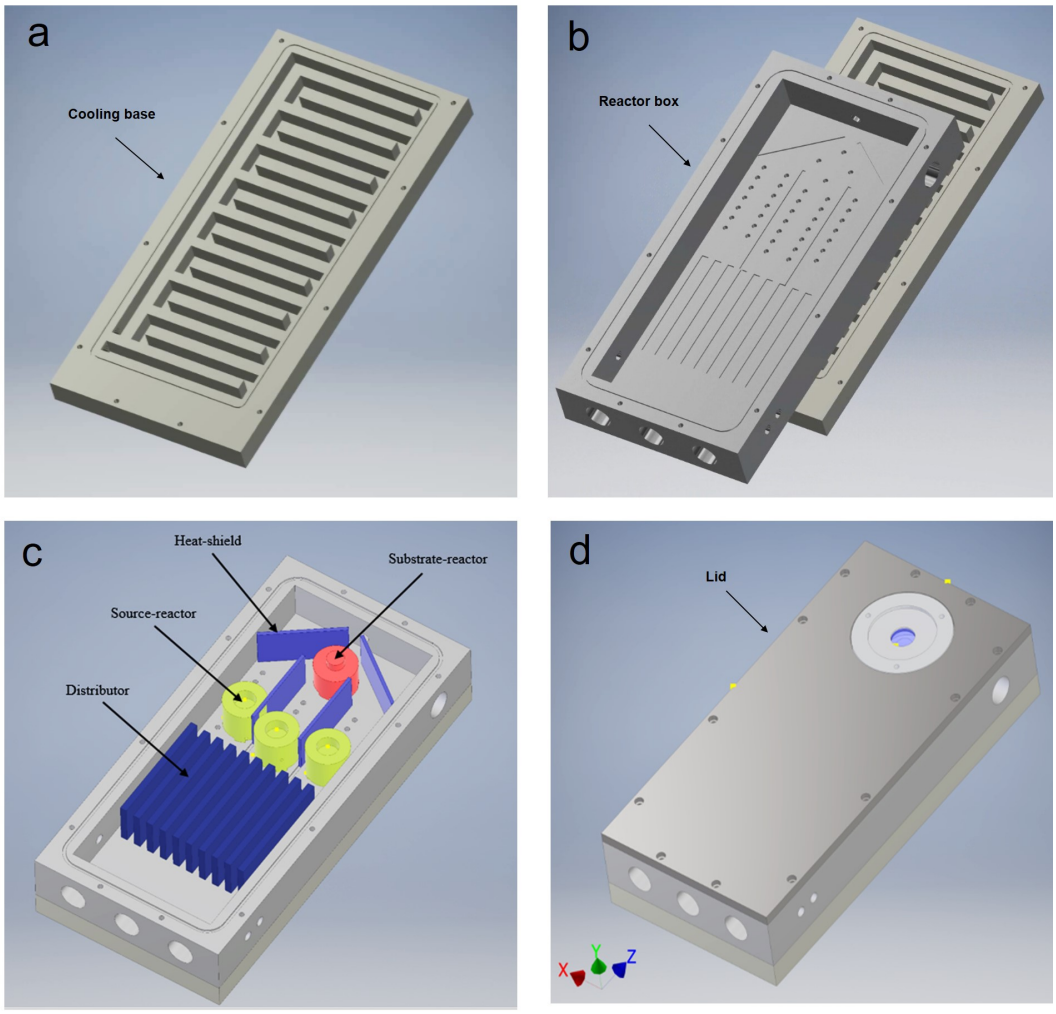

Figure 2.1: Schematic demonstration of the assembly of the main parts of the chambers and the interior components. (a) Cooling base, (b) Reactor box, (c) Interior components and (d) Lid body including the optical sapphire window and holder.

The interior components inside the reactor box are: 1) The substrate reactor (shown in figure 2.1 (c) in red), in charge of heating the growth substrate, over which the sapphire window is designated to allow optical access to the growth substrate. 2) The source reactors (shown in figure 2.1 (c) in yellow) assigned for

heating the precursors. Three reactors can be placed inside the chamber granting individual heating of each precursors without interference (Both substrate and source heaters made of Alumina whose fabrication is described in section 2.2). 3) The heat-shield walls with 6 mm thickness made of Aluminium, are occasionally laid down between the heaters, when two or three of them are active during the CVD process in order to avoid chemical vapor mixture before reaching to the substrate reactor. 4) The distributors are placed in the way of gases before reaching the source reactors to further ensure the laminar flow of the input gases.

Figure 2.2 shows the schematic and final assembly of the machined chamber with the configuration of the heaters, relevant lengths and the quarter cross-section of the upper lid. The water jackets at the top lid and the bottom base are identified in the cross-sectional view image (c). Three copper pipes (6 mm diameter) have been inserted and vacuum-sealed into the chamber as the inlets of different gases, connected each to a mass flow controller. The outlet is the same-type pipe at the opposite side, regarded as the chamber exhaust. Before machining the final chamber, 3D prototype was printed to examine the component assemblies. In addition, using a transparent lid, while blowing smoking fumes from the inlets we observe how the gases are flowing inside to make sure about the flow access over the heaters.

2.2 Auxiliary components

To govern the mass flow controllers and the heater temperatures, the chamber is orchestrated via a LabView program. The temperature profile (temperature vs. time) of each growth process is also monitored to record the history of all CVD growth trials. The optical port on the lid is a 0.5 mm thick sapphire disk and it is directly located above the substrate heater. We use a 700 W/h chiller to control the coolant temperature ($\simeq$ 10 °C) and circulate it through the water jackets. A closed-cycle chiller supplies water to the cooling channels embedded within the chamber body and the lid. The whole chamber is placed on an Olympus BX 51WI fixed stage microscope, therefore, rather than changing the height of

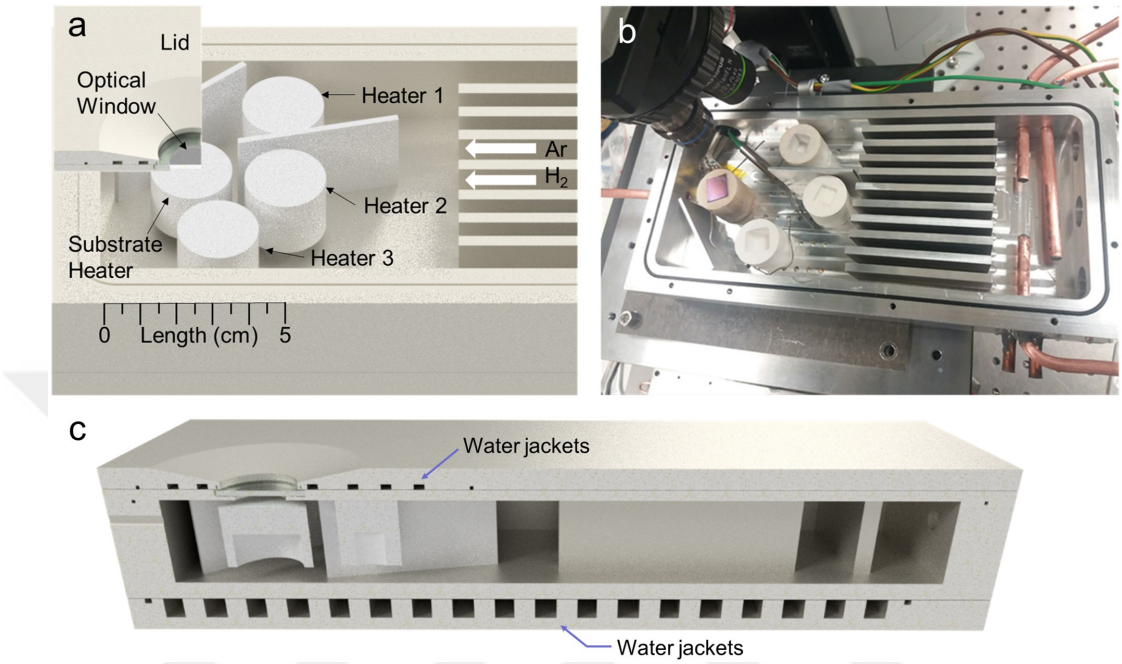

Figure 2.2: Final state of the custom-made CVD chamber. (a) Schematic of the chamber including the configuration of the heaters, relevant lengths and the quarter cross-section of the upper lid. Ar and H_2 flow is indicated by the white arrows. (b) Final assembly of the machined chamber. (c) Schematic of the cross-sectional view of the chamber with indicated water jackets.

the stage to adjust the objective focus, the nosepiece is being moved. For the X-Y motion, the whole chamber moves thanks to the flexible piping and cabling. Electrical connections for temperature control are made via hermetically sealed feedthroughs. There are two separate gas inlets, one for Ar and the other for H_2 and a single exhaust at the opposite end of the chamber. Gases are dosed through mass flow controllers. The microscope is equipped with 5x, 20x and an ultra-long working distance 40x objective with 20x multiplication at the eyepiece. A Canon DSLR camera is connected to the microscope for capturing HD video and high-resolution pictures.

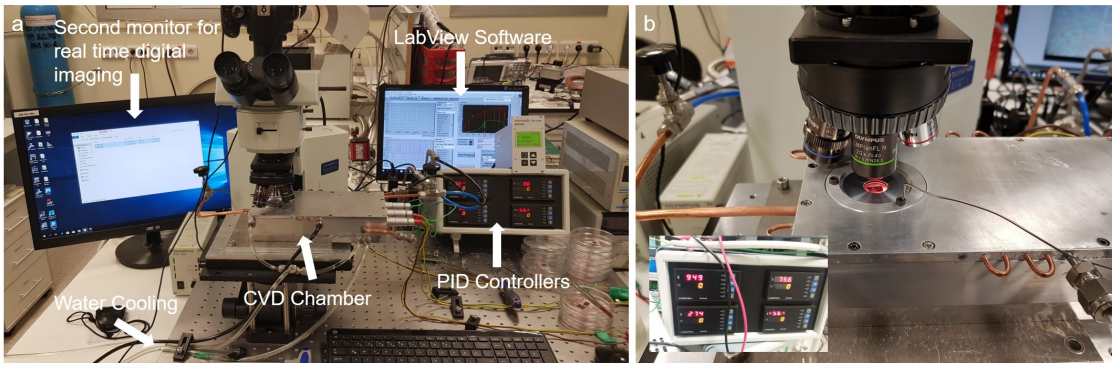

Figure 2.3: The final state of the assemblies. (a) Picture shows the layout of the overall setup. Some essential components are labeled on the picture. (b) Close-up view of the chamber running at high temperature. Inset picture shows the PID controller assembly that indicates the temperatures of the substrate heater (top left), heater 1 (top right) and heater 2 (bottom left) during a typical CVD growth.

2.3 Alumina Heaters

After satisfying all the assemblies and necessary design corrections, the main remaining challenge is heating up the chamber and fulfilling the required temperature targets (up to 1000 °C) with a control over the rate of heating/cooling. Considering the size of crucible heaters, we designed and 3D printed cylindrical molds used to slip cast the alumina slurry composed of a mixture of 85% Al_2O_3, 5% Kaolin and 10% water. Kanthal A1 22 Ga wire coils placed within the mold as the heat element for their good oxidation resistance property. After slip casting, we dry the green bodies at 100 °C to evaporate the excess water and mixture to set. Due to the enhanced plasticity of the slip and thus work-ability of the green bodies, we are able to carve them to the desired shape and size. Finally, the bodies are sintered at 1400 °C for three hours. This forms a solid body, yet as the sintering temperature is kept relatively lower to prevent deterioration of Kanthal wires, therefore the alumina crucibles are not as dense and strong as produced by other methods. After the heaters are sintered, we place thermocouple 1 mm deep into the surface and by using a hand-held infrared thermometer, we check the accuracy of the reading by the thermocouple. If the reading is accurate within ± 10 °C, we place the heater in the chamber. For the substrate heaters we perform

one final calibration using NaCl. A few grains of NaCl is placed on an oxidized chip and its melting point is observed on the substrate heater. If it agrees ± 20 °C with the melting point of NaCl (≃ 800 °C), we start using the heater. Typically, the heaters last for many growth cycles. Indeed, most of the studies we reported in this thesis has been performed using the same set of heaters. Serious cautions must be taken especially during cool-down. Sudden changes in the heater current result in rapid expansion and contraction of the Kanthal wire, which weakens or kills the heater over time due to the thermal shock.

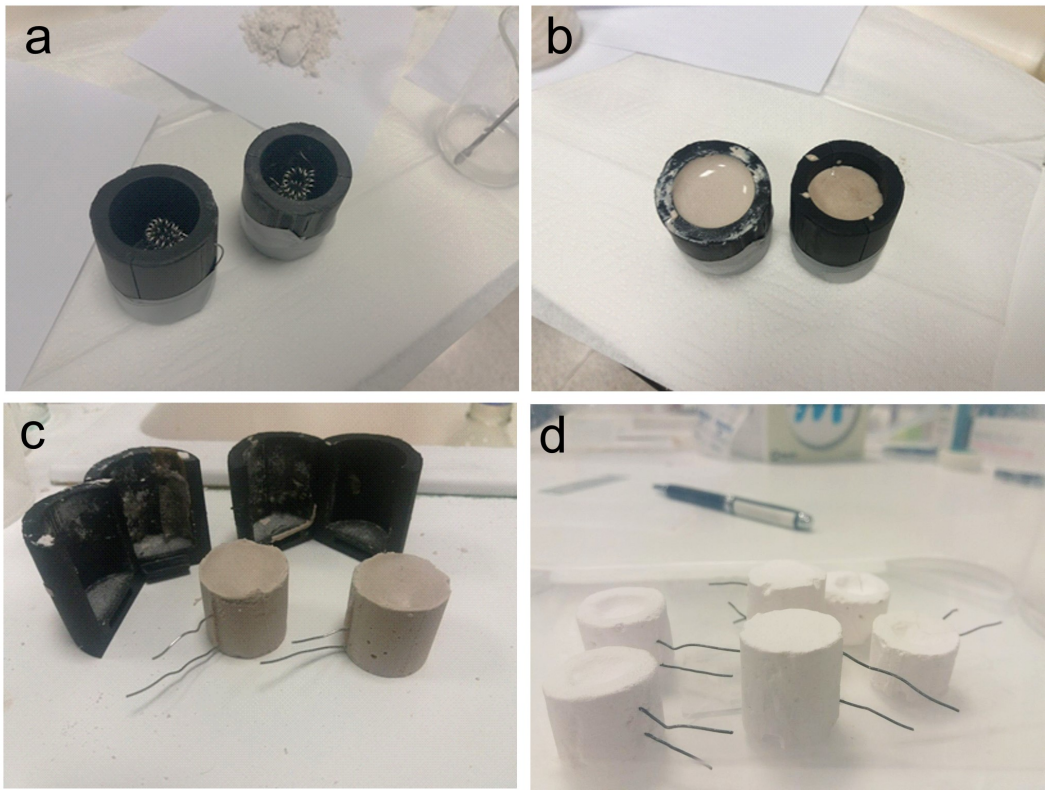

Figure 2.4: Fabrication process steps of alumina crucibles. (a) 3D printed molds with winded Kanthal coils inside, (b) The casted slurry into the molds, (c) Green bodies after drying at 100 °C for few hours and (d) alumina crucibles after sintering at 1400 °C for three hours.

2.4 Thermal simulations

Considering the cold wall CVD chamber at growth temperatures, we modeled the heater configuration in an Ar atmosphere using a finite element analysis software (COMSOL). Although it is simulated under no gas flow, since the flow rate is low under operation, it makes no difference on the temperature profile. For the analysis, we kept the top lid at 50 °C and the heater at 800 °C. Thermal analysis results reveal that while the surface of the heater is at 800 °C, the temperature within the first millimeter over the crucibles is above 600 °C. Such a thermal gradient towards the lid creates a convection current conveying some of the vaporized precursors up to the lid and the observation window. For many materials we synthesized, this causes no vision problem; however, for some that has high vapor pressure, condensation of the evaporated matter over the observation window hinders the vision partially.

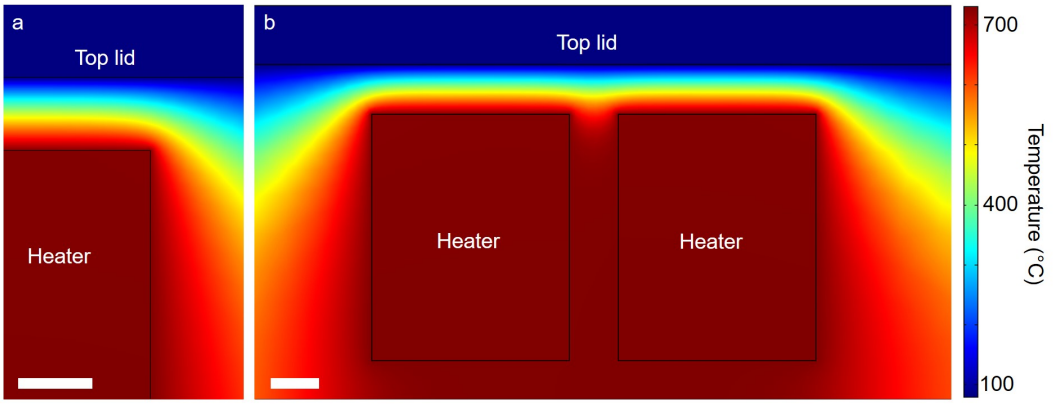

Figure 2.5: Cross-sectional view of the thermal distribution within the CVD chamber. (a) Single heater configuration and (b) double heater configuration. Scale bar represents 3 mm.

Chapter 3

Real Time Optical Observation and Control of Atomically Thin Transition Metal Dichalcogenide Synthesis

The real-time observation of the growth of 2D materials opens a new science world of inspection and analysis. Controlling numerous growth parameters to obtain atomically thin TMDCs via a black-box tubular CVD chamber is quite challenging. As each parameter play a role in the growth mechanism and therefore the final product, understanding the mechanism with the correlated parameters can be only studied with the post-growth observations. All the proposed mechanisms and their relation to the growth conditions are inferred from characterizing intermediate formations obtained by stopping the growth blindly. In this chapter, for the first time, we show how a custom-made CVD chamber allowing real-time optical monitoring during the TMDCs growth can be employed to not only disclose their formation at growth temperatures but also study the reaction routes that are critical to the production of the desired layered thin crystals. Formation of WSe_2 and $MoSe_2$ along with their lateral/vertical heterostructures has been investigated as the case studies of salt assisted TMDC synthesis.

3.1 Introduction

Two-dimensional (2D) transition metal dichalcogenide (TMDC) materials have drawn massive attention in optoelectronic devices, flexible sensors, catalysis, energy conversion and biomedical applications due to their exceptional physical and chemical properties[13][14][15]. Established as the active materials for multiple devices, the recent primary focus is the cost-effective, reliable and large-scale synthesis of 2D TMDCs using processes compatible with current semiconductor technology for their extensive development and application. Among the bottom-up synthesis methods introduced in the previous chapter, Chemical Vapor Deposition (CVD) is a promising one to synthesize high-quality 2D materials in efficient manner, suitable for industrial large-scale preparation[16][17]. In this regard, *in-situ* information from the CVD process can grant exploring the growth mechanism and controlling the quality of 2D materials. CVD synthesis of 2D materials typically requires high temperature conditions with a wide range of temperature variations, special gas environment and vaporized precursors at growth temperatures, all restrict the *in-situ* measurements and lead to difficulty for most of the characterization methods.

Having said the requisite of real-time information for understanding the complex growth mechanisms and developing optimized recipe, only few studies have focused on the *in-situ* investigation of 2D materials growth so far. Linfeng Fei et al[18] studied how orientation and grain size of MoS_2 flakes are evolving at various temperatures using *in-situ* Transmission Electron Microscopy (TEM). However, this research reported the non-real-time characterization of MoS_2 prepared by the thermolysis of ammonium thiomolybdates which is not a commonly used precursor for CVD grown 2D materials. Lopez-Posadas et al[19] monitored the CVD growth of MoS_2 monolayers on sapphire substrates using Differential Transmittance Spectroscopy (DTS). Nevertheless, DTS is only applicable to transparent substrates. Also, the growth information of MoS_2 at late growth stage was shielded due to the deposition of molybdenum trioxide on the observation window. Direct observation of graphene growth has been accomplished

using aberration-corrected Scanning TEM (STEM) and Scanning Electron Microscopy (SEM)[20][21]. Compared to TMDCs, CVD synthesis of graphene requires less-complex growth elements like single methane gas source for carbon, which enables compatibility with electron spectroscopy techniques. This is not valid for the growth of TMDCs due to more elaborate CVD condition.

In a typical TMDC CVD synthesis, a transition metal and chalcogen containing precursors are placed in a tube furnace followed by a target grwoth substrate at different positions or configurations (up-stream and face-down). At some high temperatures, Ar/H_2 mixture carries the vaporized chalcogen precursor and the metal compounds to form atomically thin layers on the target substrate. Salts are also added to the conventionally used metal oxide precursors to form more volatile intermediate compounds[22][23][24]. Most TMCDs are difficult to produce because of the high melting points of their metal and metal oxide precursors. Molten-salt-assisted methods have been used to produce ceramic powders at relatively low temperature[25], and interestingly equipped with this idea, salt-assisted CVD method have been broadly applied to synthesize a wide variety of 2D TMDCs[26]. Although 47 different compounds have been synthesized in this comprehensive research study (For more details see figure 3.1), the role of salt is poorly investigated and only ascribed by lowering the melting point of the reactants.

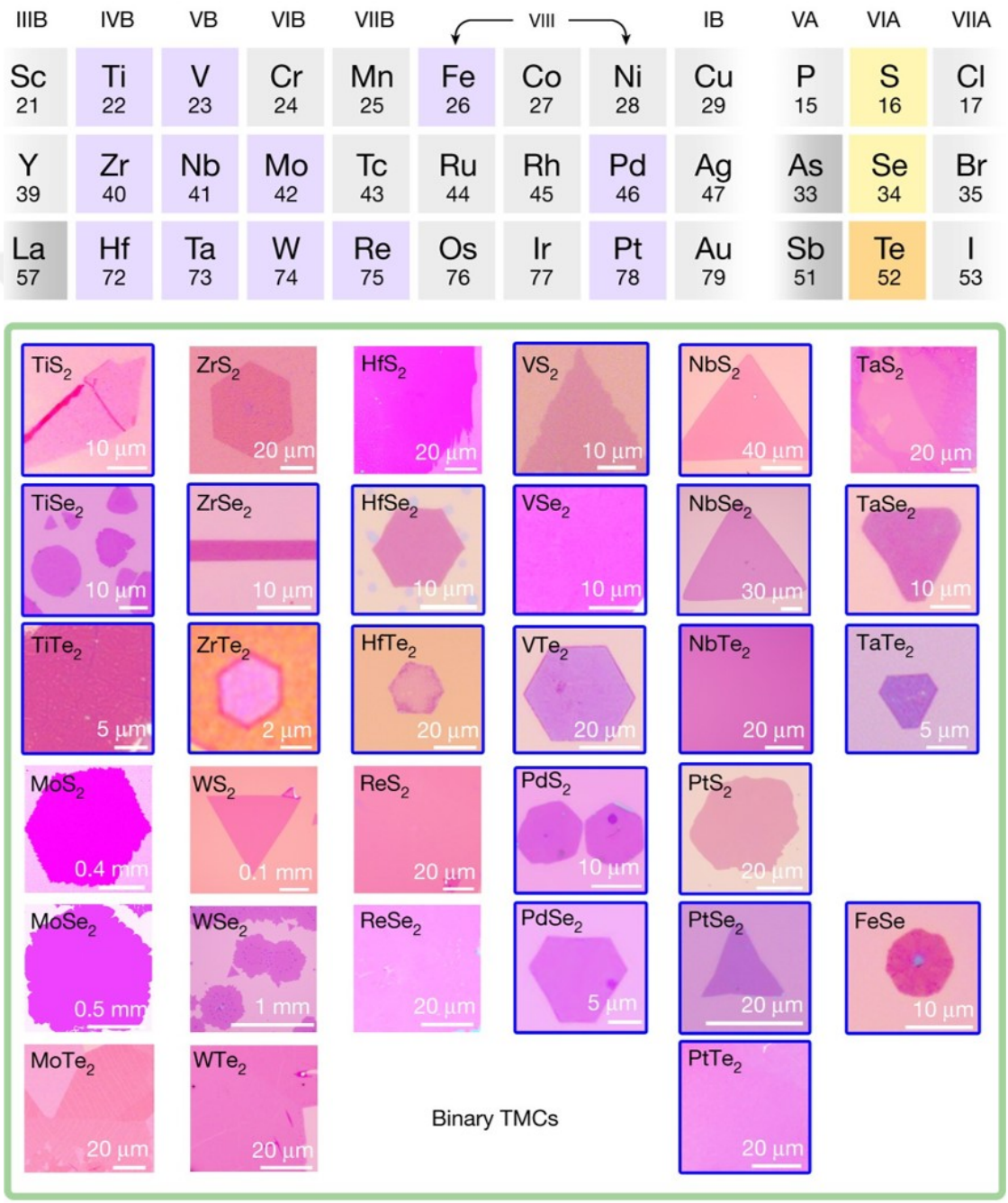

Figure 3.1: Optical images of the library of salt-assisted CVD synthesized TMDCs using various metals (highlighted in purple) and chalcogens (highlighted in yellow)[26]. Copyright springer Nature 2018.

3.2 Experimental method

We focus on salt assisted synthesis of WSe_2 monolayers on an oxidized Si chip as a demonstration of the versatility of our chamber. Fine mesh grains of WO_3 and NaCl are placed on heater 2 and Se on heater 1 shown in figure 3.2 (b). The substrate heater and heater 2 temperatures are increased simultaneously. When they reach 600 ℃, the temperature of heater 1 is brought to 300 ℃, above the melting point of Se. At the same time H_2 is introduced to aid the growth of the monolayers at different growth states to examine its role in the dynamic CVD process. We use Atomic Force Microscopy (AFM), Raman and Photo-luminescence (PL) intensity maps to characterize the as grown crystals. X-ray Photoelectron Spectroscopy (XPS) and Energy-dispersive X-ray Spectroscopy (EDS) are performed to analyze the intermediate compounds formed at various growth states.

The custom-made CVD chamber described in chapter 2 is used to monitor the growth optically. The chamber body temperature is maintained at or near room temperature. Outside the chamber, the temperature of the hottest regions remains below 50 °C. The chamber can reach down to 10^3 mBar using an oil rotary vane pump. Before heating the heaters, the chamber is flushed with Argon and re-vacuumed couple of times to obtain the optimum inert environment. 100 sccm Argon maintains all over heating and cooling steps. 20 sccm H_2 is introduced after vaporizing sufficient Se to initiate the growth. Alongside optical observation of the desired monolayer size and morphology, the H_2 flow is cut-off and chamber is cooled down to the room temperature under Ar environment.

3.3 Result and discussion

3.3.1 Mechanisms involved in salt-assisted TMDC synthesis

In spite of many studies on the CVD grown TMDCs, it is unclear which growth mode prevails under different growth conditions, primarily due to the inaccessibility of the tube furnace to track the on-going reactions during the growth. Typically, the involved growth mechanisms are proposed via post-growth observation and characterization by capturing and analyzing the intermediate products leading to the desired crystal growth. These products must be captured by shutting off the furnace and quenching the synthesis by a rapid cool down, with a probability of missing some during the growth process. In addition, the effect of each individual growth parameters on the intermediate compounds can only be comprehended if distinguished from the others over the growth operation. With all these taken into account, two growth modes have been proposed in CVD synthesis of TMDCs. (1) Vapour–Solid–Solid (VSS): Vaporized precursors are adsorbed on the substrate and form crystals via surface diffusion and bond formation at an elevated temperature[27] and (2) Vapour–Liquid–Solid (VLS): Supersaturated liquid droplets containing the constituent elements form the crystals[28]. Figure 3.2 (a) depicts these growth modes schematically.

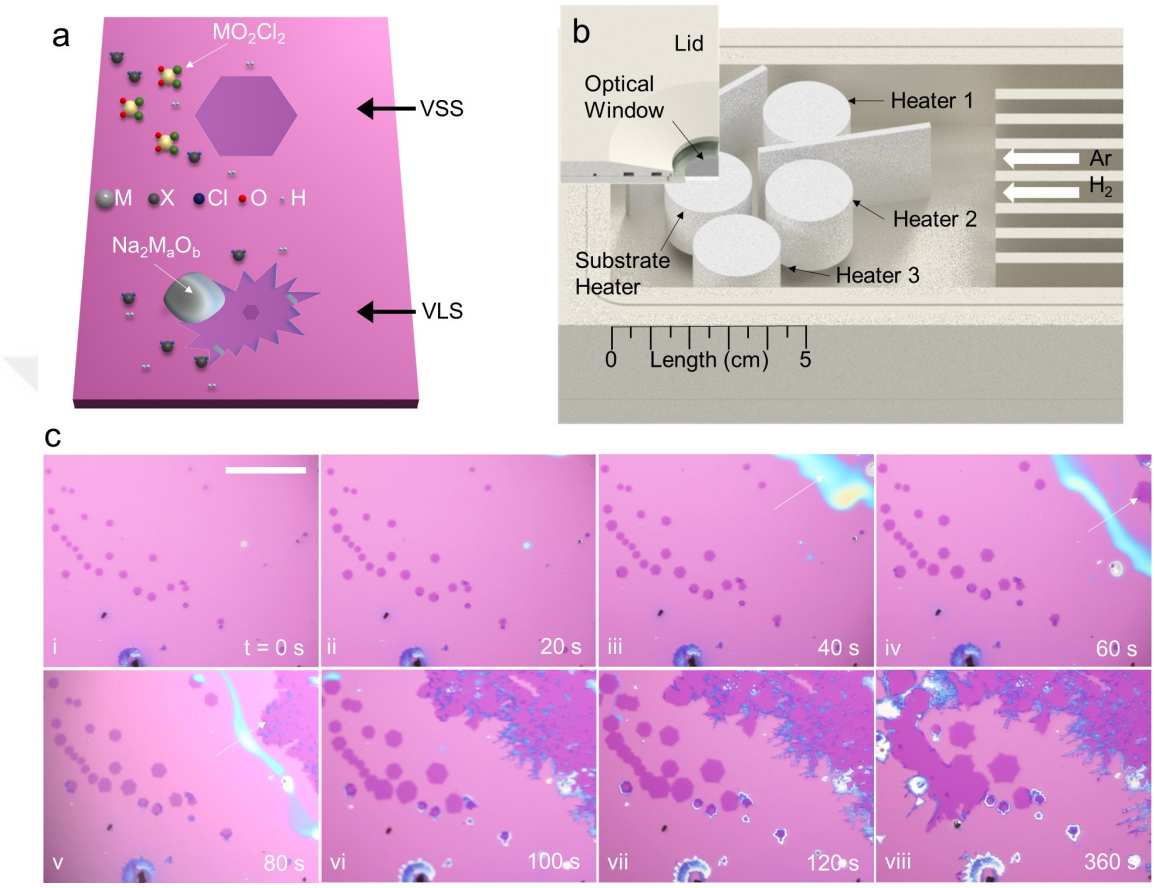

Figure 3.2: Schematic of the CVD growth modes, custom-made CVD chamber, and an exemplary growth[29]. (a) Depictions of VSS and VLS growth modes for NaCl assisted TMDC synthesis. In the VSS mode, adsorbed vapour forms the crystals while in the VLS mode, a liquid precursor forms the crystal via a chemical reaction. M and X denote the metal and the chalcogen precursors, respectively. (b) Schematic of the custom-made CVD chamber depicts the configuration of the heaters, relevant lengths and the quarter cross-section of the upper lid. Ar and H_2 flows are indicated by the white arrows. Heater 1 is separated from the rest of the reactors to prevent heating of the chalcogen precursor by radiation from the precursor heaters. (c) Real time optical micrographs captured during a synthesis is given in (i–viii). The substrate temperature is at 790 °C and the series of pictures show the evolution of atomically thin WSe_2 crystals. Time t = 0 s marks the beginning of our observation of the particular region captured in the images. Hexagonal monolayers grow larger as time goes on with a rate of ≈ 0.2 μm s^{-1}. White arrow in (iii) attracts attention to the liquid that promotes the synthesis of the monolayers. As time goes on the amount of liquid diminishes and irregularly shaped WSe_2 crystals form. After 6 minutes (viii) from the beginning of the observation, no liquid is left, and the lateral growth of the crystals stops. Scale bar is 100 μm.

To begin with, we focus on salt assisted synthesis of WSe_2 monolayers on a 280 nm oxidized silicon chip. Fine mesh grains of WO_3 and NaCl are placed on heater 2 and Se on heater 1, shown in figure 3.2 (b). While the substrate heater and heater 2 simultaneously heated up to 600 °C, the temperature of heater 1 is brought to 300 °C, above the melting point of Se. At this point, H_2 is introduced to aid the growth of the monolayers. Figure 3.2 (c) shows a series of optical images obtained during the synthesis at 790 °C (see supplementary movie 1 for the entire video). We successfully observed formation of WSe_2 monolayers in real time, which can be attributed to two distinguished growth modes: (1) VSS mode promotes when vaporized volatile precursors are uniformly supplied to the nuclei in the 2D growth plane, yielding structures with a characteristic crystal shape that can be determined by the inherent free energy of the crystal edges and surface diffusion kinetics[30]. (2) VLS mode in which the growth products are often randomly oriented multilayered crystal growing much faster than VSS ones and typically consisting of dendritic edges and morphology. VLS-like growth of laterally oriented graphene[31] and MoS_2[28] nanoribbons from molten nickel and Na-Mo-O droplets respectively, suggest that non-tubular atomically thin structures can be synthesized in the VLS mode, which is experimentally demonstrated in real time for the first time here.

As shown in figure 3.2 (c), VLS grown crystals are growing fast by consuming a bluish liquid. The growth ends after the termination of the liquid phase. Accordingly, characterization of the intermediate liquid products is vital for understanding the possible crystal formation routes. One of the powerful features of our chamber is the ability to follow the on-going reactions without missing any, and stop the growth at anytime to capture the intermediate formations. Thus, as to study the liquid phase which is the side-product of reaction between WO_3 and NaCl, we placed a 250 μm^3 large grain of NaCl surrounded by smaller grains of WO_3 on a SiO_2/Si chip on the substrate heater and observed the dynamics of the intermediate compound formations before WSe_2 growth. Figure 3.3 (a-f) shows ptical images captured during at various high temperatures, indicating the intermediate stages of the reaction between WO_3 and NaCl.

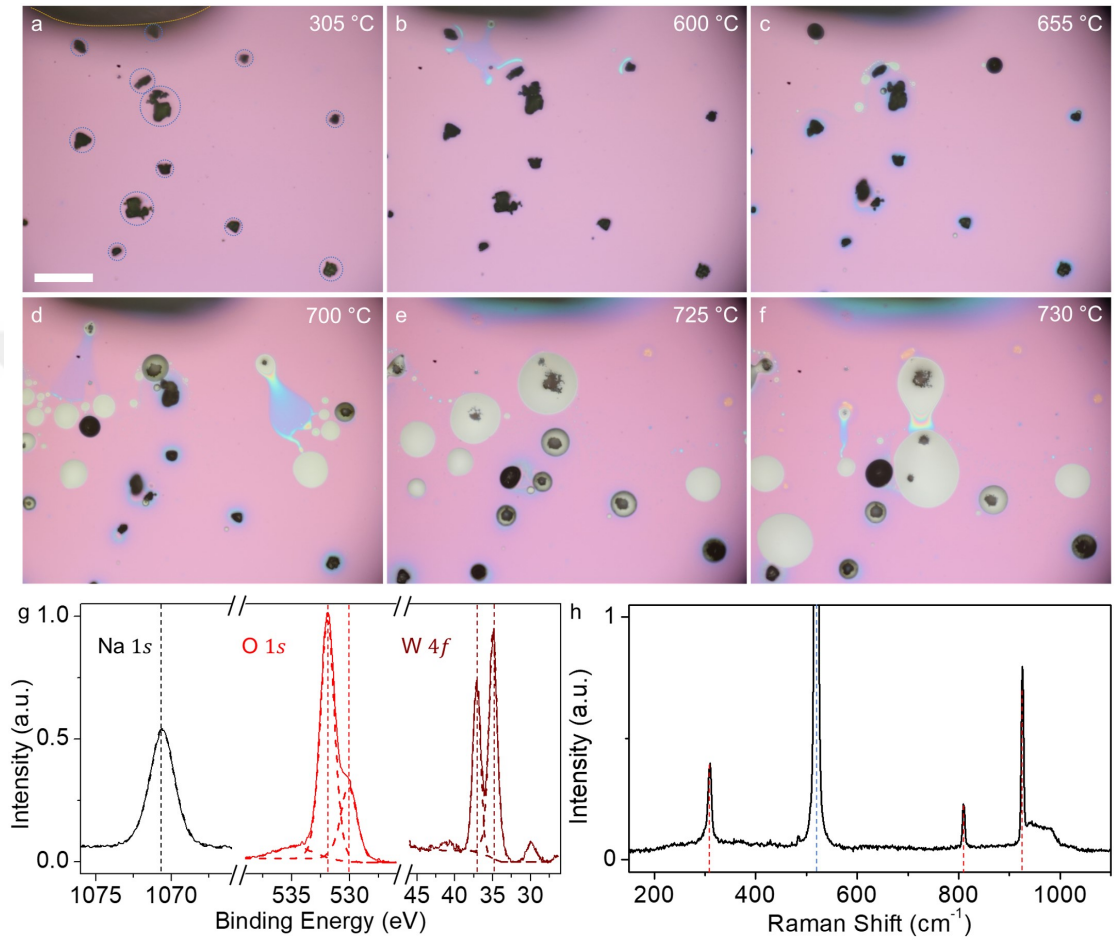

Figure 3.3: Formation and characterization of the intermediate compound[29]. (a–f) Optical micrographs obtained during the synthesis at various temperatures. Yellow dashed line at the top in (a) indicates the edge of the salt particle and grains encircled by blue dashed lines are WO_3 particles. As the temperature increases, first a turquoise liquid forms around the WO_3 grains. Then, as time goes on, the liquid droplet enlarges by consuming the WO_3 grains. Scale bar is 100 μm. (g) XPS survey shows that the liquid is composed of Na, O and W. The Na 1s survey can be fitted with a single peak at 1070.6 eV that can be attributed to Na in Na_2WO_4. O 1s binding energy can be fitted with two peaks, one at 532.9 eV and the other at 530.2 eV that can be attributed to the substrate and Na_2WO_4, respectively. W $4f_{5/2}$ and $4f_{7/2}$ peaks located at 37.3 and 34.9 eV corresponds to the previously reported values[32][33] for W 4f of Na_2WO_4 in the literature. The peak at 30.1 eV can be attributed to Na 2p. (h) The Raman spectrum obtained from the solidified liquid intermediate compound. Peaks marked with red dashed lines correspond to the Raman modes of Na_2WO_4 and the blue dashed line marks the 520 cm^{-1} Si peak from the substrate.

The first liquid formation is observed in the vicinity of WO_3 particles around 600 °C, which is consistent with the previously reported thermogravimetry and differential scanning calorimetry measurements on NaCl–WO_3 mixtures[26]. When we stop the reactions at this stage and perform SEM imaging and EDS mapping on the solidified liquid formations, Na and Cl on the WO_3 grains are detected (see figure 3.4), indicating sublimation of NaCl and condensation on WO_3. At higher substrate temperatures, more liquid forms and its color changes from turquoise to beige. Such a liquid formation must be the eutectic product between NaCl and WO_3 as both of them melt above 800 °C. As temperature goes up, especially above 730 °C, no solid particles remain as a result of the reaction (see supplementary movie 2 for the entire video). This reaction has the key role in both VSS and VLS crystal syntheses as will be shown in the following.

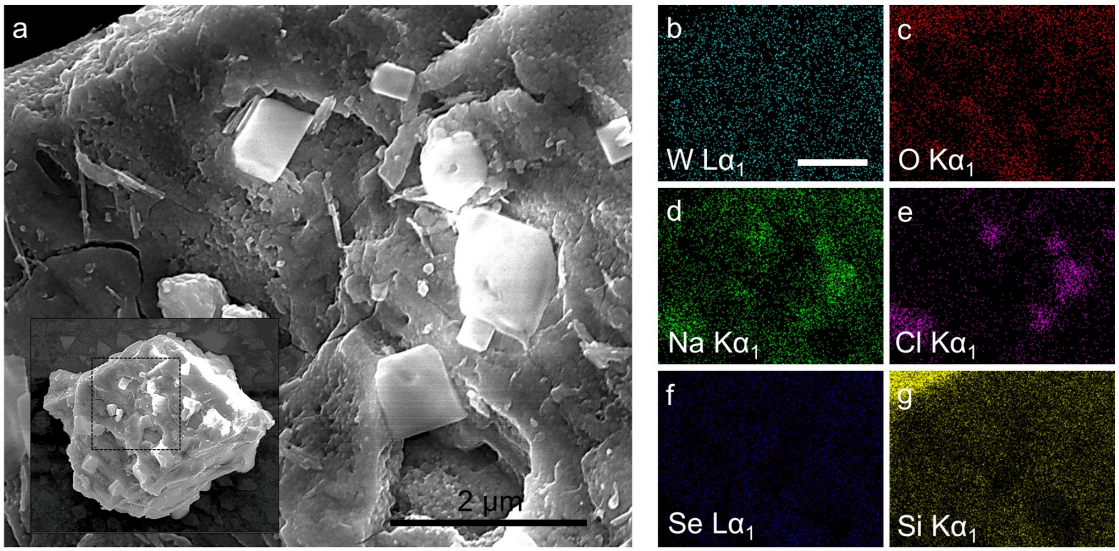

Figure 3.4: Early stage NaCl-WO_3 reaction[29]. (a) SEM image of a WO_3 grain shows crystal formations on the surface. (b-g) EDS maps taken from the same region shows that there are regions where NaCl particles recrystallized on the WO_3 surface. Comparing d and e reveals that not all the Na on the surface is in NaCl form. (f) Although no Se is introduced, as the Se Lα1 peak coincides with the tail of the W Lα1 peak, we observe an erroneous distribution of Se all over the material. The scale bar for (a) is 5 μm and for (b) is 2 μm.

To determine the chemical composition of the liquid phase, once it is fully formed (with no Se exposure), we cool down the chamber and immediately conduct XPS measurement. XPS survey reveals that the solidified liquid is composed of Na, O, W but not Cl. High resolution XPS spectra of Na 1s, O 1s and W 4f binding energies (see figure 3.3 (g)) match perfectly with the values reported for sodium tungstate, Na_2WO_4[32][33]. Raman spectrum taken from the solidified liquid phase further supports Na_2WO_4 formation[34][35]. Identified the first product of the reaction between NaCl and WO_3, the second product can be WO_2Cl_2, directing to the chemical reaction below:

$$WO_3 + 2NaCl \rightarrow WO_2Cl_2(g) + Na_2WO_4(l) \qquad (1)$$

While observing the liquid phase around 600 °C, WO_2Cl_2 is in gaseous phase, leaving the chamber by the carrier gas. This explains the absence of Cl in both XPS and EDX analyses of the later stage molten product. This is our prime clue to lead the growth to follow either the VLS or VSS mode by controlling the volatile gaseous intermediate part.

We investigate the effect of Se exposure upon the intermediate compounds to compile all the reaction routes resulting in WSe_2 crystals. When we introduce Se after forming the liquid formation at 750 °C, no WSe_2 crystal is being synthesized and the liquid remained unchanged with the passage of time. Despite introducing Se vapour at various substrate temperatures ranging from 700 to 900 °C, we do not observe WSe_2 formation. These experiments imply the essential role of H_2 in the salt-assisted CVD synthesis. With the unique ability of *in-situ* monitoring high temperature events, we can tune the growth parameters and see the effect online. To elucidate the role of H_2 in monolayer formation, we first examined the sole effect of H_2. Although there are numerous reports[36][37][38][39][40][37] on the effect of H_2 in atomically thin TMDC synthesis, its function in the salt assisted growth is not ubiquitous. H_2 is a common integrant in CVD growth of TMDCs, which is typically sent at the growth temperatures. Here, we explicate the effect of H_2 at different growth states. We play with the introduction timing of H_2 and realize the way it tunes the outcome. When we introduce H_2 into the

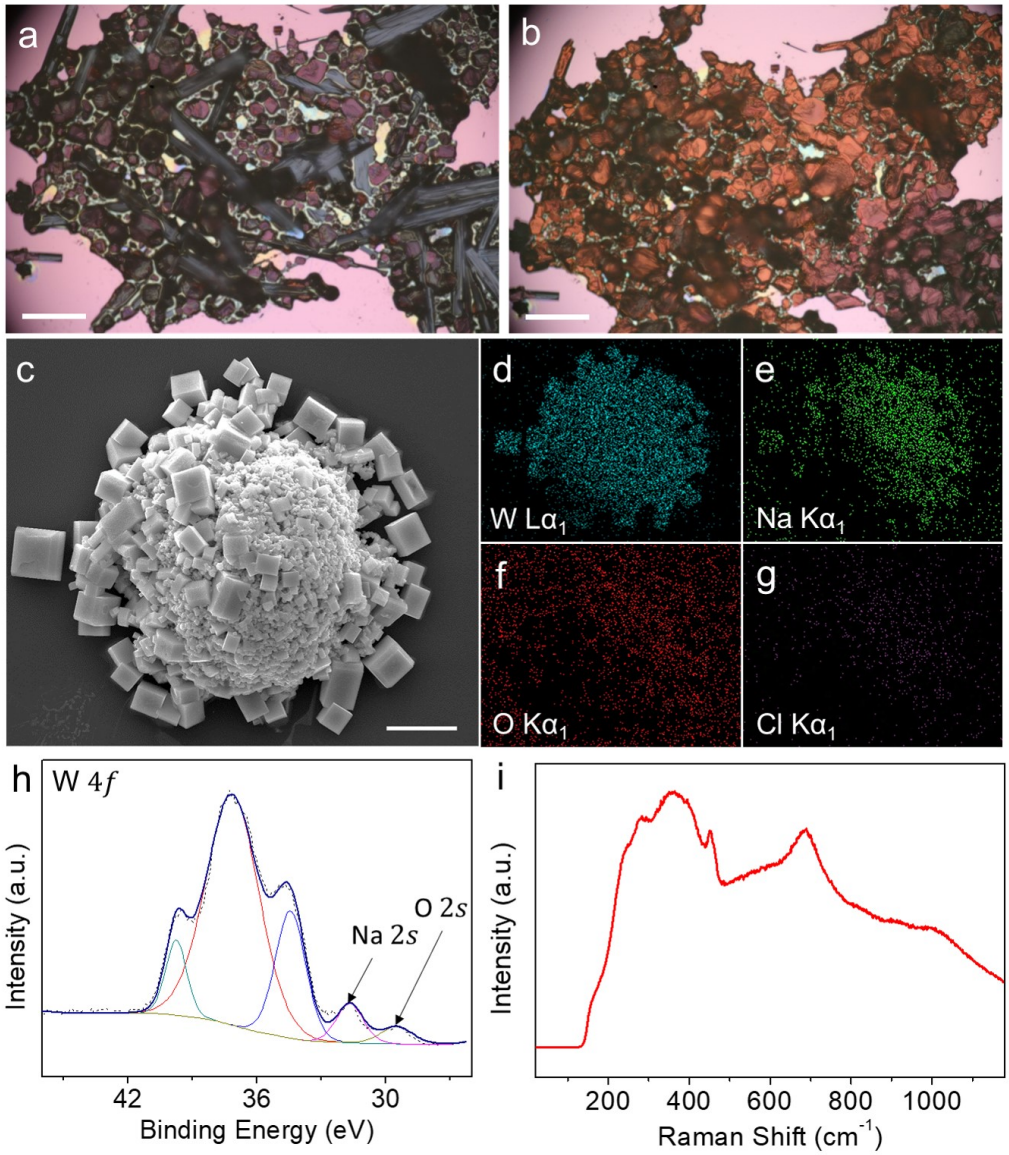

Figure 3.5: Sodium Tungsten bronze formation[29]. (a) and (b) Optical micrographs show crystals of various colors after exposing Na_2WO_4 liquid droplet to H_2. The colors we observe in these formations are consistent with the reported colors for Na_xWO_3. Scale bars are 100 μm. (c) SEM micrograph and (d-g) corresponding EDS maps. (h) XPS survey of W $4f$ high resolution scan taken from sodium tungsten bronze formation indicates that W is in +4 oxidation state. (i) Raman spectrum of sodium bronze.

molten Na_2WO_4 while the Se heater is OFF, cubic crystals varying in color from yellow to orange emerge shown in figure 3.5 (a-b). Elemental analysis by EDS (figure 3.5 (c-g)), W, Na and O are detected. According to XPS and Raman characterizations, these formations are sodium tungsten bronzes (Na_xWO_3, x < 1) of various Na ratio[41] and varying colors correspond to different x[42]. W $4f$ binding energies (figure 3.5 (h)) are consistent with the sodium tungsten bronze[43] and Raman spectrum (figure 3.5 (i)) taken from the crystals is also consistent with the Raman spectra of alkali tungsten bronzes[44]. Therefore, we determine that the temperature at which H_2 dosed during the TMDC synthesis is critical to prevent premature reduction of sodium tungstate to sodium tungsten bronze.

In the next experiment, we expose Na_2WO_4 to Se for 20 minutes, then turn off the Se heater and send H_2. However, no WSe_2 crystal is observed. This failure is due to the lack of Se in the liquid phase as confirmed by XPS and EDS analyses (figure 3.6 (a) and (b)). Even when we add Se to the $NaCl/WO_3$ mixture, no Se is detected in the liquid droplets, meaning that Se is unsolvable in Na_2WO_4. It should be note that when H_2 is introduced over hot Se vapour above 300 °C, it reacts with Se to form H_2Se gas[45], which can be imperative in WSe_2 growth.

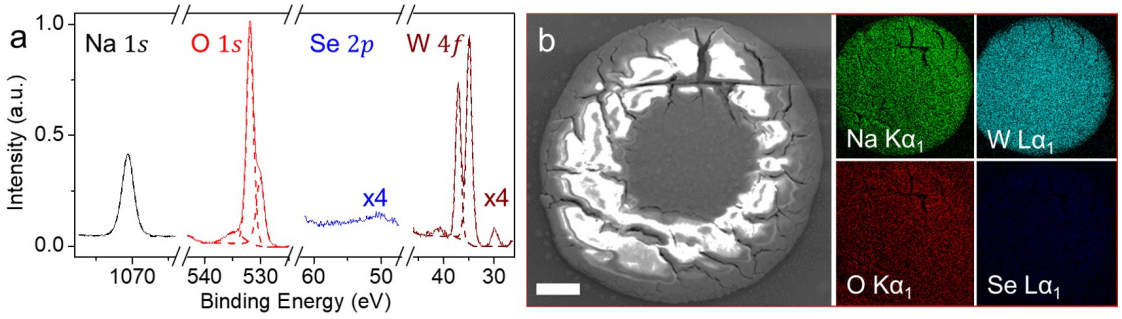

Figure 3.6: Effect of Se exposure on Na_2WO_4[29]. (a) High resolution XPS spectra of the Na_2WO_4 liquid droplet obtained after 20 minutes of exposure to Se. Na 1s, O 1s, Se 2p, and W $4f$ spectra match exactly with Na_2WO_4 spectra and no Se 2p peaks exist in the spectrum. (b) SEM image and EDS maps corresponding to the labeled elements are obtained from the solidified Na_2WO_4 liquid droplet exposed to Se for 20 minutes. The Se Lα1 map shows a faint background as the tail of the W Lα1 peak extends through Se Lα1 energy. Scale bar is 20 μm.

A series of controlled experiments are performed to unravel any possible effect

of H_2Se on WSe_2 synthesis. With the unique individual control over the heaters' temperature, we fill the chamber with H_2Se before reaching the growth temperature by playing with the introduction timing of Se and H_2. First, we evacuate the chamber and flush it with Ar several times. To form H_2Se, we fill the chamber with a $5:1$ ration Ar : H_2 until atmospheric pressure is reached and brought the temperature of the Se heater to 300 °C for Se vapour to react with H_2 in the CVD chamber. Meanwhile, the substrate temperature is kept below 300 °C to avoid any Se condensation on the substrate. The chamber is being kept for 15 minutes under this condition shown in figure 3.7 (a). Afterwards, We shut down the Se heater and ramp up the substrate heater to 750 °C (figure 3.7 (b)). Through this process, we can make sure no Se feed is present at the growth temperature and the chamber is filled mostly with H_2Se. As soon as the substrate temperature goes above 650 °C we start observing the formation of WSe_2 monolayers out of the formed Na_2WO_4 liquid (VLS) as well as at remote positions (VSS) on the substrate where no liquid can be found. To further insure that H_2Se is the main reactant with the volatile intermediate compounds, we perform the same controlled experiment in such a way that after heating the Se heater and cooling it back to the room temperature (figure 3.7 (c)), H_2 is introduced and again the substrate heater is heated to 750 °C (figure 3.7 (d)). However, such experiment does not result in any WSe_2 crystal formation. This experiment substantiates H_2Se gas as a requisite element to synthesize WSe_2 crystals both in VLS and VSS modes. Since selenium has a lower reactivity compared to sulphur[46][47], unlike sulphur based TMDC synthesis, the dependence of WSe_2 formation on H_2Se is not surprising.

With all these findings taken into account as well as intermediate formations based upon reaction (1), the proposed VLS reaction can be written as:

$$Na_2WO_4(l) + 2H_2Se(g) + H_2(g) \rightarrow WSe_2(s) + 3H_2O(g) + Na_2O \qquad (2)$$

Here, H_2Se and H_2 gases react with the liquid intermediate compound Na_2WO_4 to form WSe_2, acting as as a reducing agents to reduce W^{6+} in Na_2WO_4 to W^{4+} in WSe_2.

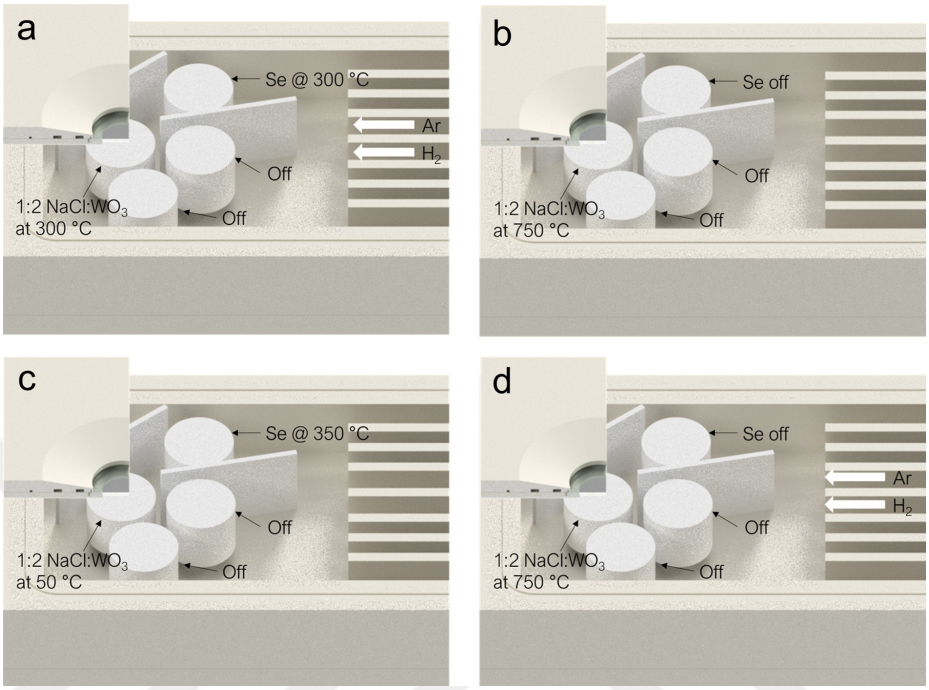

Figure 3.7: Series of controlled experiments to investigate the role of H_2 in the CVD growth process. (a) Both substrate and Se heater temperatures are kept around 300 °C while H_2 and Ar are supplied. (b) The Se heater is OFF and the substrate heater is ramped up to 750 °C in the absence of the carrier gases while the chamber exhaust is closed. (c) Heating the Se crucible up to 350 °C in the absence of H_2. (d) H_2 is introduced at the substrate temperature of 750 °C while Se is OFF.

Additionally, the VSS chemical reaction of the adsorbed molecules producing WSe_2 can be written as:

$$WO_2Cl_2(ads) + 2H_2Se(ads) + H_2(g) \rightarrow WSe_2(s) + 2H_2O(g) + 2HCl(g) \quad (3)$$

This reaction is attributed to the real time observation in which crystals appear on the substrate where no liquid phase is observed. Unlike VSS mode, crystals grow at a much faster rate in the VLS mode. This observation can be qualitatively described by the fact that in one hand, gaseous molecules (WO_2Cl_2 and H_2Se in the case of WSe_2) have to be adsorbed by the substrate surface and crystal nucleation requires a seed to begin via VSS. On the other hand, crystal growth promotes by excess supply of constituent precursors and governed by the kinetic

effect[48].

One employment of the discussed reactions (2 and 3) is promoting one mode over the other by controlling the growth parameters. For example, bottom-up directed growth of 2D materials could be achieved by directing the liquid phase into a desired pattern. The competition between reaction (1) and (2) can be governed if the gaseous adsorption or liquid condensation rates are handled. As the reaction between the metal–oxide and the salt begins, the VSS precursor is released in the gaseous form and adsorbed by the substrate surface. If no H_2 and Se is supplied in time, the adsorbed precursor molecules are desorbed from the substrate surface. While the reactants are being consumed, the partial pressure of the VSS precursor decreases due to the decay in the reaction between the salt and the metal–oxide precursors. Accordingly, by delaying H_2 and Se, the volatile intermediate gases keep leaving the system. Meanwhile, High enough partial pressure of the VLS precursor in the chamber is needed to condense liquid droplets on the target substrate. In this regard, VLS condensation rate may be tuned by quite a few parameters such as separation of the substrate from the precursor heater, carrier gas flow rate and the precursor heater temperature. More specifically for WSe_2, modifying the temperature and introduction time of H_2 and Se allow us to boost one growth mode over the other. When the precursor heater is around 600 °C and concurrently H_2 and Se are supplied, most dominantly VSS growth is elevated. Delaying the time of H_2 and Se by about 10–15 minutes while the precursor temperature reaches 700 °C results in the formation of VLS crystals predominantly. In a tube CVD furnace, such a level of control is extremely difficult since the substrate and precursor temperatures interfere in a way that any change in the precursor temperature will either affect the substrate temperature or the separation between them needs to be adjusted at a cost of reducing the amount of precursor reaching the substrate. Therefore, not only real time capturing of the growth modes is noteworthy but also the capability of the chamber to dominate one mode over the other is remarkably important.

3.3.2 Characterization of WSe_2 monolayers

Figure 3.8 (a) shows an optical image of a typical crystal synthesized in our custom CVD chamber via vapour-solid-solid route. Raman and photoluminescence (PL) intensity maps (figure 3.8 (b)) show that the crystal is uniform, and the PL spectrum is similar to that has been reported previously[49]. Raman peak positions match with the ones reported in the literature[50] (figure 3.8 (d)). Photoluminescence (PL) maps obtained from typical VSS crystals show that they are high quality WSe_2 monolayers. The PL spectrum given in figure 3.8 (e) is fitted with two Gaussian peaks: The major peak is centered around 1.621 eV with a full-width half-maximum (FWHM) of 60 meV and the secondary peak is centered around 1.550 eV with 58 meV FWHM. The stronger peak at 1.621 eV is attributed to neutral free A-excitons while the peak at 1.550 eV is attributed to the trions. In WSe_2 mechanically cleaved from the bulk, trion peak is closer to the exciton peak in energy and the exciton peak is located around 1.658 eV. However, our measured values are very typical of CVD synthesized WSe_2 monolayers[51][52][53]. The relative peak shifts compared to the exfoliated samples can be explained by the stress induced on the crystals due to the thermal expansion coefficient differences between the substrate and the WSe_2 crystals. AFM topography (figure 3.8 (f) and (g)) shows that the monolayer WSe_2 has a thickness of ≈ 0.75 nm, further confirming monolayer formation[54].

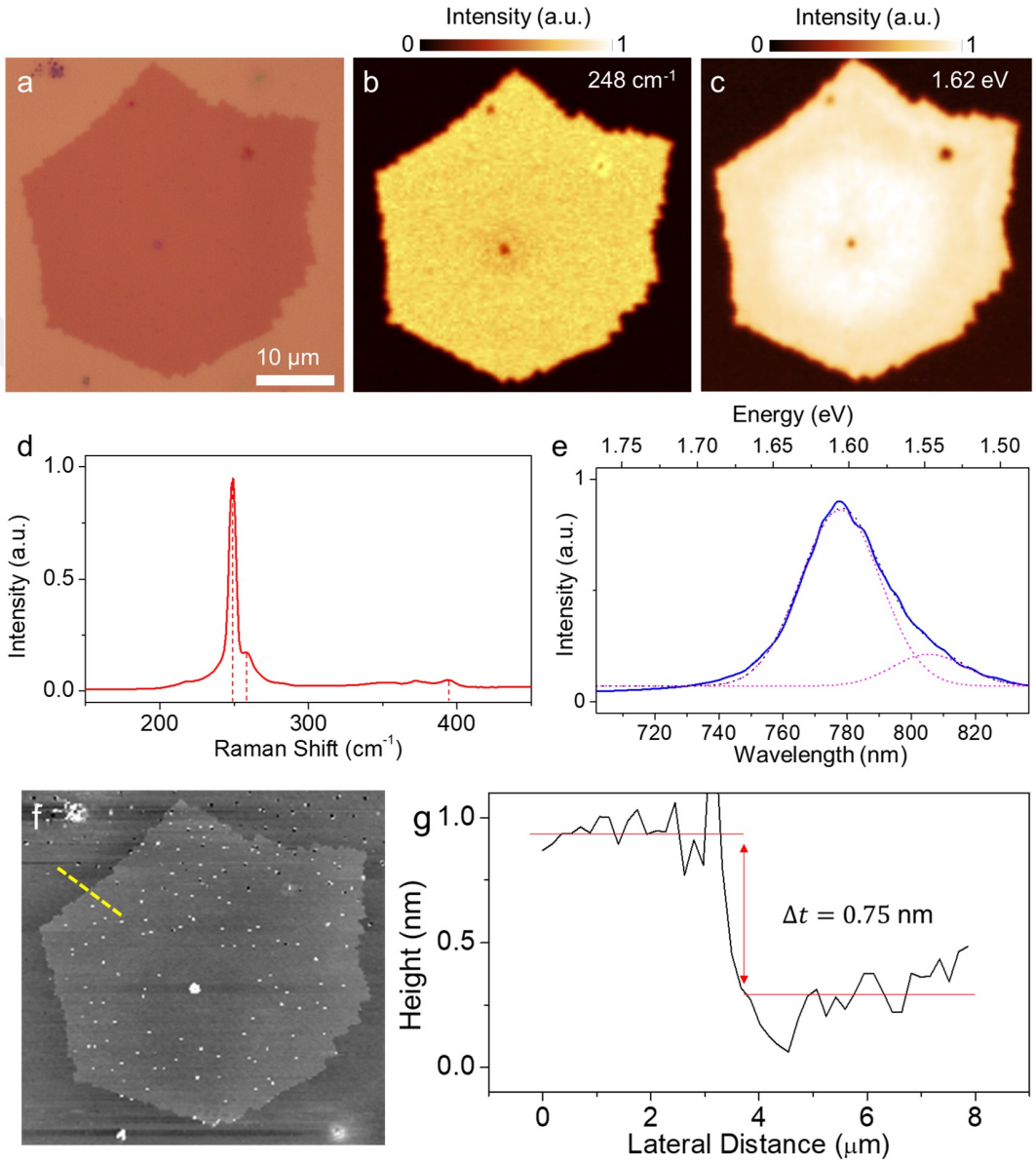

Figure 3.8: Characterization of a typical WSe_2 monolayer[29]. (a) Optical microscope image of a typical crystal is given. (b) Raman (248 cm^{-1}) and (c) PL (1.62 eV) intensity maps show the high uniformity of the crystals. (d) Raman spectrum taken from a point on the crystal shows the typical Raman features of the monolayer WSe_2. (e) PL spectrum taken from a point on the crystal is similar to the previously reported CVD grown monolayers of WSe_2. Gaussian fits to the spectrum are represented by purple dotted lines and their sum is by black dotted line. (f) AFM height map and (g) the height trace taken along the yellow dashed line in (a) shows that the apparent thickness of the crystal is 0.75 nm.

Crystals formed via VLS mode typically have much poorer crystal quality, most often composed of multi-layered regions and the crystals are polycrystalline with multiple defects. Figure 3.9 (a) shows an optical image of a crystal grown within HfO_2 on SiO_2 channels (50 nm deep, 5 μm wide) via directing the VLS liquid into the channels before introducing H_2 and Se. The Raman intensity map shows intensity variations across the crystal (figure 3.9 (b)); however, the peak position stays the same. Similarly, PL intensity and FWHM varies significantly across the crystal (figure 3.9 (c)). The PL peak is significantly reduced and shifted to 1.568 eV. The PL intensity and FWHM vary significantly across the crystal (figure 3.9 (d)). Such variations due to the defective nature of VLS formation can be further rehabilitate via using pure non-volatile alkali molybdates and tungstates as the VLS growth feed[55].

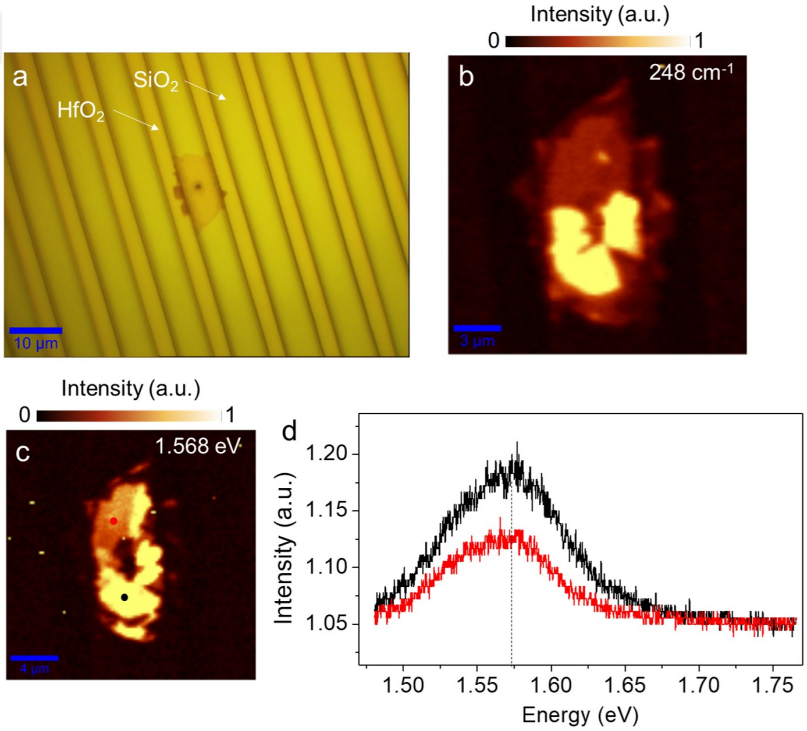

Figure 3.9: Raman and PL characterization of a VLS grown WSe_2 monolayer[29]. (a) Optical microscope micrograph of a crystal formed via guiding the liquid phase within the channels of HfO_2 on SiO_2. (b) Raman intensity map of 248 cm^{-1} peak indicating dramatic intensity variations across the sample. (c) PL intensity map integrated at 1.568 eV. As comparison to VSS formed crystals, the peak position is very much shifted and the FWHM is larger (d) PL graphs taken from the marked locations on (c).

3.3.3 Characterization of $MoSe_2$ monolayers

The methodology we present here can be applied to any other TMDCs such as $MoSe_2$ as a Molybdenum chalcogenide exemplary. Using mixture of MO_3 and NaCl (1:5), we synthesize $MoSe_2$ monolayer crystals along with the same VSS/VLS observation as WSe_2 crystals. Figure 3.10 (a) shows an optical picture of typical $MoSe_2$ crystals formed via VSS growth mode. AFM measurements given in figure 3.10 (b) depicts a monolayer thickness of 0.72 nm. Raman and PL maps ((c) and (d)) confirm that the crystal is a uniform $MoSe_2$ monolayer, matching the previously reported ones[56][57].

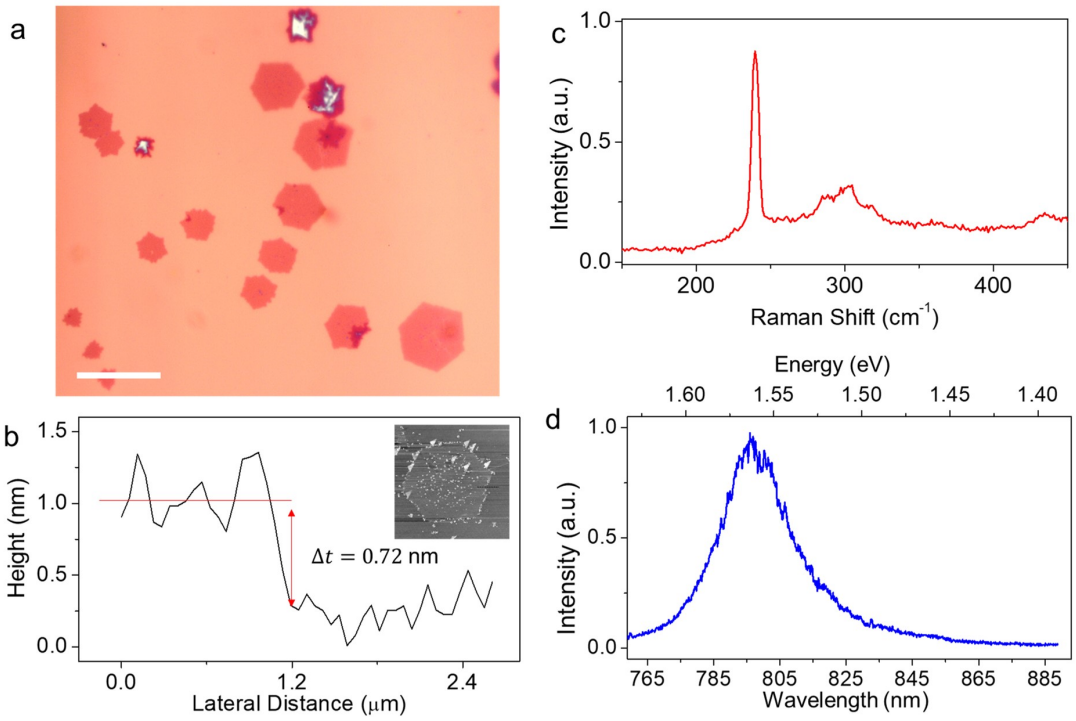

Figure 3.10: Raman, PL and AFM characterization of a typical $MoSe_2$ monolayer[29]. (a) Optical micrographs of hexagonal $MoSe_2$ monolayers on SiO_2/Si. The scale bar is 20 μm (b) AFM height trace taken along the dashed line in the inset topography map shows that the average height of the crystal is 0.72 nm. (c) Raman and (d) photoluminescence spectra, consistent with the CVD grown $MoSe_2$ monolayers.

3.3.4 Lateral and vertical $MoSe_2/WSe_2$ heterostructures

To further demonstrate the versatility of our chamber, we synthesize $MoSe_2/WSe_2$ heterostructures both in lateral and vertical configurations equipped with the real time observation and analysis of the growth. Our ability to control the heaters independently enables *in-situ* control of the heterostructure synthesis. Heater 1 and 3 are dedicated to Se (10 mg) and MO_3 (10 mg) respectively. Mixture of NaCl:WO_3 (less than a mg) is placed at a corner of the substrate to enhance the mass transport of WO_2Cl_2 (figure 3.11 (a)). While heater 1 and 3 are kept at 300 and 600 °C, respectively, the substrate heater is ramped up to 550 °C. At this stage, H_2 is introduced into the chamber to elevate the formation of H_2Se for $MoSe_2$ synthesis. After obtaining several micrometers large $MoSe_2$ monolayers, The heater 3 and H_2 flow are shut down to terminate the $MoSe_2$ growth. Subsequently, WSe_2 growth is initiated by ramping up the substrate heater to the desired temperature which determines the lateral or vertical layout of the final heterostructure. WSe_2 is reintroduced for WSe_2 formation until the end of the synthesis.

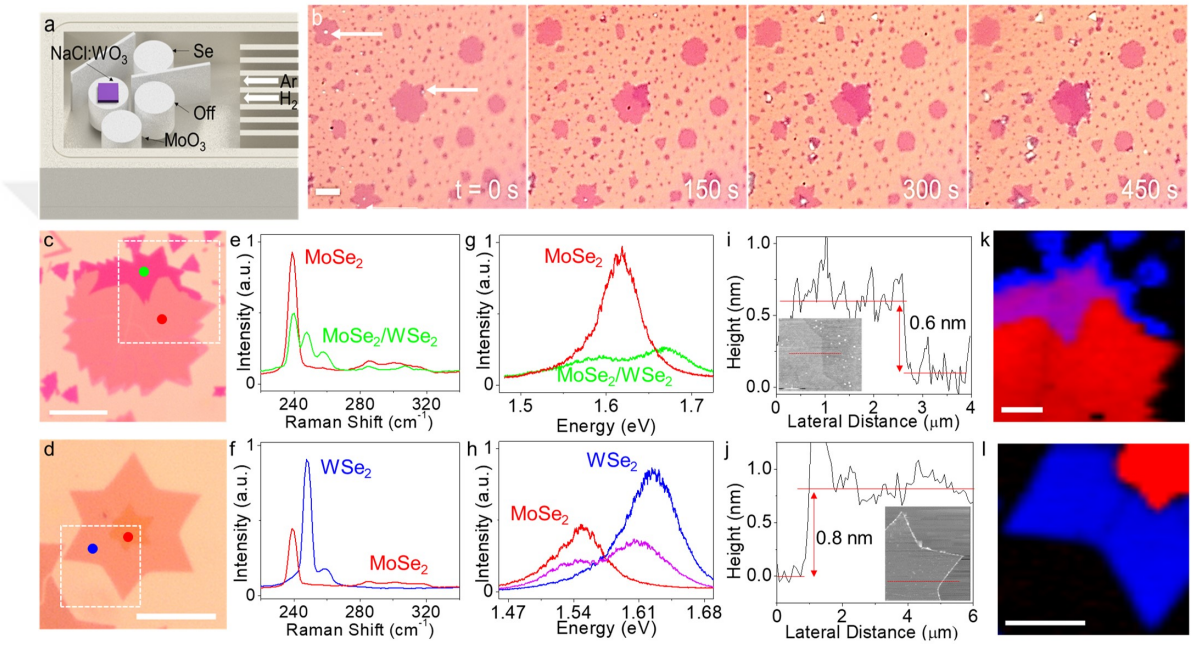

Figure 3.11: Real time observation and control of heterostructure synthesis. (a) Schematic shows the configuration of the CVD chamber for the heterostructure synthesis[29]. (b) A series of images obtained at 700 °C demonstrating the formation of WSe_2 on the $MoSe_2$ monolayer. The white arrows indicate the seeds and how the WSe_2 top layer generates from it. Scale bar is 10 μm. (c) and (d) show optical microscopy images of vertical and lateral heterostructures, respectively. Scale bars are 10 μm. (e) and (f) Raman and (g) and (h) PL spectra obtained from the locations in (c) and (d) marked with colored circles. PL spectra in purple in (h) are obtained from the interface between $MoSe_2$ and WSe_2. (i) and (j) AFM height traces obtained along the red dashed line in the inset show the vertical and lateral heterostructures. (k) and (l) Raman intensity maps for the vertical and the lateral heterostructures at 239 cm^{-1} (red) and 248 cm^{-1} (blue) obtained from the area marked by white dashed rectangles in (c) and (d). Purple region in (k) is due to the overlay of the red and blue maps as in this region of the heterostructure, we observe both 239 and 248 cm^{-1} peaks. Scale bars are 2 μm.

The evolution of the vertical heterostructure growth in time captured at 700 °C is shown in a series of real time optical microscopy images given in figure 3.11 (b). Some small droplets indicated with the white arrows in figure 3.11 (b) are observed upon heating the substrate heater where W source is injecting after $MoSe_2$ growth termination. We stop the synthesis as the droplets form and characterize them using Raman spectroscopy. As expected, the Raman spectra from the frozen droplet matches with the Na_2WO_4 as shown in figure 3.12.

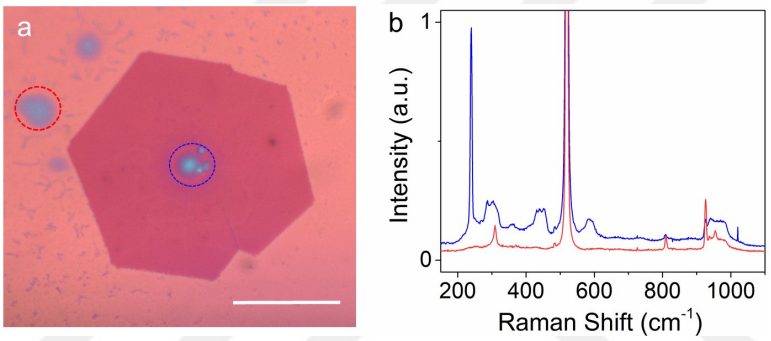

Figure 3.12: Vertical heterostructure intermediate state[29]. (a) Optical microscope image of a Na_2WO_4 droplet on $MoSe_2$ monolayer. The scale bar is 10 μm. (b) Raman spectra taken from the dashed circles in a match with the Raman spectrum of Na_2WO_4. Extra peaks in the blue Raman spectrum are from the $MoSe_2$.

Interestingly, we see the droplets formation either at the edge or at the center of the $MoSe_2$ monolayers, but never in between. At this stage, when we introduce H_2, the WSe_2 layer nucleates from the liquid phase at much slower rate compare to the monolayer TMDC growth. Results of Raman, PL and AFM analyses of both vertical and lateral heterostructures are shown in figure 3.11 (c-l), all indicating growth of the WSe_2 monolayer along the edge or on top of the $MoSe_2$ monolayer. Our studies show that substrate temperatures below 725 °C mostly yield vertical, while above 750 °C mostly yield lateral heterostructures, which can be explained by the kinetic nature of the crystal formation. The mentioned temperatures are high enough to trigger the efficient reaction between NaCl and WO_3. Accordingly, at this moment in time, there are plenty of VLS and VSS precursors available for the crystal nucleation. Therefore, unlike previous studies reporting the deterministic role of precursor supply, the substrate temperature dictates the heterostructure type preferably.

Chapter 4

Synthesis of V_2O_3 nanoplates for the exploration of the correlated supercritical state

The previous chapter highlights the capability of the real-time observation chemical vapor deposition method (RTO-CVD) to explore the growth mechanisms and synthesis of various TMDC monolayers as well as their heterostructures. The RTO-CVD is a powerful platform to synthesize less/unknown materials. Here, for the first time, we show synthesis of single crystalline V_2O_3 nanoplates whose growth recipe has been developed via RTO-CVD. The 2D characteristic of the CVD grown V_2O_3 crystals allows us to study their peculiar electrical and physical properties such as metal-insulator transition (MIT) and supercritical state. High-quality V_2O_3 nanoplates introduced in this chapter can be both tensile and compressively stressed. The results emphasize the practical efficacy for studying the physics of the supercritical state and the phase stability of V_2O_3 to enable new horizons in applications.

4.1 Introduction

One of the most versatile oxides, vanadium (V) as a multivalent transition metal exists in various valence states such as V^{+2}, V^{+3}, V^{+4}, V^{+5}, and more[58]. A large variety of stable and metastable structures of vanadium oxide, each of which possesses different crystal structures, leading to distinct physical and chemical properties suitably employed for various applications. Vanadium oxides are renowned for displaying peculiar properties due to the unpaired d-electrons in vanadium's valance. Accordingly, their functionalities can be tailored due to the strong electron-lattice interactions and electron-electron correlations. Interplay among the internal degrees of freedom, such as spin, charge, and orbital leads to rich electronic phenomena, such as metal-insulator transition (MIT)[59], unusual quantum spin states[60][61], and superconductivity[62]. Such phenomena are quite complicated to be fully recognized. This complexity arises from the lack of consistency in crystalline state, oxygen non-stoichiometry, and doping. For instance, the magnitude of the MIT transition and the narrowness of the hysteresis loop (due to the latent heat) vary with the stoichiometry discrepancy. Even small stoichiometric deviations destroy the sharpness of the transition and increase the hysteresis width[63]. In addition, crystalline state of the vanadium oxides matters a lot as polycrystalline material will have a broader transition than single crystals[64].

Furthermore, the vanadium oxides physical and electrical properties are remarkably sensitive to the external stimuli, such as temperature, stress, and doping. If studied in bulk or thin film samples, multiple problems emerge such as various phase and domain formations in view of non-uniform strain and compositional variations due to local doping and oxygen vacancies[65][66]. One robust solution for the mentioned challenges is developing nanostructured vanadium oxides and take advantage of crystals that are smaller than the characteristic domain size[67][68][69]. Nanoscale samples, thus making it possible to explore the fundamental properties in details, especially realizing the MIT transition nature without criticizing irreproducibility between samples and non-uniform stresses

producing mechanical degradation[70]. With all these taken into account, synthesis of nanosclae vanadium oxides is the essence of demand.

A large varieties of versatile vanadium oxide nanostructures have been synthesized using different synthesis techniques. To name but a few, simple precipitation[71], hydrothermal synthesis[72], electrospinning[73], sol-gel technique[74], chemical vapour deposition[75], physical vapour deposition[76], pulsed laser deposition[77], atomic layer deposition[78], and magnetron sputtering[79] techniques used to develop numerous nanostructures such as nanosheets, flowers, rods, wires, and fibers. CVD technique is usually used to synthesize pure and high-quality materials with better performance. Recent discovery of the CVD growth recipe for growing the nanoscale crystals, revitalized the interest in VO_2, especially with regards to the MIT. For instance, it lights up insight into realizing photoresponse, phase diagram and hydrogen doping of VO_2 nanocrystals[80]. However, such a growth intuition is lacking for V_2O_3. Attempts to explore the MITs and criticality in V_2O_3 have been mainly focused on bulk and thin film samples, so their nature has remained more elusive. Further complications arise in film samples due to polycrystallinity of the films and nonuniform stress due to the substrate adhesion as well as lattice mismatch-induced stresses in epitaxially grown films. Similarly, bulk crystals of V_2O_3 present other challenges, such as defects in the crystal, impurities and domain structure generating irreproducible results[81][82]. To the best of our knowledge, so far, no free-standing high-quality crystals smaller than the characteristic domain size have been available for V_2O_3 due to the synthesis challenges. Hence, the immense potential to study the criticality of the Mott transition has not been fully appreciated[83], and the precise details of the phase diagram are still inexplicit[84]. Here, as the pioneers, we succeed a route to synthesize high-quality layered V_2O_3 single crystals of a few nanometer thickness via RTO-CVD, and study some novel aspects of the phase transitions.

4.2 Experimental method

X-ray Photoelectron Spectroscopy (XPS) analysis is performed using K-Alpha X-ray photoemission spectrometer by Thermo Scientific. X-ray diffraction measurements are taken using XRD Panalytical MRD X'pert Pro diffractometer. Selected Area Electron Diffraction (SAED) and High Resolution Transmission Electron Microscopy (HR-TEM) measurements are taken using FEI Technai G30. As-grown crystals are transferred on holey carbon or Silicon Nitride grids using both micromanipulator and wet transfer methods. In the wet transfer method, growth substrate is coated by a thin Cellulose Acetate Butyrate (CAB) film and baked at 150 °C for 5 minutes. Then, the film is removed via wedging into water and the film is transferred on to target substrate. Finally, the film is dissolved in Ethyl acetate for 15 minutes leaving the crystals on the target[85]. Atomic Force Microscopy (AFM) is employed on both as-grown and transferred crystals. Wavelength Dispersive X-ray Spectroscopy (WDXS) and Energy Dispersive X-ray Spectroscopy (EDXS) are used to characterize the as-grown crystals and the intermediate compounds, respectively along with Scanning Electron Microscopy (SEM) to image them. Raman measurements are taken using 532 nm excitation laser focused to a diffraction limited spot. Laser power is kept low enough to restrict photothermal heating. Two and four terminal devices of V_2O_3 are prepared using standard optical or electron beam lithography methods. Once the crystals are patterned, they are dipped in buffered oxide etched for a few seconds to remove oxides from the crystal surface for lower contact resistance. Au/Cr layer of 100/5 nm thickness is deposited using thermal evaporation. No difference observed for devices prepared with Au/Ti of the same thickness with electron beam evaporation. TEM samples are prepared both on silicon nitride membrane and holey carbon grids. Transfer techniques described above is used to prepare the samples. Cross-sectional TEM images are taken through samples prepared by Focused Ion Beam (FIB) etching and deposition. We perform low temperature electrical measurements in four-terminal geometry using Cryogenic Limited Physical Property Measurement System (PPMS). A closed circuit Helium system is used to lower the temperature. The devices are wire boned to the PPMS 6 pin sample holder using wirebonder iBond5000. We source current and

measure voltage from the the outer terminals and measure the voltage drop from the inner contacts to calculate the resistance across the inner terminals.

4.3 Result and discussion

4.3.1 Synthesis of V_2O_3 nanoplates

V_2O_3 synthesis is developed in the RTO-CVD chamber allowing real-time optical observation and control of the synthesis[29]. A mixture of KI:V_2O_5 is milled together in the weight ratio of 2:1 and a few fine granules are placed directly on a c-cut sapphire substrate. Then, the chamber is vacuumed to 10^{-3} mbar and flushed with Ar several times. The growth takes place at an atmospheric pressure of Ar. Once 660 °C is reached, the precursor mixture starts melting and 20 sccm H_2 gas flow is turned on while the stage temperature is ramped up to 850 °C. 10 minutes after the introduction of the H_2 gas, crystals of varying thicknesses grow from the supersaturated droplets in a period of 5 minutes. Once all the droplets are consumed, H_2 flow is shut down and the chamber is cooled down at a controlled rate (40 °C/min). A series of real-time optical microscope images captured during the growth within 810-850 °C given in figure 4.1 (a-d), demonstrating the formation of the crystals out of the supersaturated droplets (indicated by blue arrows) with the passage of time. Even though *in-situ* monitoring of the synthesis allows us to determine the growth conditions guiding to V_2O_3 nanoplates and develop the growth recipes, any conventional split tube furnace can be used for the nanoplate synthesis.

4.3.2 V_2O_3 growth reaction analysis

With the unique real-time monitoring feature of the chamber, we can observe the molten intermediate compounds and stop the reaction at any temperature to characterize them. Potassium iodide (KI) salt reacts with V_2O_5 at elevated

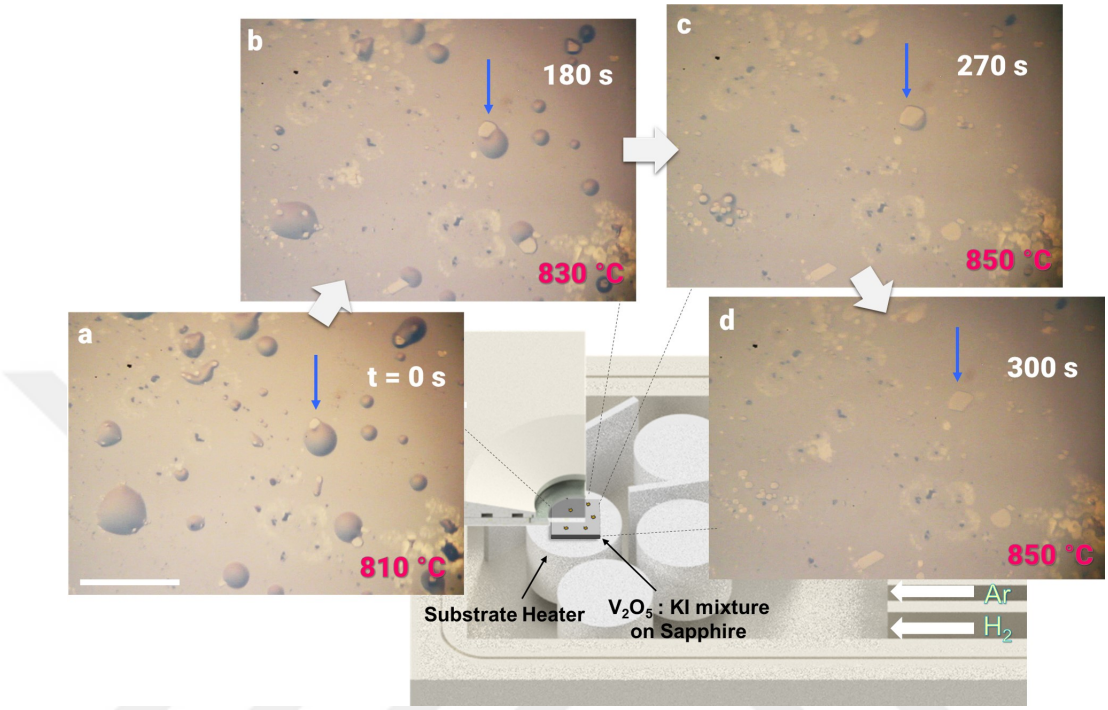

Figure 4.1: A series of optical microscope micrographs taken during the salt-assisted synthesis show the crystal formation stages. Images are taken from 810 °C to 850 °C, and the beginning of the observation in (a) is marked as time zero. As the time passes by (b) and (c), thin crystals nucleate from the liquid flux until fully solidification (d). The blue arrows indicate an exemplary crystal formation. The scale bar is 50 μm.

temperatures to form potassium vanadate (KV_3O_8)[86], an intermediate liquid compound that can be further reduced to V_2O_3 with H_2. This chemical route results in much higher-quality crystals as compared to the direct reduction of via H_2 and sulfur[87] or a reduction of V_2O_5 in molten potassium fluoride[88]. To analyze the intermediate compounds and compile the reaction route, followed by the normal growth recipe, we heat the chamber to 700 °C, and watch reaction to take place. Once a droplet is formed, we shut down the furnace and characterize the intermediate compound using EDS, XPS and Raman. EDS maps shown in figure 4.2 (a-f), reveal the constituent elements of the droplet. K, V and O dominates the spectra with Al signal outside of the droplet coming from the growth substrate. Raman spectrum from the droplet matches very well with KV_3O_8[86] and +5 oxidation state of V from XPS is consistent with the potassium vanadate in the literature[89].

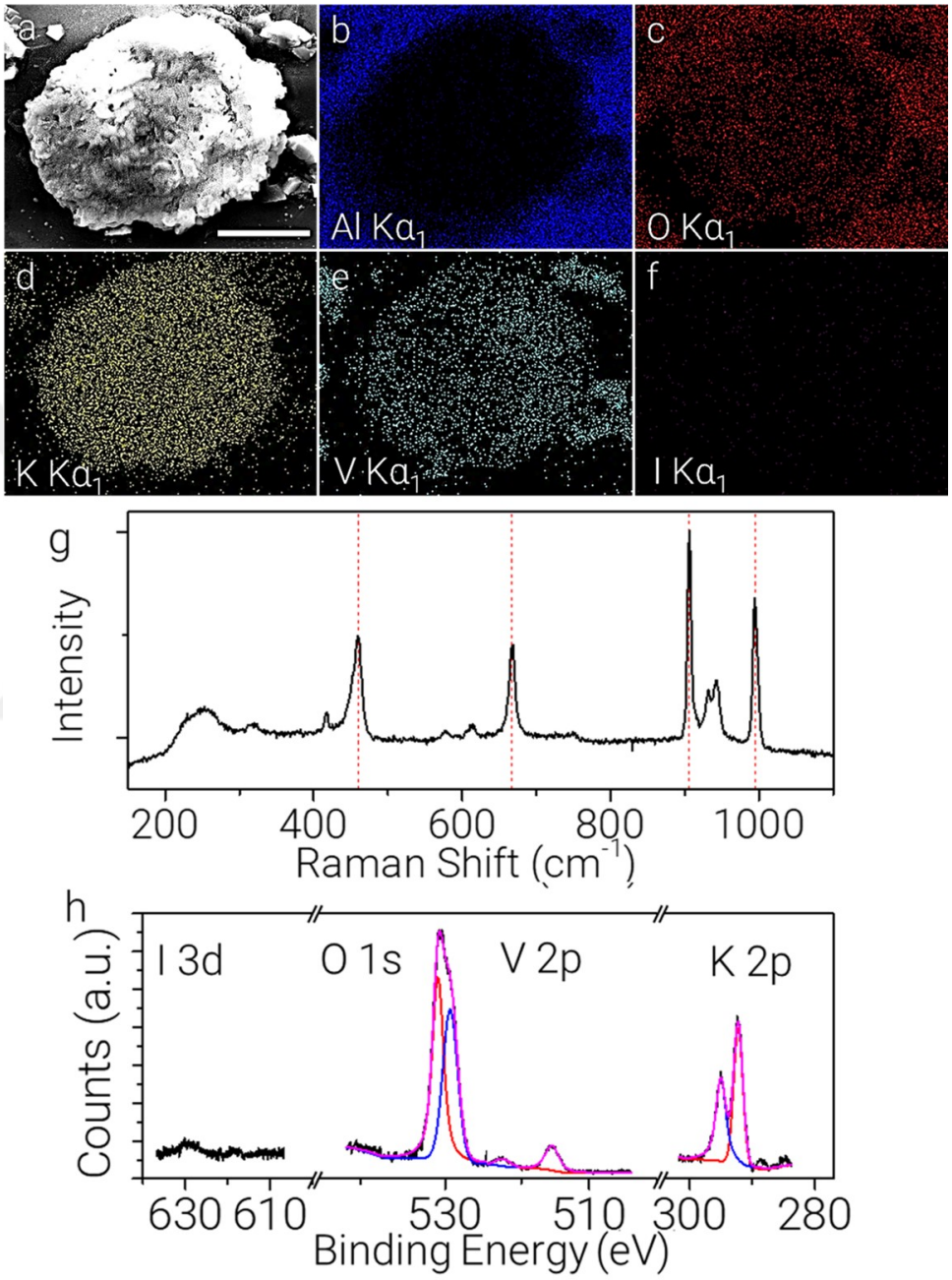

Figure 4.2: Characterization of the solidified intermediate compound[90]. (a) SEM image of a typical molten intermediate compound after solidification. Scale bar is 5 μm. (b-f) EDS maps for various elements. The intermediate compound contains O, K and V and no I. Al Kα1 signal comes from the sapphire substrate. (g) Raman spectrum taken from the intermediate compound shows typical Raman modes for KV_3O_8[86]. These modes are marked by red dashed lines. (h) XPS surveys for I 3d, O 1s, V 2p and K 2p consistent with the EDS and Raman spectra. Fittings to the O 1s and V 2p match with the binding energies of KV_3O_8[89].

V_2O_3 crystals form via reduction of KV_3O_8 under reducing H_2 environment. We also introduce Se in some trials to form H_2Se as a stronger reducing gas; however, no significant difference is observed in crystal morphologies. According to the intermediate growth analysis, the following reaction for the crystal formation can be proposed:

$$2\ KV_3O_8(l) + 6\ H_2(g) \rightarrow 3\ V_2O_3(s) + 6\ H_2O(g) + K_2O(s) \qquad (1)$$

This proposal is based on the observation that we encounter very small amount of K on the surface of the growth substrate. KOH would evaporate at the growth temperature and K_2O_2 readily decomposes into K_2O above 500 °C. Thus, such a reduction route is plausible.

4.3.3 Characterization of V_2O_3 crystals

A typical microscope micrograph of the as-grown crystals is shown in figure 4.2 (a). Figure 4.2 (b-c) shows optical images taken after transferring the V_2O_3 crystals into Si/SiO_2 substrate using the transfer method discussed in section 4.3. The transferred crystals typically have a few nanometer thin layers attached to the thicker crystals[85]. More strikingly, images obtained by SEM given in figure 4.2 (d-f) reveal layer-by-layer growth of the crystals. Such observations is due to the growth kinetics, commonly observed in the crystal formation from supersaturated liquid precursors[91] in which the solute particles energetically favor to couple to the kinks rather than the flat surfaces, manifesting itself as the growth in steps. This explains the ability of the crystals to be mechanically exfoliated, thus obtaining non-uniform multilayered crystals after the transfer process. Although no van der Waals force exists between these layers, such an exfoliation from non-van der Waals stacked sources is not too unforeseen. To name but a few as examples, hematite with the same crystal structure as the metallic phase of V_2O_3, and ilmenite 2D layers have been obtained via liquid phase exfoliation[92][93].

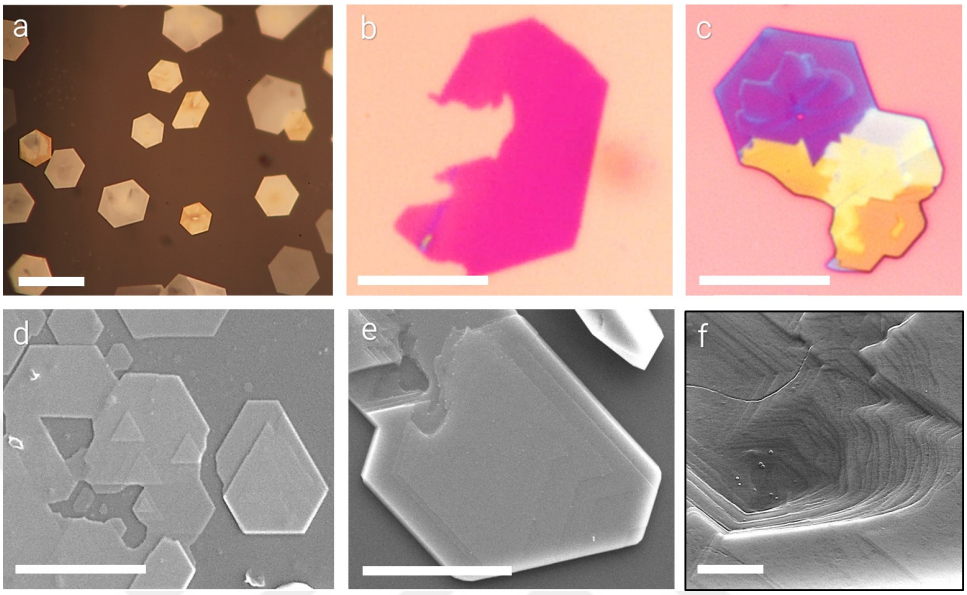

Figure 4.3: Optical and SEM imaging of the as-grown and the transferred V_2O_3 crystals[90]. (a) The optical microscope micrographs shows crystal formations of various thicknesses on sapphire substrate. (b-c) The optical microscope micrograph of V_2O_3 nanoplates transferred on to an oxidized Si chip, showing the crystal mechanically exfoliated from the substrate. (d-f) The SEM micrographs depicting layer-by-layer growth with a close-up view of the edge of a crystal in (f). The scale bars for (a-e) and (f) are 20 μm and 1 μm, respectively.

Atomic Force Microscopy (AFM) measurements are performed in details on the as-grown and transferred crystals, indicated in figure 4.4. Various height profile analyses taken from different crystals show that the minimum step height among the layers is 0.6 nm.

The chemical composition of the synthesized crystals is studied using XPS and WDS. XPS surveys (figure 4.5 (a-c)) confirm the presence of O, V, and Al yet no I and K for the samples when rinsed with de-ionized water[94][95]. For unrinsed samples, K peak is detected in the XPS spectrum; however, after 1 second etch with 1 keV argon ions, K peak vanishes, indicating remnants of the reaction by-product on the sample surface. No further potassium is observed in the depth of the crystals as determined by further depth profiling with XPS via Ar ion milling. This is expected since K atoms would be excluded from the V_2O_3 lattice due to their large size[96], consistent with the WDS result. The absence

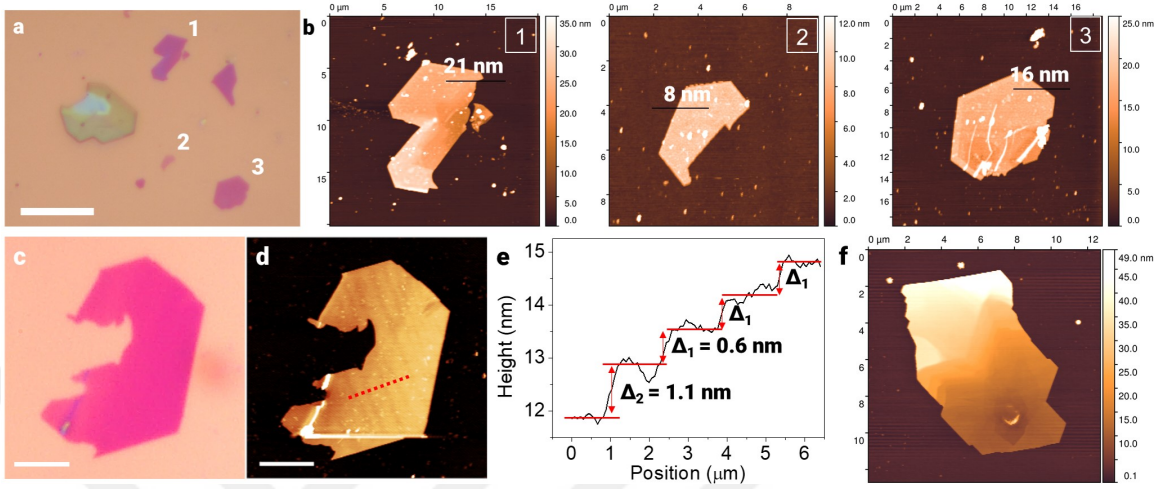

Figure 4.4: AFM analyses of V_2O_3 crystals[90]. (a) Optical microscope micrograph of transferred thin V_2O_3 crystals. The scale bar is 20μm. AFM maps corresponding to each numbered crystal are given in (b) with the noted thickness on the crystal. (c) Another crystal transferred on to SiO_2 with the corresponding AFM height trace map shown in (d). The scale bar is 5μm. (e) Height profile taken along the red dashed line shows steps of 0.6 nm along the crystal. (f) AFM height trace map of an as-grown crystal with thickness ranging from 10 to 40 nm. Layered structure is clearly visible from the map.

of the salt elements in V_2O_3 crystals further suggests the assisting role of KI in the CVD process. Al 2p and O 1s peaks are due to the sapphire substrate. XPS spectra of V 2p peaks confirm that vanadium is in 3+ valance state[97] with a slight native oxide formation that can be removed by Ar ion milling as shown in figure 4.5 (a). Ar ion milling results in the formation of V 2+/1+ and V 0 states on the surface[95]. Peaks in the pristine sample are referenced with respect to C 1s surface advantage peak. After milling, due to the loss of C 1s reference, we use O 1s predominantly coming from the sapphire substrate for the reference point. Reference material reported for V 2+/1+ is a V_2O_3 pellet bombarded with Ar ions for various durations. As the etch time goes on, the V0 peak becomes more pronounced. XPS spectrum taken at the valence-band edge on the as-grown V_2O_3 shows the insulating behavior of the crystals as there is no spectral weight at the Fermi level (figure 4.5 (c)). The spectrum is identical to that taken over the bulk insulating samples[94]. The shoulder that starts around 10 and diminishes at 12 eV belongs to the sapphire substrate[98].

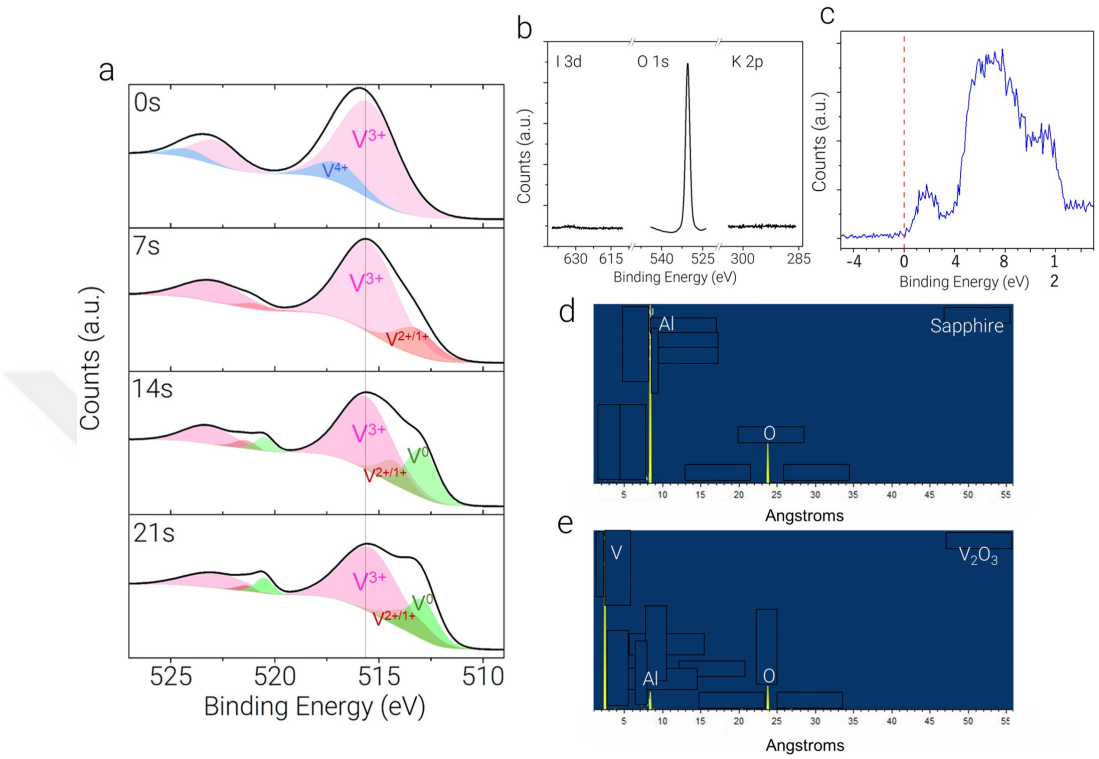

Figure 4.5: XPS and WDS analyses on the as-grown V_2O_3 crystals[90]. (a) XPS spectra of the V 2p peaks taken from pristine samples and samples etched for several seconds. Fittings to the spectra by V 2+/1+, 3+, 4+ and metallic states are given by red, pink, blue and green filled curves, respectively.(b) XPS surveys of I 3d, O 1s and, K 2p peaks indicate no presence of I and K. O 1s peak is dominated by the binding of O in the substrate as the surface coverage of V_2O_3 crystals are low. (c) Valence-band XPS spectrum taken from the as-grown crystals. (d) WDS spectrum from the sapphire substrate yields peaks for Al and O. (e) WDS spectrum taken from a V_2O_3 crystal shows peaks for V, O and Al. Al and O is due to the substrate.

WDS spectra show only V and O in abundance, taken from a few tens of nanometer thick crystals. Al and some O results from the substrate. Even when we use H_2Se as the reducing agent for the synthesis, no Selenium is detected in the spectrum.

To further characterize the crystal structure and crystallinity of the nanoplates, we perform transmission electron microscopy (TEM) and selected area electron diffraction (SAED) on V_2O_3 nanoplates transferred to holey carbon and silicon nitrite TEM grids. Figure 4.6 (a) shows a representative HR-TEM image with an

evident close-packed structure along with the corresponding SAED pattern shown in figure 4.6 (b). When the zone axis is perpendicular to the sample surface, a sixfold symmetric arrangement is recognized with d spacing of 2.5 Å for the $(10\bar{1}0)$ plane. This is consistent with the XRD measurements as the corundum c axis points perpendicular to the nanoplate surface. However, such a pattern can be attributed to fcc or bcc structure, thus further SAED analyses at different zone axes are required to distinguish the accurate structure, which will be discussed later in this chapter.

X-ray diffraction (XRD) results (figure (d-e)) confirm the c axis of the sapphire substrate and the synthesized crystals are parallel to each other[99]. θ-2θ scans around the (0006) reflections of the sapphire and V_2O_3 show that the corundum c-axis is orientated perpendicular to surface. We assign the peaks at 41.7° to (0006) plane of the sapphire substrate as they are missing in the grazing incidence XRD diffraction. The remaining peak at 38.7° matches very well with those reported for V_2O_3 on α-Al_2O_3[100] (ICDD card no. 04-002-9108). With regard to any miss-orientation of the as-grown crystal, rocking curve scan (ω-scan) of the V_2O_3 (0006) reflection results in a very sharp peak with a full width half maximum (FWHM) = 0.12°. This shows corundum c-axis of the crystals is perpendicular to the c-plane sapphire surface.

The V_2O_3 nanoplate growth on the sapphire surface can be considered as an incommensurate van der Waals epitaxy[101]. The lattice mismatch between the c-cut sapphire and V_2O_3 would result in 4.1% biaxial in-plane tensile strain. However, as will be discussed in the Raman section, this level of strain is unlikely[102]. I would like to emphasize one more time that V_2O_3 crystals can be mechanically removed from the substrate surface. Another experiment supporting the incommensurate van der Waals epitaxy is our failed attempts to grow V_2O_3 crystals on various substrates such as SiO_2, Si and quartz.

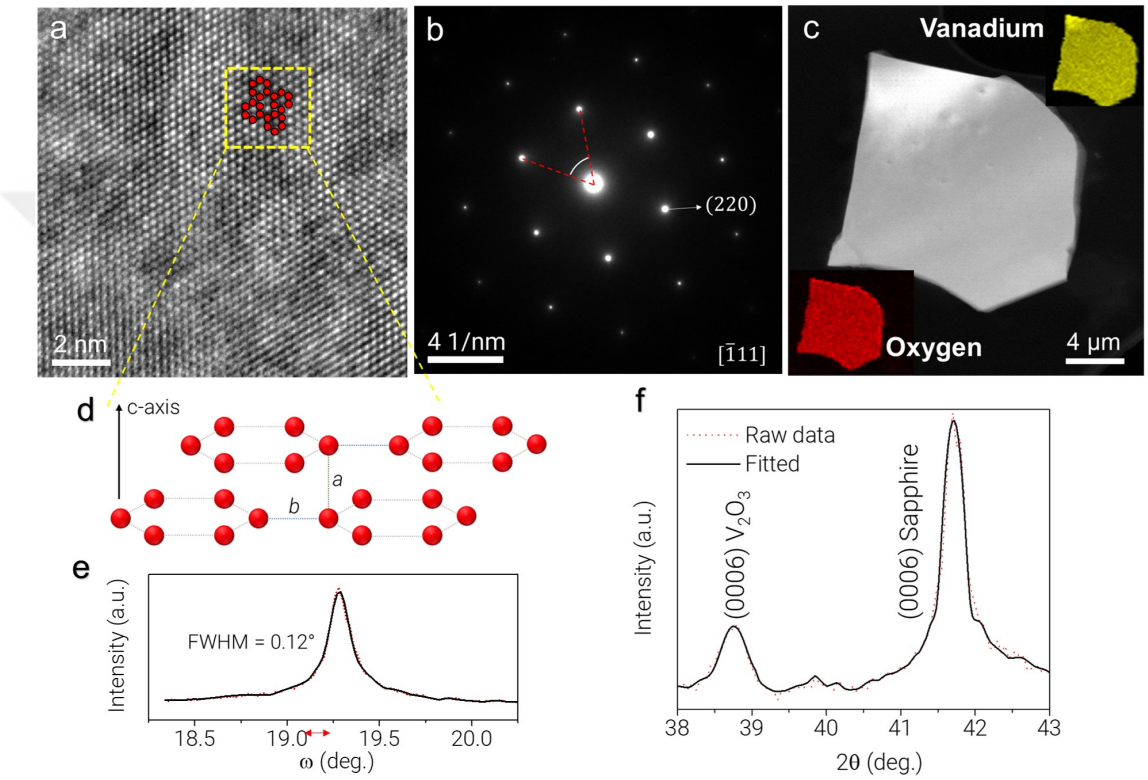

Figure 4.6: TEM and XRD analyses of V_2O_3 crystals[90]. (a) High-resolution TEM image of a V_2O_3 crystal. The evident close-packed structure is marked with red circles. (b) Sixfold symmetric SAED pattern indexed according to the fcc [$\bar{1}$11] direction. However, the same pattern is produced for the hcp [0001] direction. The lengths of the red dashed lines are 4nm^{-1}, corresponding to 2.5 Åd spacing along (220) fcc or (10$\bar{1}$0) hcp planes. (c) HR-TEM image of a V_2O_3 crystal and its corresponding EDS elemental maps in the insets, showing a uniform distribution of V (yellow) and O (red) all over the crystal. (d) Sketch of the arrangement of vanadium atoms in the corundum phase. a and b indicate the lattice parameters along and perpendicular to the c-axis, respectively. (e) XRD scan shows the (0006) planes of V_2O_3 and c-cut sapphire (ICDD card no. 04-002-9108). (f) Rocking curve scan gives a single peak for V_2O_3 (0006) showing that the c-axis of the corundum V_2O_3 is parallel to the substrate surface.

It is known that at room temperature, V_2O_3 is in the paramagnetic metallic (PM) corundum phase, whereas around 160 K, it turns into the antiferromagnetic insulating (AFI) monoclinic phase via a first-order phase transition[59][103]. Moreover, tensile stress stabilizes the paramagnetic-insulating (PI) corundum phase at room temperature or above[96]. PI and PM phase equilibria end with the solid-state critical point to enter a solid-state supercritical state (analogous to supercritical fluids), when the crystal is under tensile stress at elevated temperatures (around 400 K). The stress-temperature phase modulation regulates the phase stability diagram of V_2O_3[104] given in figure 4.7. The effect of doping and stress is illustrated on the lateral axis, and the effect of the temperature is illustrated on the vertical axis. The shaded region above 400 K, beyond the critical point, depicts the supercritical state where Mott criticality is prevalent.

Raman spectroscopy is a powerful tool to differentiate PI and PM phases although few studies reported the Raman response of V_2O_3 due the missing of a suitable crystalline V_2O_3 platform to compare PI and PM phases' Raman information. Attempts to explore the phase diagram is mostly limited to chromium or titanium-doped samples as PI to PM transition can be obtained without tensile straining the V_2O_3 thin films[83][104]. When V_2O_3 is doped by a certain amount of Cr or Ti, the PI or PM phases respectively become stable in unstrained films. However, this simple-minded approach leads to poor phase purity due to coexistence of the metallic and insulating domains stabilized by structural defects[105]. Bulk V_2O_3 samples suffer from impracticable phase engineering via stress modulation. Therefore, using high-quality single crystalline V_2O_3 crystals can screen the above-mentioned challenges for reliable Raman investigations on different phases.

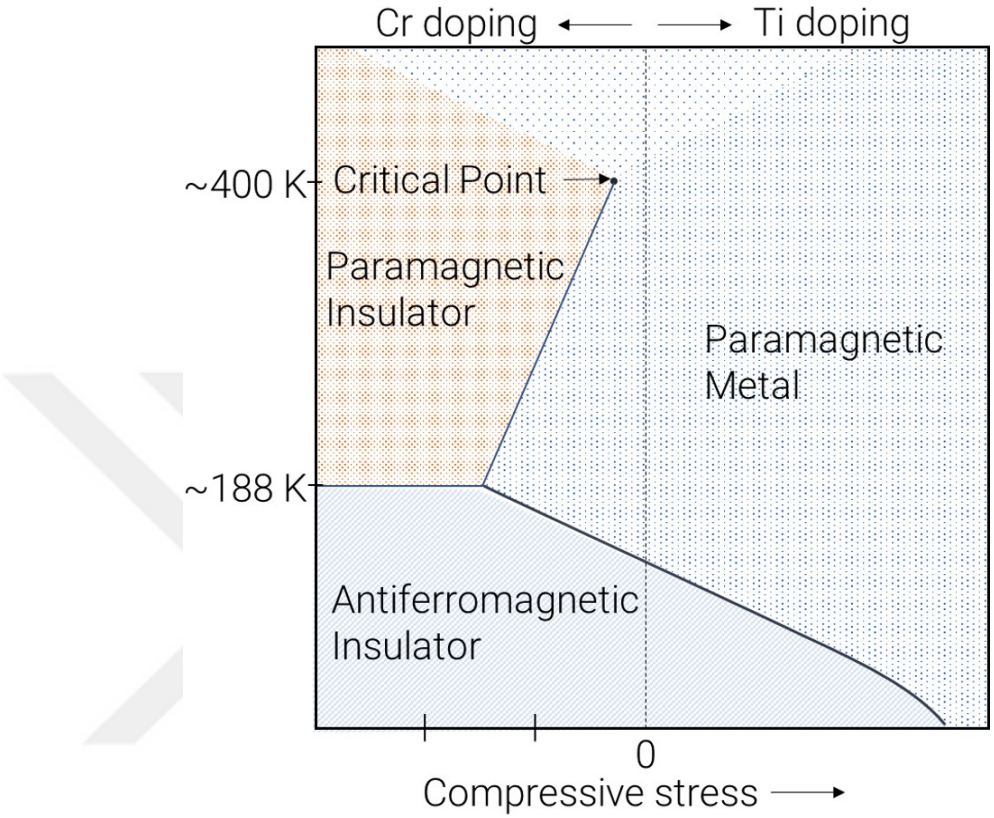

Figure 4.7: Tentative phase stability diagram of V_2O_3 is depicted in the figure based on the previous reports. Marked temperatures on the graph designate the temperature of the critical point and the triple point. Markings on the horizontal axis indicate 4-kbars/division hydrostatic pressure[90].

Table 4.1: Comparison of the Raman peak positions for as-grown and transferred V_2O_3 crystals with the literature.

	This work (as-grown crystals PI phase)	$(V_{0.985}Cr_{0.015})_2O_3$* (PI phase)[106]	$(V_{0.985}Cr_{0.015})_2O_3$ (PI phase)[106]	This work (Transferred crystals PM phase)	Pure V_2O_3* (PM phase)[106]	Pure V_2O_3 (PM phase)[107]
	Raman Shift (cm^{-1})			Raman Shift (cm^{-1})		
E_g	-	200	210	210	210	203
A_{1g}	-	230	234	237	235	231
E_g	248	246	246	293	291	290
E_g	305	310	327	327	320	-
A_{1g}	514	514	501	502	500	500
E_g	590	590	595	590	590	590

*Values extracted from graph

Raman spectrum of paramagnetic (PM) V_2O_3 has been reported to have six well-defined peaks corresponding to E_g and A_{1g} vibrational modes at 203, 290, 590, 231, and 500 cm^{-1}, respectively[107][106]. Raman spectra for our as-grown crystals on sapphire have peaks around 248, 305, 514, and 590 cm^{-1}, and they match well with the spectrum of the paramagnetic-insulating phase reported by Tatsuyama and Fan for $(V_{0.985}Cr_{0.015})_2O_3$[106]. A detailed comparison of our measurements with the literature is given in Table 4.1.

The PI phase Raman conforms with the as-grown V_2O_3 crystals. According to the phase diagram (figure 4.7), the as-grown crystals are under tensile stress. Taking into account the thermal expansion coefficient (TEC) difference between sapphire and V_2O_3 crystals, while cooling down to the room temperature, they meet a tensile stress[108]. TEC parallel to the c-cut sapphire surface ($\alpha_S^{||}$) ranges from 8.5 to 5.3×10^{-6} K^{-1} within 850 to 25 °C. V_2O_3 has a negative TEC value for 25 to 400 °C and positive above 400 °C along the corundum c-axis ($\alpha_{V_2O_3}^{||}$=-1.273+1.782·10^{-8}T+2.405·$10^{-13}$$T^2$ $°C^{-1}$) and positive for the a-axis ($\alpha_{V_2O_3}^{\perp}$=3.266·10^{-5}T-2.871·10^{-8}T+7.747·$10^{-13}$$T^2$ $°C^{-1}$)[108]. In plane strain due to thermal expansion coefficient difference will be isotropic. Length change upon cooling from the growth temperature to the room temperature is Δ_S=5.5·10^{-3}L for the sapphire surface and $\Delta_{V_2O_3}$=16.7·10^{-3}L for V_2O_3. Such a difference introduces ≈1.1% in-plane strain on the crystals. Taking account of isotropic Poisson's ratio (ν=0.33)[109] for V_2O_3, total hydro-static volumetric expansion, $\frac{\Delta V}{V}=(1+\frac{\Delta L}{L})^{1-\nu}$-1, would be 0.29%. Isothermal bulk modulus is given by K_r=-$V\frac{dP}{dV}$=1.75 Mbar for V_2O_3 following Sato et. al[110]. Accordingly, we can calculate the equivalent hydro static pressure as -6.6 kbar. According to the phase stability diagram, such a negative hydro-static pressure is large enough to stabilize the PI phase at room temperature[103]. This shows the equivalence of the in-plane strain to the hydro-static pressure. The mismatch between TECs also implies that the growth temperature has an influence on the strain at room temperature. The V_2O_3 growth temperature might vary from 700 to 850 °C. Therefore, the range of hydro-static pressure experienced by the crystals due to TEC differences varies from -6.6 to -5.9 kbar. Yet, the upper limit is sufficient to maintain the crystals in the PI phase. These analyses are consistent with the

fact that the as-synthesized crystals are in the paramagnetic-insulating phase. As indicated in figure 4.8, all the as-grown crystals ranging from 100 to 10 nm in thickness, show the PI Raman fingerprint. No variations observed in the Raman features except thickness dependent intensities. This points out that the crystals are stoichiometrically similar.

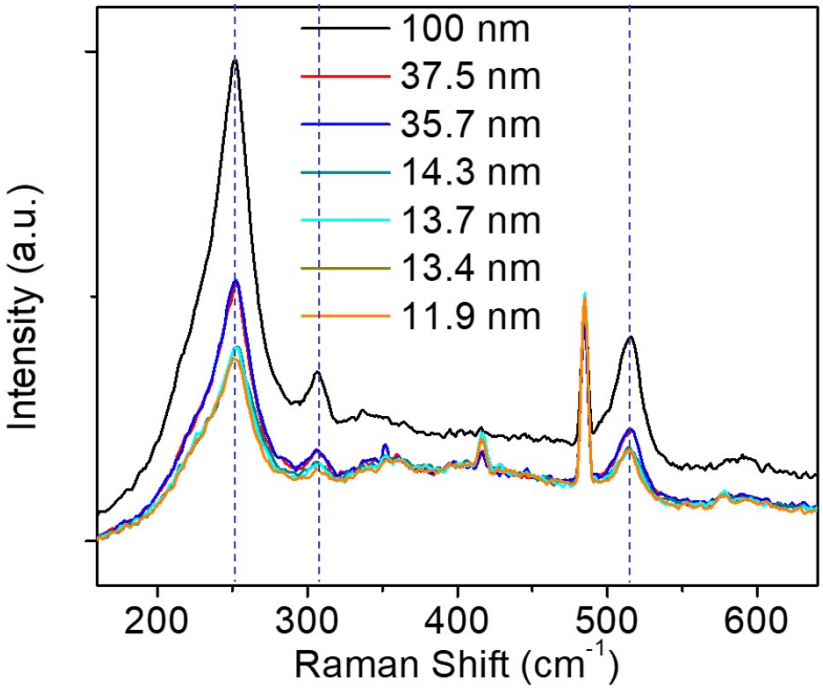

Figure 4.8: Stack of Raman scatterings taken from the as-grown V_2O_3 crystals with different thicknesses. The major peaks are labeled with the dashed lines. The remaining peaks are from the sapphire substrate.

A striking change occurs in the Raman spectrum after releasing crystals from the sapphire surface or when they are agitated strongly on the sapphire surface. As a comparison, Raman scatterings of an as-grown and a transferred onto a clean sapphire substrate are shown in figure 4.9 (a). The Raman peak positions of the transferred crystals agree well with the reported PM phase[107][106]. This change in the spectrum can be explained by the phase transition from the PI to the PM phase due to the relaxation of the tensile stress on the crystals.

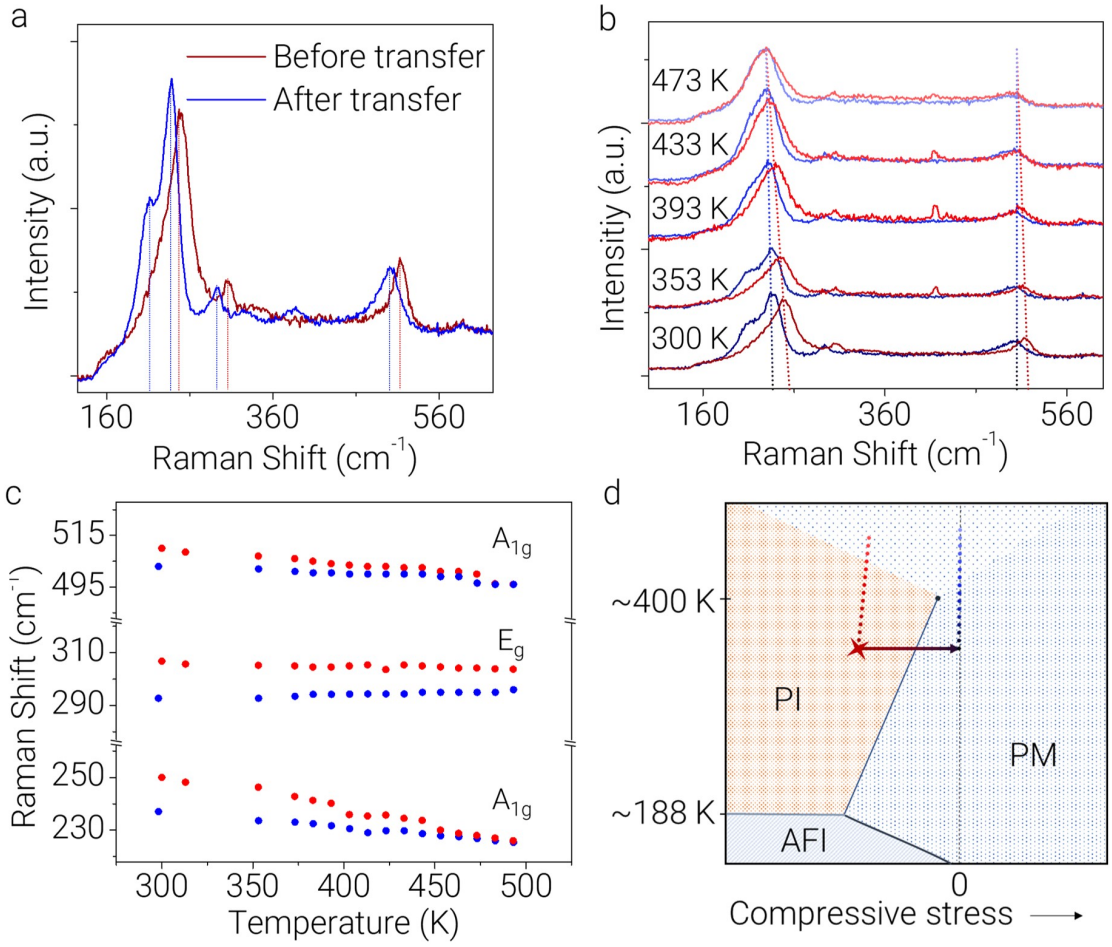

Figure 4.9: Temperature dependent Raman analysis of the as-grown and the transferred V_2O_3 crystals[90]. (a) Raman spectra of as-grown and transferred V_2O_3 on sapphire are given in the figure. Major Raman modes reported in the literature are marked by dashed lines with respective colors. (b) Raman spectra of as-grown (red series) and transferred (blue series) crystals become similar upon heating. The E_g mode around 210 cm^{-1} gradually disappears with the increasing temperature, and the A_{1g} mode softens in both cases to merge around 450 K. The peak around 416 cm^{-1} is coming from the sapphire substrate. (c) Temperature dependences of the peak Raman modes for the as-grown (red points) and the transferred (blue points) crystals. Raman peak positions can be determined with ± 5 cm^{-1} precision. (d) Effects of releasing the crystals and heating both as-grown and transferred crystals are illustrated on the tentative phase stability diagram. The red star marks the tentative stress on the as-grown nanoplate at room temperature, and the solid arrow emerging from it indicates the effect of transferring. The red and blue dotted lines depict how both as-grown and transferred crystals, respectively, enter the supercritical state. The red dotted line is drawn slanted as the temperature increase will reduce the tensile stress due to differences in thermal expansions of V_2O_3 and the substrate.

Temperature dependent Raman spectra of both as-grown and transferred V_2O_3 crystals, shown in figure 4.9 (b), specify a reversible softening of the Raman modes, especially above 400 K. Intriguingly, both phases show a similar feature above 400 K. The initial spectra of both phases is retrieved by cooling back to the room temperature. This observation can be attributed to the emergence of the supercritical state upon heating. The PI and PM phase boundaries end in a second-order critical point[83]. Consequently, crystals heated into the supercritical state display a unique Raman spectra irrespective of their initial phase.

Figure 4.9 (c) shows the temperature dependence of Raman peaks persisting up to the supercritical state for both PI and PM crystals, in which the A_{1g} peaks merge at the elevated temperatures whereas the E_g peaks undergo little variations with the temperature. This can be explained by insensitivity of in-plane E_g modes to the second-order phase transition due to the fact that the $e_g(\pi)$ band is perpendicular to the c axis[111] and the vibration of atoms along the c axis mainly affects the A_{1g} modes[106]. In the tentative phase stability diagram (figure 4.9 (d)), it is shown how the different initial phases terminate in the similar Raman responses. It is further supported by the asymmetric peak at 514 cm^{-1} at the super critical state. Such an asymmetry can be attributed to the Fano resonances of the Raman active electronic transitions across α_{1g} and e_g bands near the Fermi level[112]. As the number of electrons in the α_{1g} band increases in the supercritical state compared to the PI phase, the continuum electronic Raman process (belonging to the same symmetry group) may interact with each other. Such an interaction between a discrete process with a continuum process results in an asymmetry in the Raman peak.

The crystal structure and crystallinity of the V_2O_3 nanoplates (transferred to holey carbon and silicon nitrite grids) are characterized using TEM and SAED (figure 4.10 (a-d). In addition, cross section of the V_2O_3 on sapphire is analyzed via HR-TEM and SAED (figure 4.10 (e-f)). Looking through the [111] zone axis perpendicular to the sample surface, a sixfold symmetric arrangement is realized with d spacing of 2.5 Å corresponding the $(10\bar{1}0)$ plane. This is consistent with the XRD measurements as the corundum c axis points perpendicular to the nanoplate surface. However, such a pattern can be attributed to fcc or bcc structures as well and more diffraction patterns at other zones must be solved for the clarification. Surprisingly, the SAED patterns taken along different zone axes match exactly with a face-centered-cubic (fcc) structure rather than more commonly reported hexagonal-closed-packed (hcp) corundum structure. In order to slip away from the measurement errors, five separate crystals that transferred via different methods are measured at the indicated zone axes. This helps us to reliably solve the diffraction patterns likewise solving a two-variable problem with three equations. Although hcp structure is expected according to the XRD results, figure 4.10 (c) and (d) are perfectly consistent with the fcc structure, thus contrary to the XRD results.

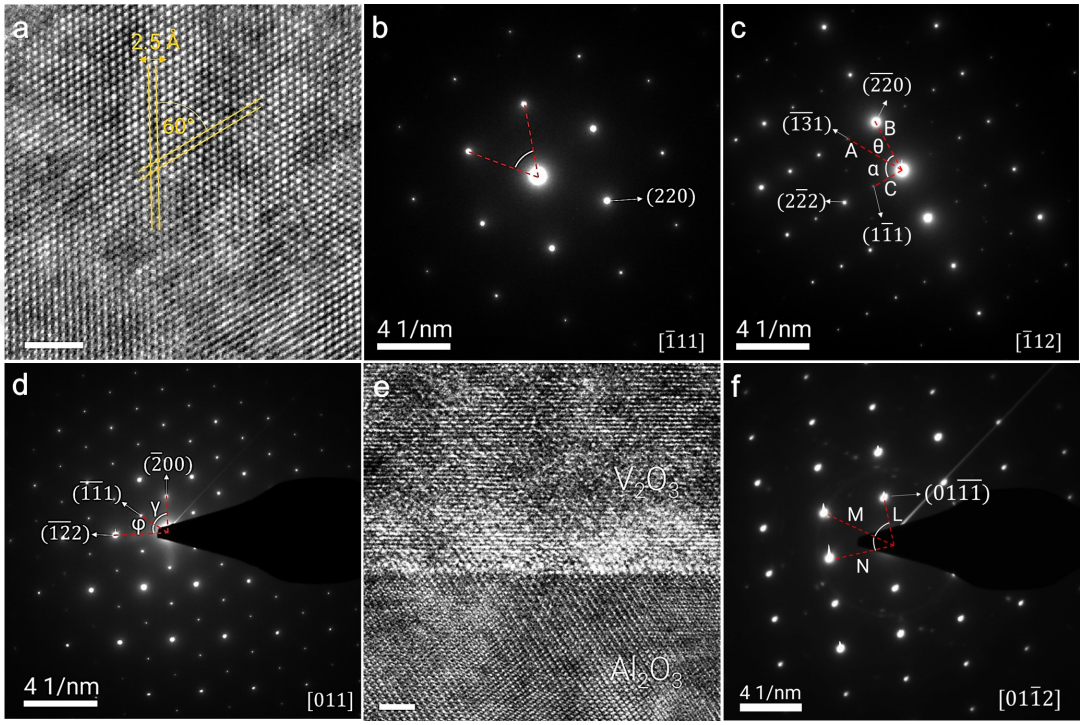

Figure 4.10: TEM analyses of V_2O_3 crystals[90]. (a) HR-TEM image of a V_2O_3 crystal. The close-packed structure is evident. The scale bar is 2 nm. (b) Sixfold symmetric SAED pattern indexed according to the fcc [$\bar{1}$11] direction. However, the same pattern is produced for the hcp [0001] direction. The lengths of the red dashed lines are 4nm^{-1}, corresponding to 2.5 Å d-spacing along (220) fcc or (10$\bar{1}$0) hcp planes. (c) Once the sample is tilted to a different zone axis, the difference between the fcc and the hcp structures becomes clear. No such pattern can be found for hcp. The angles between the principal plane normals θ=39.23°, α=50.77°, and the ratios of the principal spot spacings B/C=1.633, A/C=1.915 match exactly with the standard indexed diffraction pattern for fcc crystals. (d) Another specific fcc diffraction pattern is obtained and indexed along the [011] direction. The angles between the principal plane normals γ=54.74° and ϕ=35.26° match perfectly with the standard indexed diffraction pattern for fcc crystals. (e) The cross-sectional HR-TEM image shows the stacking of a V_2O_3 crystal on the Al_2O_3 substrate. The scale bar is 2 nm. (f) SAED pattern taken from the V_2O_3 sample prepared for the cross-sectional TEM imaging can be uniquely indexed with the hcp [01$\bar{1}$2] diffraction pattern. Both angles between the principal plane normals and N/L=1.52 and M/L=1.82 match very well with the standard indexed SAED for hcp.

The observed shift in stacking from hcp to fcc can be explained by a slight structural change upon heating of the crystals by the electron beam up to the supercritical state. This claim is further supported by Raman measurements on free standing crystals over TEM grids. According to the phase stability diagram, a temperature rise of ≈150 K is sufficient for emergence of the supercritical state in the nanoplates. Demonstrated by Guo et al[113], electron-beam heating in TEM samples is measured using the MIT temperature in VO_2 nanocrystals, and even with very modest electron flux, it is possible to induce a significant temperature rise in the cantilevered nanocrystals. Another evidence supporting the electron-beam-induced heating which triggers the structural change is comprehended from the SAED pattern taken from the cross-sectional TEM sample (figure 4.10 (f)). In this sample, as shown in figure 4.10 (e), the V_2O_3 crystals is sandwiched between the sapphire substrate and the platinum top layer, thus not thermally isolated. The SAED pattern taken from the cross-sectional sample matches very well with the hcp corundum structure as opposite to the patterns taken from the free-standing crystals. This suggests that the beam-induced heating in this case is not high enough to cause the hcp to fcc transition over the supercritical state. Another instinctive back up derive from the Raman measurements on free standing V_2O_3 crystals over TEM grids (figure 4.11 (a-b)). As the tensile stress is released upon transferring into the grids, the PM phase Raman scattering is grasped (figure 4.11 (b) 20 μW laser power). We notice that crystals suspended on holey carbon grids are exceptionally sensitive to the laser power. This is not too surprising as there is no supporting substrate, thus the absorbed laser power results in a greater local temperature increase in the crystal. Raman spectra taken with ≈20, 40 and 80 μW laser powers are given in figure 4.11 (b). Applied 20 μW laser power, PM phase is evident, though illuminated with 40 or 80 μW, A_{1g} peak around 240 cm^{-1} shifts towards 230 cm^{-1}. Such a Raman change has been already discussed in figure 4.9 (b), indicating the local temperature rise up to the supercritical state. Comparing the peak position to figure 4.9 (b), we conclude that the temperature rise in the nanoplate is around 4 K/μW. To verify the clarity of the transferred crystals, Energy dispersive X-ray spectroscopy taken in TEM samples confirms that O and V are the dominant elements (figure 4.11 (d)).

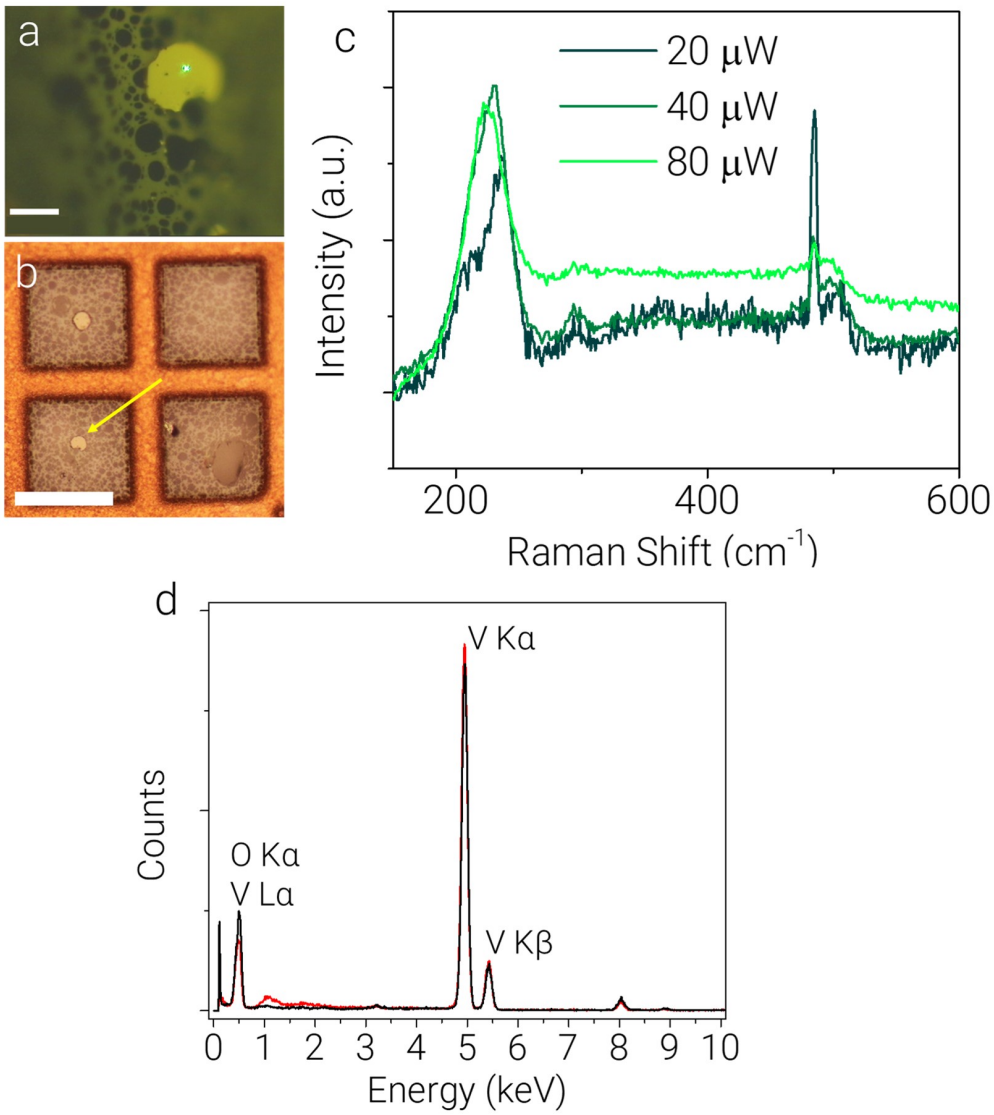

Figure 4.11: Raman and EDS analyses of the TEM samples[90]. (a) Optical microscope micrograph of a V_2O_3 crystal transferred on holey carbon TEM grid. The scale bar is 10 μm. (b) Smaller magnification optical image of the same crystal in a (marked with a yellow arrow). The scale bar is 50 μm. (c) Raman spectra taken at various laser powers. 20 and 40 μW spectra are scaled accordingly to show the features. Laser heating is apparent as the metallic V_2O_3 enters to the supercritical state with increasing the laser power. (d) EDS spectrum taken in TEM for two different samples shows O and V are the dominant elements. Traces of Cu is is due to the TEM grid.

I would like to note that there are no previous reports of a fcc structure for the high-temperature V_2O_3 along with the supercritical state information, and further studies are required to elaborate this intriguing observation.

4.3.4 Electrical properties of V_2O_3 devices

Four-terminal configuration devices are used to investigate the electrical properties of both as-grown and transferred V_2O_3 crystals corresponding to the PI and PM phases, respectively. As demonstrated by the XPS results (figure 4.5 (a)), a slight native VO_2 forms on the surface when the samples exposed to air for longer than a day. Such surface oxidation can significantly affect the PM phase devices, dominating the insulator behavior rather than the metallic due to the poor electrical contact to the V_2O_3. Accordingly, prior to the metal contact deposition on to the patterned crystals, the buffered oxide etchant (BOE) (6:1 volume ratio of 40% NH_4F:49% HF in water) is used to remove the oxide formation from the surface. To realize the suitable etch time, we perform AFM measurements within various etch times and track the height changes over the crystals. Figure 4.12 shows the AFM results of a crystal before and after BOE etching. After 5 seconds of BOE treatment, the crystal is thinned down by $\approx$7 nm. Further BOE treatment does not reduce the crystal thickness but the roughness becomes more severe after 5 seconds of the treatment. Therefore, 5 seconds BOE etching is chosen to treat the patterned crystals, immediately followed by the metal contact evaporation.

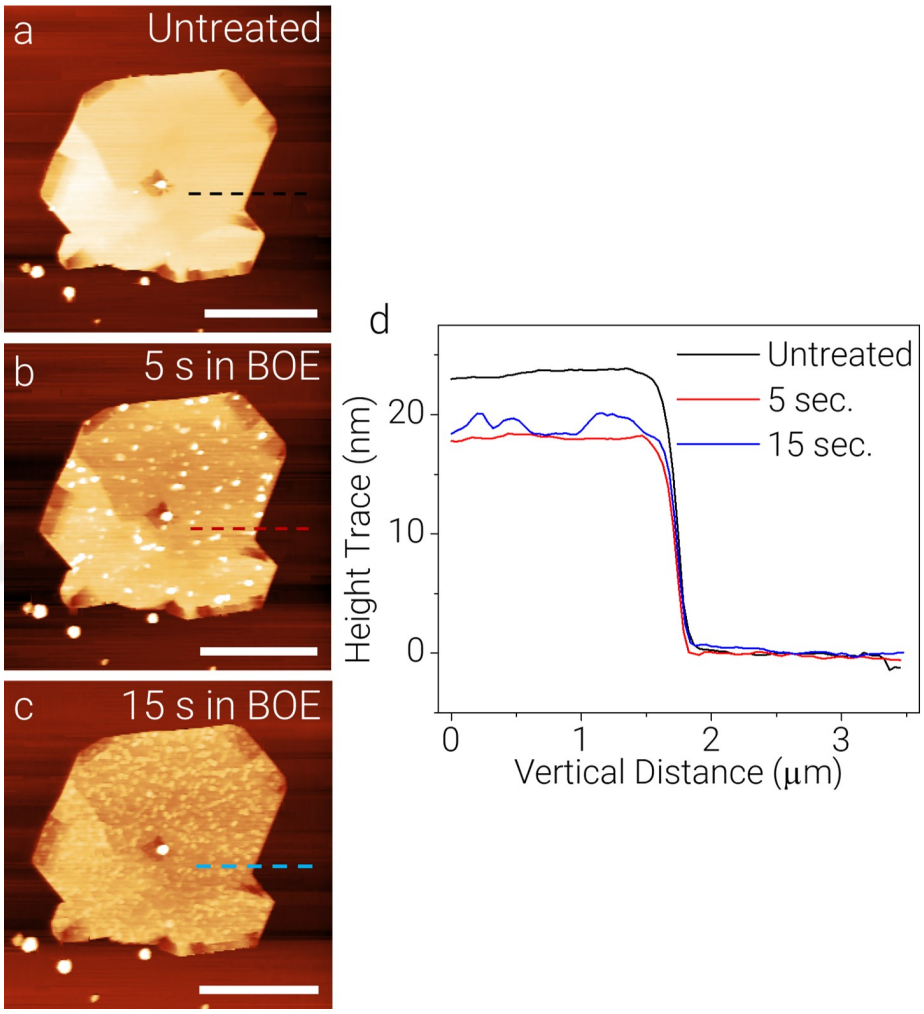

Figure 4.12: Removal of surface oxide for device fabrication[90]. (a) AFM height trace map of a crystal after several days of exposure to the ambient. (b) same crystal after a 5 second BOE treatment. Surface of the crystal becomes noticeably rougher after the BOE treatment. (c) After 15 seconds of BOE treatment no further reduction in the crystal thickness is observed; however, the crystal surface becomes very rough. The scale bars are 4 μm. (d) Height traces taken through the colored dashed lines in respective AFM maps, indicating the change in the crystal thickness.

Resistance vs temperature (RT) curve taken on as-grown crystals using a four-terminal configuration (source current from the outer terminals and measure the voltage drop from the inner ones) within 150 to 300 K is shown in figure 4.13 (a). An activated electrical conduction observed throughout the entire temperature regime, accompanied with a rapid increase in the resistivity around 188 K. This is consistent with the fact that our as-grown crystals are in the PI phase, and as they cool down, PI to AFI transition takes place at the previously reported transition temperature[103]. Due to the surface adhesion, the as-grown crystals are under nonuniform stress leading to a shallow phase transition which maintains coexistence of PI and AFI phases over a wide temperature. The results are shown for three devices, all of which manifest insulator-to -insulator transition around 188 K. Resistivity $[\rho(T)]$ vs temperature (T) curve below 188 K (except the vicinity of the phase-transition temperature) can be fitted with an Arrhenius relation $\rho(T) = \rho_0 e^{E_A/k_B T}$, where $E_A = 0.195 \pm 0.005$ eV is the activation energy, k_B is the Boltzmann's constant, and ρ_0 is a constant[81]. Upon transition from PM to AFI phase, the lattice parameters along and perpendicular to the c-axis (shown in figure 4.6 (d)) undergo some expansions. More specifically, a expands by ≈1.9 percent while b expands by ≈4.2 percent. A similar expansion takes place in transition from PM to PI phase.

As discussed in section 4.3.3, through transferring the as-grown V_2O_3 nanoplates to an arbitrary substrate like oxidized Si chip, the tensile stress on the nanoplate is released, and the they turn into the PM phase. The metallic resistivity behavior sustains down to ≈160 K (figure 4.13 (b)). The MIT is observed around 160 K (corresponding to the PM to AFI transition) is much sharper than the PI to AFI transition, yet not abrupt in our devices since the nanoplate still adheres to the SiO_2 surface. Moreover, due to the clamping effect of the electrical contacts, some force is exerted on the nanoplate upon the onset of phase transition since the in-plane lattice constant increases significantly during the MIT. This manifests itself as the staircase-like changes shown in the inset of figure 4.13 (b), attributed to the coexistence of the metallic and the insulating phases over a temperature range[114]. Taking into account the thickness of crystals in the devices, the temperature-dependent resistivity $[\rho(T)]$ of the metallic phase is

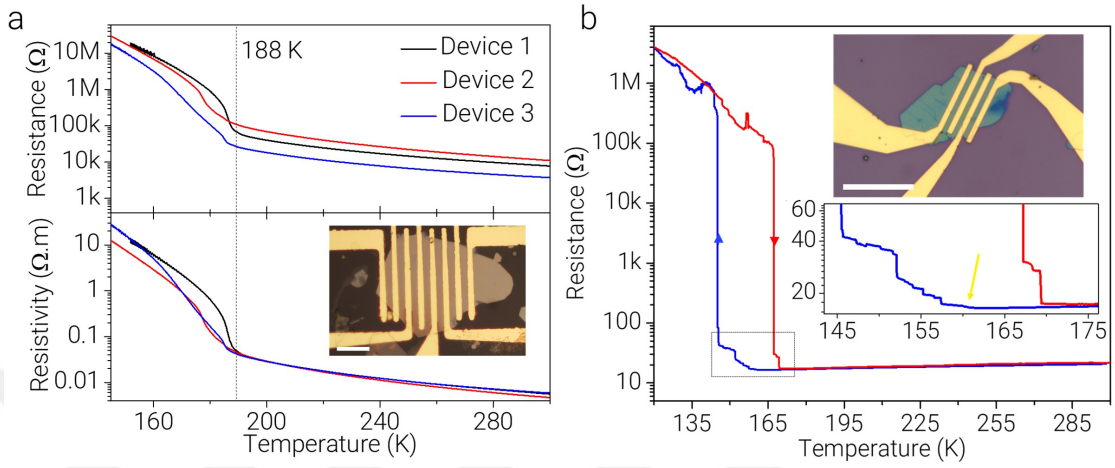

Figure 4.13: Low-temperature electrical measurement of V_2O_3 devices[90]. (a) Resistance and resistivity vs temperature curves for three different devices are given in the graph. The inset in the lower panel shows a typical as-grown nanoplate patterned using optical lithography. The scale bar is 20 μm. (b) Resistance vs temperature curve for a transferred V_2O_3 crystal. For this particular sample, there is a $5\frac{1}{2}$ orders of magnitude change in the resistivity. Here, blue and red colors represent cooling and heating, respectively. The lower inset shows a scale up of the region marked with a dashed rectangle. The onset of the phase transition is around 160 K. The upper inset shows a typical device patterned using electron-beam lithography.

calculated as $\rho(T)/\rho(273K)= 0.58 + 1.5{\cdot}10^{-3}T$, which is comparable to the bulk samples[115][116].

All the features observed in the RT curve can be explained qualitatively based on the tentative phase diagram. Each device displays a unique RT curve that can be explained by referring to the phase stability diagram. As another example, figure 4.14 (a) shows Two consecutive RT cycles for a device patterned on a transferred V_2O_3 nanoplate, thus in the PM phase at room temperature. The assumption that the crystal is relaxed might not be precisely correct but it does not affect the qualitative analysis drawn in figure 4.14 (b). Any residual stress along the crystal would affect the onset the MIT temperature. While cooling the device, likewise the device shown in figure 4.13 (b), the onset of transition is observed around 160 K. The staircase like transitions appear again, indicating the coexistence of both phases, which can be attributed to two reasons. First, electrical contacts clamp the nanoplate down and restrict the expansion of the

crystal upon MIT and second, the nanoplate adheres to the SiO_2 surface, resulting a slip-stick expansion of the crystal. Once the AFI phase promotes over the whole section, the same activated behavior in resistivity is spotted. At this point, the pressure applied by the crystal is great enough to push the contacts to reduce the strain, thus crystal return to the strain-free state. Upon heating the device, it superheats up to 170 K. Interestingly, the activated conduction is no longer present and coexistence continues up to 192 K which is greater than the presumed temperature for the triple point. Thus, some tensile strain on the crystal might be relaxed by the introduction of the PI phase. As the PI phase has in-plane lattice constant in between AFI and PM phases, this proposition is not too invalid. Finally, the resistance returns to its original value abruptly at around 192 K.

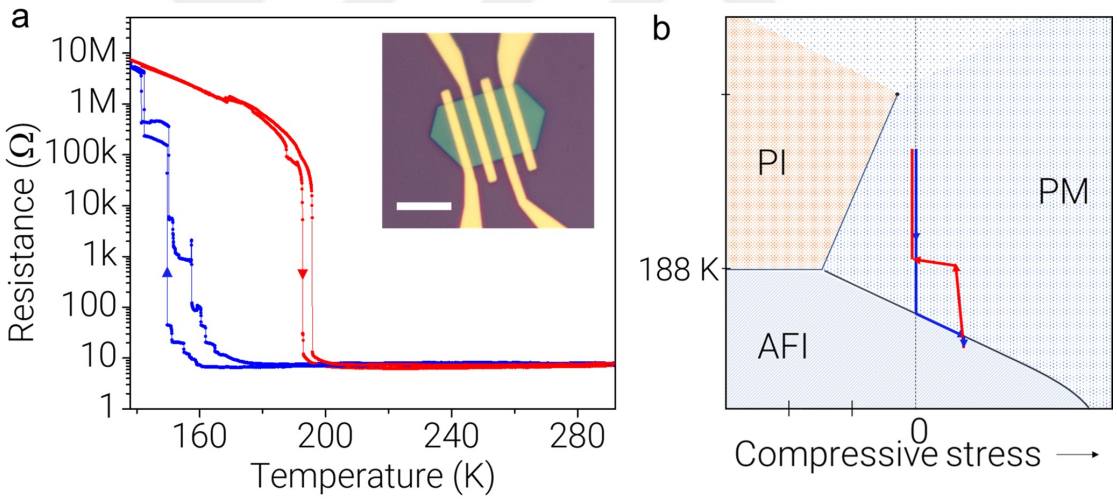

Figure 4.14: Synchronized RT curve with the phase stability diagram[90]. (a) Two RT cycles for a device patterned on a transferred V_2O_3 nanoplate. Blue and red colors indicate cooling and heating, respectively. The scale bar in the inset image is 10 μm. (b) Tentative phase diagram with the colored arrows depicting the changes crystal experiences upon thermal cycling.

Chapter 5

Synthesis, electric-field induced phase transitions and memristive properties of spontaneously ion intercalated two-dimensional MnO_2

As discussed in chapter 4, the RTO-CVD chamber is a robust platform to develop synthesis recipe for unknown materials. In this chapter, for the first time, chemical vapor deposition (CVD) synthesis of large-area single-crystalline layered 2D MnO_2 nanosheets is succeeded, spontaneously intercalated by potassium ions during the synthesis. Further detailed studies verify that the charge transport in these crystals is dominated by the motion of hydrated potassium ions in the interlayer space. Such an in-plane ionic conductivity has been realized for the first time in 2D community. Contingent on the electrical and optical modulation of the potassium and the interlayer water concentration, a reversible layered-to-spinel phase transition accompanied by an optical contrast change is appreciated in 2D K-MnO_2 crystals. The phase transition causes variations in the ionic content along with the motion of K ions, dictating the memristive switching mechanism.

Finally, as a prospective application, emulation of synaptic behaviors is comprehended using the electric field driven ionic motion in two-terminal graphite contact K-MnO_2 devices.

5.1 Introduction

The term "Memristor" refers to a non-linear two-terminal electrical component whose resistance depends on the magnitude and polarity of the applied voltage; thus, remembers its most recent resistance history based on the voltage input. The concept was theoretically predicted in 1971 by Leon Chua[117] followed by the experimental demonstration in 2008 by R.Stanley Williams et al[118], finding the fourth fundamental circuit element, joining the resistor, capacitor and inductor. Typically, memristors have been realized in three-dimensional (3D) material systems with an oxide layer sandwiched between metal contacts[119], until 2015 that Mark C.Hersam et al[120] developed the first 2D memristor via defect engineering in a defective monolayer MoS_2. This breakthrough enables a new functionality to the device by a third gate terminal in a field-effect geometry. Since then, many efforts have been put forward to scale down memristors to an atomic-layer level, producing rich physical and chemical properties as exemplified in various 2D crystals[121] but not the traditional memristors, such as robust mechanical strength and flexibility[122], superb chemical stability[123], enhanced thermal heat dissipation[124] and ultra-low power consumption[125].

Realizing memristive behavior in the emerging 2D materials will add up new applications to this group of captivating materials. Combined with transistors in a hybrid chip, memristors could radically improve the performance of digital circuits without requiring the costly and increasingly difficult doublings of transistor density on chips[126], granting us another decade, at least, of Moore's Law performance improvement. However, developing a reliable 2D memristor often requires fabrication of complex stack of materials and elaborated engineering. Besides defect engineering[120][127][128], phase transition[129][130][131], heterostructure and interfaces[132][133][134][135][136] as well as surface oxidation[137][138][139]

have been engineered to develop a 2D non-volatile resistive switching device. Furthermore, it has been shown that reversible modulations through electric field-controlled Li^+ and Ag^+ ion migration in 2D MoS_2[130] and $GeSe_2$[140], respectively, lead to the memristor behavior. In both cases, the ions are extrinsically inserted to the structure via Lithium intercalation or using Silver as one of the electrodes, and the intrinsic ionic engineering in a 2D material has not been succeeded yet.

Ion intercalation engineering of 2D materials[141][142] may open up a new world to enabling novel technologies in energy storage[143][144], electronics[145][146], optoelectronics[147][148][149][150][151], neuromorphic computing[130] and, magnetic information storage and processing[152]. 2D layered materials are suitable hosts to be externally intercalated by the guest ions due to the weak van der waals interaction among the layers. However, extrinsic ion intercalation through the edges of 2D crystals causes wrinkling and distortion of the crystal without securing any spatial uniformity or scalability. Despite the recent efforts putting forward on ion intercalation through the top surface[142], device fabrication still suffers from the scalable integration of ion intercalation engineering for technological applications. One fundamental solution to untangle these challenges is coming across with a 2D material owning intrinsic in-plane ionic conductivity along the basal plane. Nevertheless, no such a material has been reported in 2D form, yet.

Manganese dioxide (MnO_2) is capable of hosting a variety of cations, which has been studied for various applications in catalysis[153], supercapacitor and battery applications[154][155], water extraction and splitting[156], and others[157] as it is a low-cost environmentally friendly alternative. Layered manganese oxide compounds commonly known as birnessite whose structure comprised of edge-sharing MnO_2 octahedra, with water molecules and/or metal cations occupying the interlayer region[158] as shown in figure 5.1. It is well-known as an electrochemical active catalysis and gained considerable attention as cathode materials for aqueous rechargeable batteries[159][160] as well as supercapacitors for energy storage[158][161]. One of the challenges in promoting electrochemical properties of the birnessite is its low conductivity arising from poor

crystallinity[162]. Typically, low temperature methods such as sol-gel[163][164] and hydrothermal[161][165] are used to synthesize birnessite compounds, forming low crystalline morphologies. One way around this is developing high temperature synthesis methods in a scalable fashion. When synthesized via hydrothermal methods[166][167][168], MnO_2 exhibits diverse polymorphism which can be classified as layered (2D) or tunnel (1D) MnO_2 according to the specific framework formed by the edge- and corner-sharing MnO_6 octahedra (figure 5.1). The guest cations such as Li^+, Na^+, K^+, etc. stabilize both 1D and 2D structures along with the structural water[169][170]. Meanwhile, 2D to 1D transition takes place via of movement of Mn atoms from intralayer space to the interlayer positions[171]. In addition, electrochemically induced phase transitions across MnO_2 and Mn_3O_4 have been reported[172][173][174][175]. Representative crystal structure schematics of the MnO_2 polymorph classes and spinel-Mn_3O_4 are depicted in figure 5.1. Although the birnessite MnO_2 embraces a layered structure, no large-area 2D nanosheets have been succeeded based on that. Hydrothermally obtained K-MnO_2 has been shown to be delaminated into atomically thin flakes[176][177][178]; however, the lateral crystal sizes attained via liquid or mechanical exfoliation methods are far too small for practical single crystal device applications along with their poor crystalline quality.

5.2 Experimental method

5.2.1 Synthesis of 2D K-MnO_2 crystals

Real-time optical observation chemical vapor deposition (RTO-CVD) chamber is used for the crystal growth. RTO-CVD method is very practical in developing new growth recipes as it allows real time observation and control of the crystal formation. The synthesis of K-MnO_2 is obtained via melting of the MnO_2 precursor mixed with the potassium iodide salt on c-cut sapphire substrate for an epitaxial growth. The sapphire substrate is rinsed with acetone, IPA and water then dried before using. The KI and MnO_2 powders are milled together in a fine

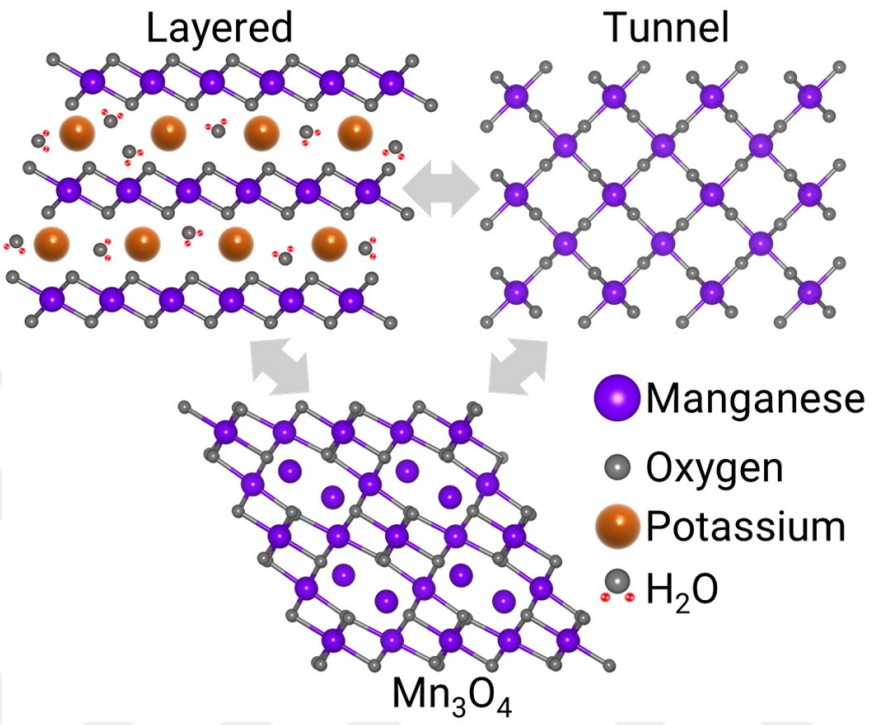

Figure 5.1: Representative schematics of layered and tunnel polymorphs of MnO_2 and, Mn_3O_4. Phase transition among various polymorphs is possible. Mn^{2+} ions in Mn_3O_4 schematic are depicted without bonds for clarity.

powder in 5:1 ratio, then a few granules placed on the growth substrate. The chamber lid is closed, and the substrate heater is ramped to 640 °C at a rate of 30 °C/min under ambient conditions. The growth takes place around 640 °C for 5 minutes while the the crystals of desired size are observed optically. Finally, the substrate heater is turned off and naturally cooled down to the room temperature within 10 minutes. The remaining precursors are removed via ultra-sonication of the growth substrate in acetone and blowing high purity nitrogen. Series of optical images taken at 640 °C with the passage of time are shown in figure 5.2 (a-d) (see supplementary movie 3 for the entire growth video). The same recipe is transferred to conventional tubular CVD chambers and similar high-quality crystals are obtained in KAIST university.

Theoretical structural prediction made by Mendoza-Cortes et al[179] predicts stability of various birnessite types (with different intercalated cations) down to the monolayer form. The mentioned-above growth procedure paves the novel way to converge the theoretical prediction and experimental results. Indeed, the growth strategy can be extended to the other birnessite types (with different cations) and open up the entry to the new class of layered 2D materials.

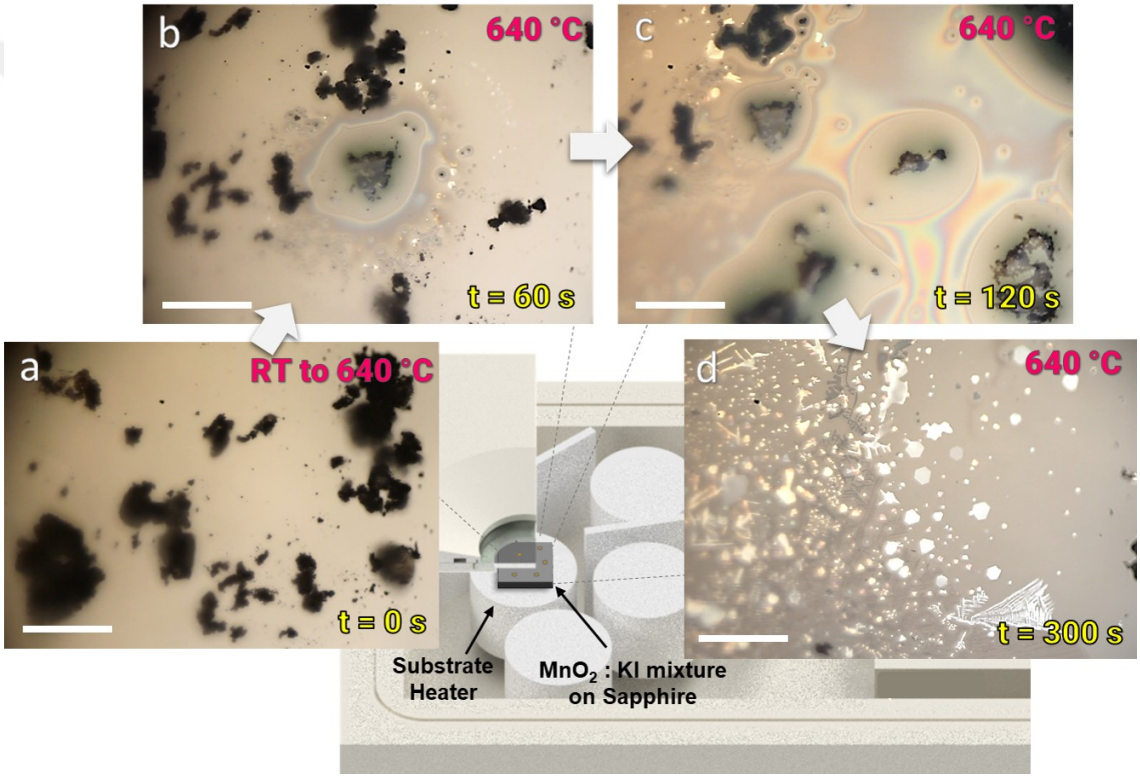

Figure 5.2: A series of optical microscope micrographs taken during the K-MnO_2 CVD synthesis. The beginning of the observation in (a) is marked as time zero after reaching 640 °C. As the time passes by (b) and (c), the more molten phase forms until fully solidification in (d). All the scale bars correspond to 100 μm.

5.2.2 Characterization methodology

Raman spectra are collected with 532 nm Rayleigh excitation at various powers typically less than 0.2 mW. The temperature dependent measurements in ambient and under vacuum are performed in a custom-made chamber with a sapphire optical window. Ambient measurements are performed with the chamber open and the vacuum measurements are taken with a turbomolecular pump backed with a rotary vane roughing pump. 99.999% Ar line is connected to the vacuum side of the turbo pump. All the lines are pumped before starting the experiments. The setup can reach to a base pressure of 6.0×10^{-3} mbar. Temperature reading of the sample is taken from the top of the heating stage with a PT-1000 resistive sensor.

X-ray diffraction measurements are taken on as grown samples using XRD Panalytical MRD X'pert Pro diffractometer equipped with a Cu Kα source. Similarly, XPS analysis is performed on as grown samples using K-Alpha X-ray photoemission spectrometer by Thermo Scientific. TEM samples are prepared by transferring crystals over holey carbon TEM grids. 6% polycarbonate solution in chloroform is spin-coated on the growth substrate at 1500 rpm. Then the substrate is heated to 180 °C for 6 minutes to bake the film. Subsequently, the polycarbonate film is gently peeled of from the surface with the help of water. The film is placed on an empty Si substrate with crystals facing up. Suitable regions are determined under optical microscope and the film is cut to match the size of the TEM grid. Then the cut section is peeled off from the Si surface and placed over the TEM grid. The grid is placed gently into chloroform to dissolve the polycarbonate film to leave the crystals over the grid. TEM measurements are performed using Tecnai G2 F30 S-Twin for collecting HR-TEM and SAED data. Electrostatic Force Microscopy (EFM) measurements are taken via MFP 3D Asylum Research AFM using conductive Pt-Ir cantilevers.

5.2.3 Device fabrication

Gold contacted devices are fabricated using standard optical lithography. AZ5214 resist is spin-coated over the growth substrate. Then, suitable crystals are patterned using UV exposure. Following the developing of the resist, 5 nm Cr and 70 nm Au is evaporated thermally. After the lift-off in acetone, devices are dried with nitrogen. Crystals are not immersed in water or rinsed in any stage of the fabrication.

Graphite electrode devices are fabricated using stamping method followed by indium needle placement. First, thin graphite flakes are mechanically cleaved over Polydimethylsiloxane (PDMS) stamp. Then, the stamp is deterministically placed over the target crystal. Upon contact the substrate is heated to 70 °C for PDMS to release the graphite. The same procedure is repeated for the other Gr contact. Then, a fine needle is drawn from a molten indium blob, using a micromanipulator and a tungsten probe. The needle is placed on the sample heated to 160 °C, slightly above the melting point of the indium. Once the needles are placed over the graphite electrodes, the sample is removed over the stage. The total exposure to high temperature is limited to a few minutes. The pulse measurements are performed using a lab-view programmed Keithley 4200A parameter analyzer. The pulse trains are validated by DSOX3014A Oscilloscope before the measurements.

5.3 Result and discussion

5.3.1 Characterization of 2D K-MnO_2 nanosheets

Figure 5.3 shows optical micrographs of some representative K-MnO_2 crystals on sapphire substrate. The low magnification image (a) indicates the superb efficiency of the growth. The preferred growth orientation of the crystals in (b) suggests the epitaxial relation with the sapphire substrate. A large-area crystal

up to 100 μm is depicted in (c), showing the growth capability for scaling. Various layers with different color contrasts are visible in (d), conveying the layered nature of the crystal formations. The inset in (d) shows an AFM height trace map revealing ≈0.7 nm thick atomic layer of 2D K-MnO_2, corresponding to a monolayer overgrowth at the center of the crystal.

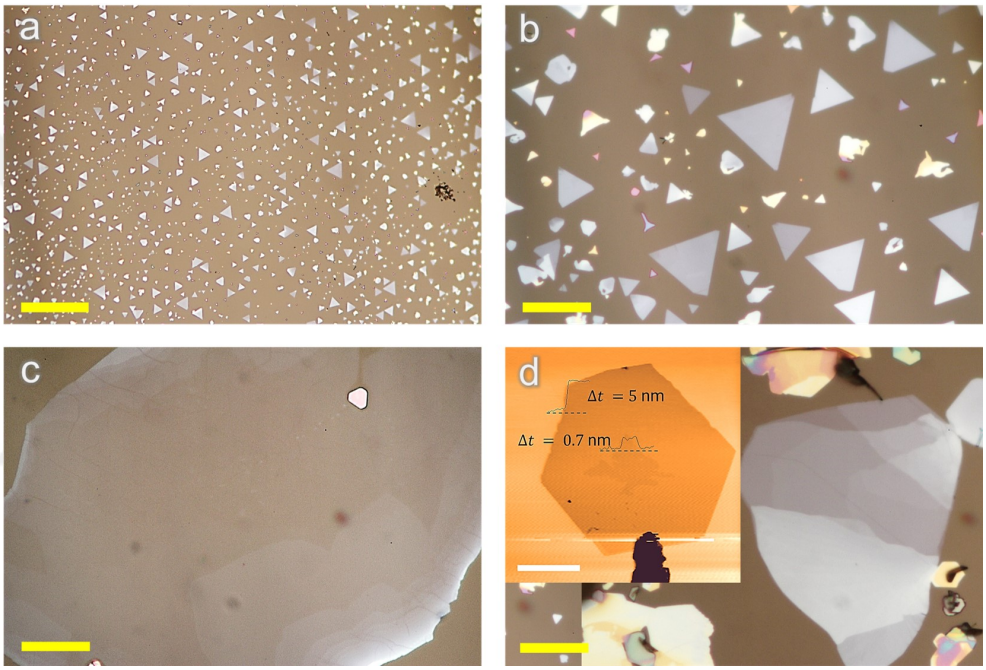

Figure 5.3: Post-growth optical observations of 2D K-MnO_2 crystals. (a) a low-magnified optical image of the growth, showing the high coverage and efficiency. (b) A higher magnified optical image of (a), showing the preferred orientation of the crystals. (c) Optical image of a large-area crystal with the lateral size up to 100 μm. (d) Optical image of an exemplary multi-layer crystal. The darker contrast regions manifest thinner ones. The inset shows an AFM map of a 5 nm thick 2D K-MnO_2 crystal. An overgrowth at the center of the crystal sets out the monolayer thickness of ≈0.7 nm. The scale bar in (a) is 100 μm and 20 μm in (b-d). The scale bar in the inset is 5 μm.

The crystallinity and the crystal structure of 2D nanosheets are studied by X-ray diffraction (XRD). The sharp diffraction peaks scan (figure 5.4 (a)) are located at 12.9° and 25.6° corresponding to (001) and (002) planes of K-MnO_2 in the Birnessite structure, namely δ-MnO_2 (JCPDS card No.80-1098)[180][181][160]. The interlayer spacing calculated from (001) plane is ≈0.69 nm, consistent with the thickness of an overgrowth layer obtained via AFM (figure 5.3 (d)). Monoclinic

and hexagonal layered crystal structures of δ-MnO_2 has been reported earlier[182]. The absence of other diffraction peaks owes to horizontally oriented grown crystals with respect to the c-cut sapphire substrate (0006). Due to the absence of the other characteristic peaks, distinction between the monoclinic and hexagonal structures is not conceivable. Since the XRD pattern is not solely informative in clarifying the polymorph phase due to the lack of other useful reflections, transmission electron microscopy (TEM) and Raman analyses are further carried out to determine the crystal structure.

Raman spectrum (figure 5.4 (b)) taken from the as-grown 2D K-MnO_2 nanosheets reveal 9 Raman modes at 196, 236, 280, 406, 470, 506, 557, 577 and 636 cm^{-1} that can be attributed to the monoclinic birnessite phase[183]. The 557 cm^{-1} attributed to the out-of-plane vibrational modes of Mn-O bonds, is typically missing in the Raman spectra reported in the literature. This is due to the disorders in the hydrothermally synthesized manganese dioxides, manifesting itself by broadening of the Raman features[177]. According to the group theoretical calculation, manganese dioxide materials with monoclinic C2/m space group are predicted to show 9 Raman-active modes with 3 A_{1g}+6 B_g species. The 557 cm^{-1} is in-line with the theory but reported as 577 cm^{-1} in the experimental works. The high quality single-crystalline form of our crystals enable us to resolve all the predicted Raman modes. In addition, low frequency peaks are not typically noticeable due to the poor crystallinity of the reported MnO_2 materials. In our spectrum, 280 cm^{-1} is significantly resolved and corresponded to K-O vibrational mode.

X-ray Photoelectron Spectroscopy (XPS) was used to identify the chemical composition and related valence states of Mn (figure 5.4 (c)). Mn 2p scan mainly consists of a spin-orbit doublet corresponding to the Mn $2p_{3/2}$ and Mn $2p_{1/2}$ states around the binding energy of 642.2 and 653.9 eV. To identify Mn oxidation states, the binding energy of Mn $2p_{3/2}$ is considered, which increases progressively as the oxidation state of Mn increases[184]. The asymmetrical Mn $2p_{3/2}$ peak is deconvoluted into two peaks at 641.8, 642.9 eV corresponding to Mn^{3+} and Mn^{4+}, respectively[185][186][187][188]. Mn^{3+} oxidation state is attributed to intercalated K ions rather than oxygen vacancies, where the charge deficit within

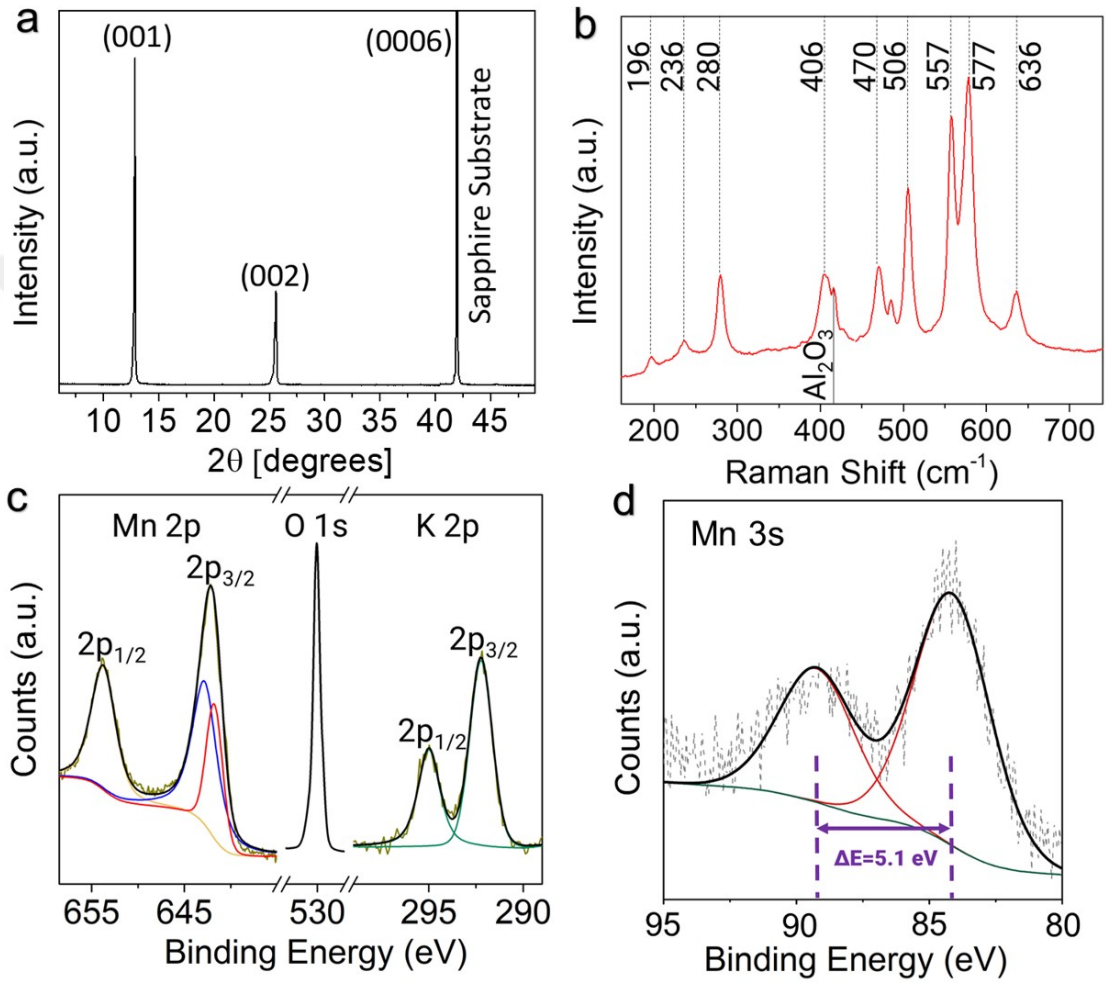

Figure 5.4: Material characteristics of 2D K-MnO_2 nanosheets. (a) XRD pattern from as synthesized crystals on sapphire shows narrow peaks corresponding to the planes parallel to the substrate surface. Consistent with the AFM, interlayer spacing calculated from the (001) peak is ≈0.69 nm. (b) Raman spectrum of a 2D K-MnO_2 crystals on sapphire substrate shows 9 Raman modes marked with dashed lines. Raman peak from the substrate is marked with a solid line. (c) XPS surveys for Mn 2p, O 1s and K 2p peaks. Mn 2p survey shows that the Mn is in +3 and +4 oxidation states as determined by two Gaussians that can be fitted to $2p_{3/2}$. (d) Mn 3s high resolution scan. The magnitude of the splitting in our case is 5.1 eV, that is between 4.7 eV for MnO_2 (Mn 4+) and 5.3 eV Mn_2O_3 (Mn 3+) showing the mixed oxidation state of Mn of 3+ and 4+.

octahedral Mn^{4+} layers is compensated along with K^+ cations[189]. Moreover, the splitting of Mn 3s peaks (figure 5.4 (d)) is often used to qualitatively determine the oxidation state of Mn[190][191]. The obtained ΔE value is around 5.1 eV supporting mixed oxide nature of Mn in K-MnO_2 crystals. The O 1s scan shows a single peak around 530.2 eV which is dominantly coming from the sapphire substrate[29]. K 2p survey exhibits the K $2p_{3/2}$ and K $2p_{1/2}$ peaks at 292.2 and 295.0 eV, respectively, assigned to potassium species residing between the MnO_6 octahedral based sheets.

The free standing K-MnO_2 crystals on TEM grids obtained using the transfer method explained in section 5.2.2. Figure 5.5 shows the highlights of TEM results. Selected-Area Electron Diffraction (SAED) pattern (a) matches with the monoclinic crystal system[181] and confirms the single-crystallinity of K-MnO_2 nanosheets. The observed supercell reflections are consistent with the ordered distribution of the interlayer species. Giovanoli et al[192] were the first to observe the existence of super-reflections in the SAED pattern of synthetic Na-Birnessite. They assumed that these superstructures were caused by an ordering of Mn vacancies. From the analysis of SAED patterns, Post and Veblen[193] concluded that it was most likely that super-reflections resulted from a regular distribution of interlayer cations rather than of vacancies. This is further supported by Manceau et al[194] proposed that the two dimensional super-periodicity observed in the SAED patterns for birnessite particles resulted from a periodic distribution of Na atoms because of their electrostatic interactions. The HR-TEM image (b) conveys the arrangement of Mn atoms without noticeable grain boundaries or vacancy defects. The marked interplanar distance of 0.24 nm corresponds to the (101) plane of birnessite MnO_2[195]. The EDS maps (c) confirm the presence of uniformly distributed K ions all over the nanosheet, along with Mn and O in accordance with the XPS results.

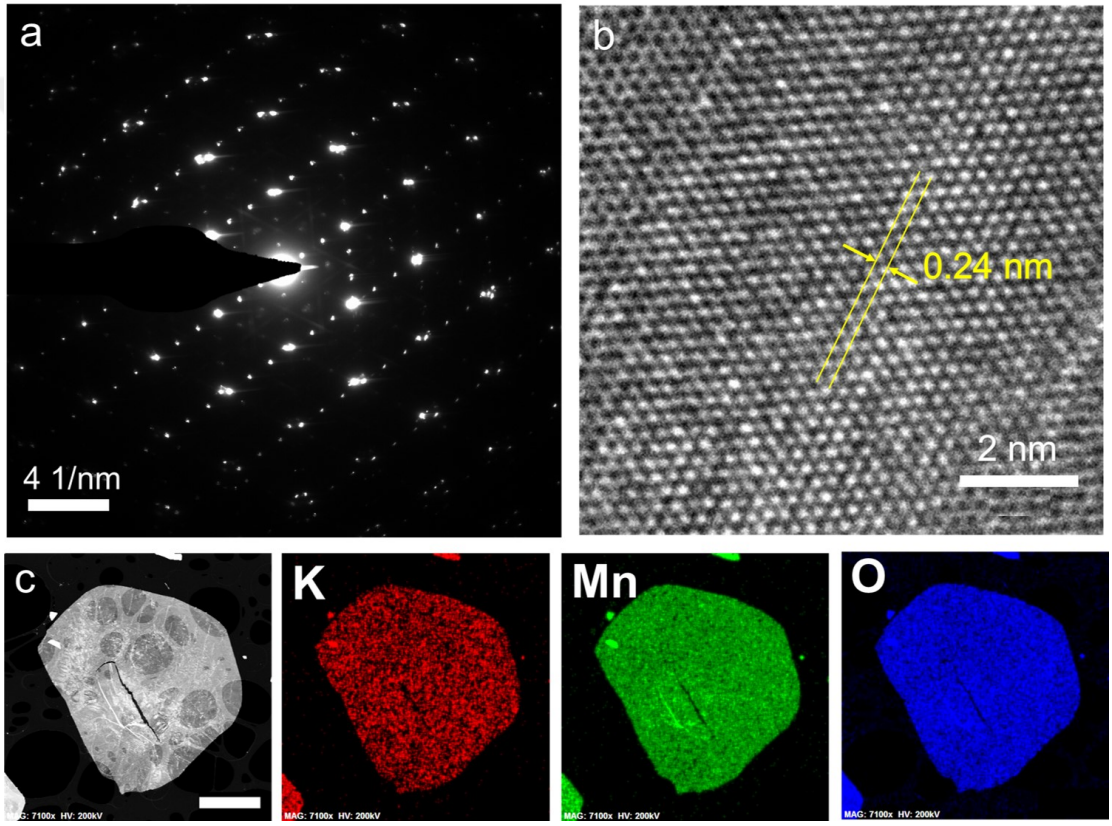

Figure 5.5: TEM analysis of K-MnO_2 nanosheets. (a) The SAED pattern in [001] zone axis, agrees with the monoclinic crystal structure. Supercell reflections attributed to the interlayer cations. (b) HR-TEM image taken through z-axis perpendicular to the crystal. The interplanar distance of 0.24 nm is indicated with yellow arrows, attributed to the (101) plane of birnessite MnO_2. (c) EDS color maps specified with the K, Mn and O elements.

5.3.2 Charge transport in K-MnO_2 devices

Initially, two-terminal gold contact devices are used to evaluate the inception of charge transport in K-MnO_2 nanosheets. Current-voltage (I-V) curves demonstrate a linear I-V with typical resistances ranging in giga-ohms, suggesting the insulator nature of 2D nanosheets (figure 5.6 (a)). In addition, constant current (or so-called galvanostatic) measurement is performed with the application of few nano-amps constant current while recording voltage changes within time (V-t). On this wise, the dominant charge carrier type can be elucidated. As shown in figure 5.6 (b), upon application of the 1 nA constant current, the voltage across the contacts increases with an exponential decay. Similarly, when the current is removed, the voltage across the contacts decays exponentially. In both cases, the experimental data can be fitted perfectly with the empirical formula $V(t)=V_0+V_1e^{(-t/\lambda)}$, where V_0 and V_1 are some constants and λ is the time constant for the exponential decay function. In both rise and decay times, approximately the same λ is obtained. Interestingly, the division of λ over the crystal cross-sectional area ($\lambda/w.t$, where w is the width and t is the crystal thickness) in the ground electrode is constant for the as-fabricated devices. The $\lambda/w.t$ ratio is 81 ± 10 s/μm^2 for three different devices with various contact area configurations. Considering a device with pure electronic conductivity, the contact cross-sectional area should have no effect in charge transport in micrometer scales at the room temperature and λ ought to be less than a millisecond. However, for a mixed ionic-electronic conductor, λ may last several minutes due to the relatively slow motion of ions causing a voltage building up across the contacts. These observations indicate the mixed conductivity nature of charge transport in 2D K-MnO_2 devices. Taking into account the the first recorded voltage value after sending the constant current, compared with the maximum voltage value derived from the saturated built-up potential, the ionic and electronic contributions can be deconvoluted. Consequently, the K-MnO_2 devices turned out to be dominantly ionic conductor up to 90%.

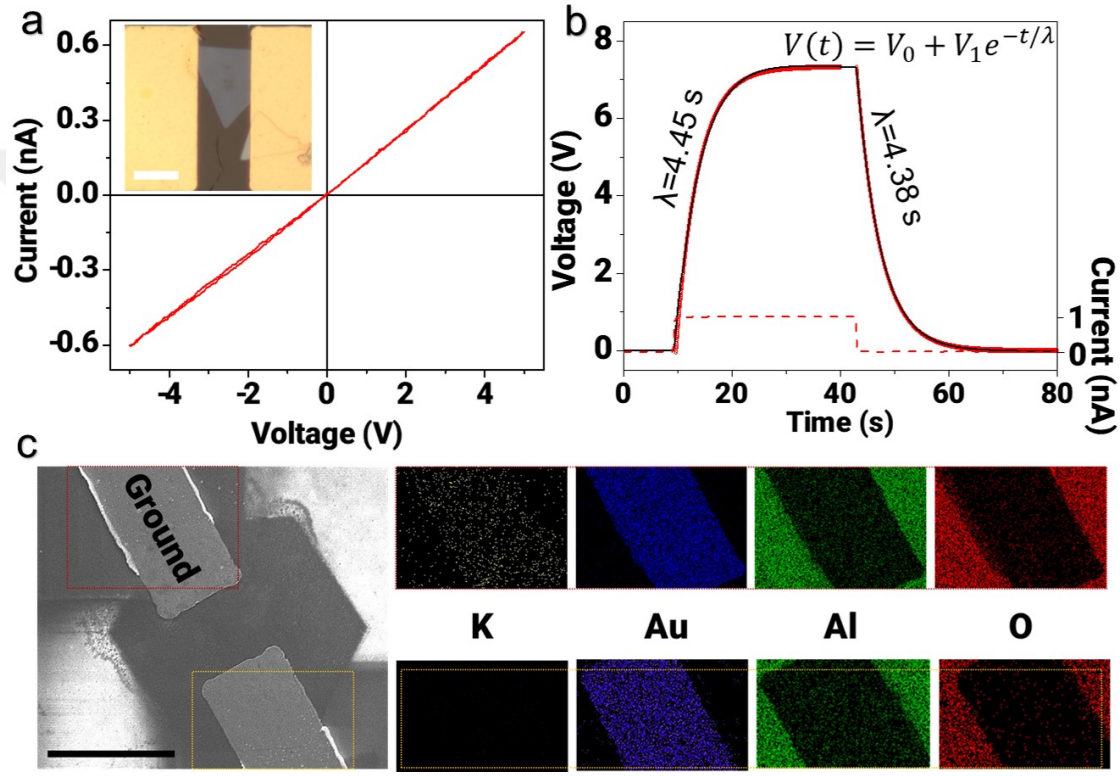

Figure 5.6: Charge transport in 2D K-MnO_2. (a) I-V cycle of an exemplary gold contact device shown in the inset. Scale bar for the inset is 10 μm. (b) V-t scan under constant current shows an exponentially decaying increase and decrease in the voltage response across the electrodes (shown in solid black line). The exponential fit to the rising and decaying parts are given with red circles. λ is the time constant in the exponential function used for fitting the experimental data. Dashed line shows the current applied at various times. (c) SEM micrograph and the EDS maps corresponding to regions in the dashed rectangles at the upper and lower contacts of a positively biased device. SEM image suffered from heavy charging due to the sapphire substrate. Ground contact shows the presence of K whilst the other contact lacks. Scale bar is 20 μm.

The above-mentioned discussion emphasizes the role of cross-sectional area as the designator of delay time in the charge transport, implying the important role of contact electrodes. EDS analysis (figure 5.6 (c)) on the electrodes of a device after applying positive bias with respect to the ground, reveals the presence of K in the ground electrode. This is consistent with the fact that the electric field formed within the material drives the positively charged K ions from the positive terminal to the ground terminal. The electrodes act as a reservoir for the potassium ions which can enter them reversibly, in such a way that the reservoir releases or collects ions depending on the bias polarity.

5.3.3 Water intercalation in K-MnO_2 nanosheets

Although the K-MnO_2 crystals are obtained at high temperatures via a CVD process, further analyses reveal that water molecules exists between the layers. High temperature Raman and XRD as well as room temperature FT-IR measurements (figure 5.7) verify that the K-MnO_2 nanosheets are in hydrous form. High temperature XRD spectra (from 30 to 150 °C) taken in ambient environment (figure 5.7 (a)) show (001) peak shifting towards higher 2θ angles, which takes place between 100 and 120°C. Such a contraction in d-spacing is attributed to the removal of water molecules (so-called water crystal) in the hydrous form of birnessite[196]. The (001) peak shifts back to its original upon cooling, which conveys reversible water intercalation in K-MnO_2 from the moisture in the ambient. No other peaks appear in the XRD patterns during the heat cycling (figure 5.7 (b)), indicating that the peak shiftings are not due to a phase transition. Accordingly, we presumes the grown crystals at high-temperatures, upon cooling absorb water from the air environment in the CVD process. Moreover, Fourier transform infrared spectroscopy (FT-IR) measurement (figure 5.7 (c)) on the crystal confirms the presence of O-H vibrational modes.

Likewise high-temperature XRD results, Raman spectra taken at various high temperatures in ambient (figure 5.7 (d)) reveal a reversible scattering change after cooling. The 557 cm^{-1} peak in the Raman spectrum of pristine K-MnO_2

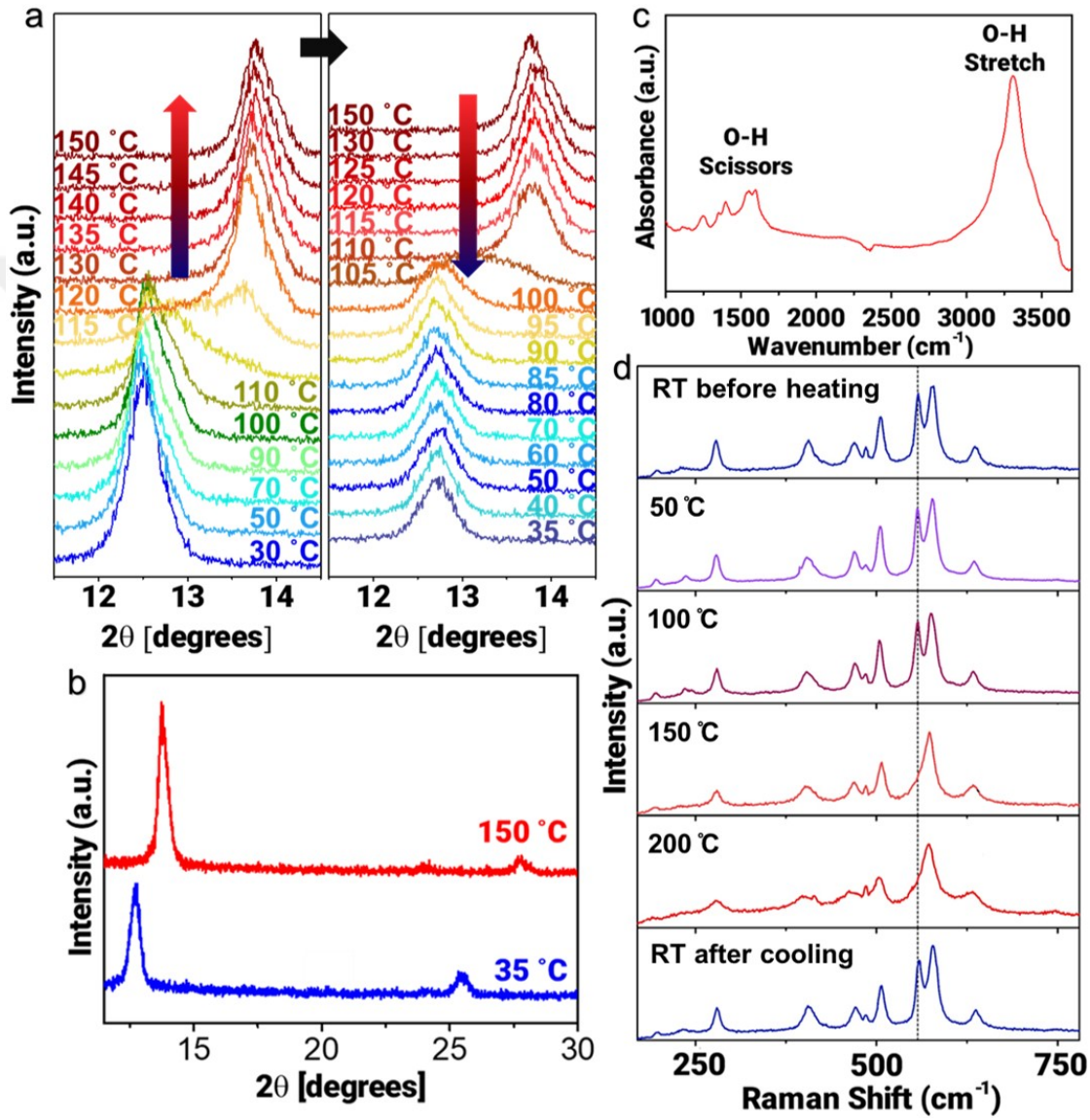

Figure 5.7: Perception of water crystal via high-temperature characterizations in ambient. (a) XRD spectra taken at various temperatures upon heat cycling under the ambient. (b) Wide XRD scan shows how (001) and (002) peaks shift with no additional peaks appearing. (c) FT-IR absorption spectrum indicating the presence of O-H vibrational modes attributed to the interlayer water molecules. (d) Raman scatterings collected under the ambient at various temperatures. Upon cooling down to the room temperature, the pristine spectrum is obtained.

(attributed to the Mn-O out of plane vibrational modes) diminishes above 100 °C and reappears upon cooling. Once more, the reversible Raman evolution via heat cycling can be interpreted as the reversible removal/absorption of water molecules from the ambient. As will be discussed in the following, such a reversible phenomenon plays an important role in the charge transport of 2D K-MnO_2 devices.

5.3.4 Adaptations under vacuum heat cycling

To further elucidate the water effect interpretations, electrical and physical properties of K-MnO_2 nanosheets are studied in high vacuum medium. The resistance of devices dramatically increases while being vacuumed. Figure 5.8 (c) shows the change in electrical resistance of a device vacuumed using a rotary vane pump followed by turbo-molecular pump down to 6.5×10^{-3} mbar. The chamber is firstly pumped with rotary vane pump ($\approx10^{-1}$ mbar) (region i , in which the resistance slightly increases linearly). While the molecular pump is speeding, a dramatic rise is observed in ii, followed by an exponential increase over a course of an hour after stabilization of the pump down to 6.5×10^{-3} mbar. The resistance changes are attributed to the continuous water removal which is boosted when the molecular pump comes into play. The resistance drops rapidly while venting the chamber, indicating the water absorption back into the structure. While the device is under high vacuum, upon the heating cycle (figure 5.8 (d)), the resistance decreases exponentially form tens of giga ohms down to hundreds of mega ohms. There is a slight slope change observed during heating (red curve in (d)) around 65 °C, which coincides with the onset of Raman changes and XRD shiftings. Therefore, this can logically attributed to the water loss, which is absent upon cooling (blue curve in (d)). The discontinuity in the heating/cooling curves is due to the I-V cycle taken at high temperature that changed the resistance state of the device.

Likewise the high-temperature ambient Raman measurements, the 557 cm^{-1} peak in the Raman spectrum of the pristine K-MnO_2 diminishes above 50 °C and remains absent upon cooling to room temperature under vacuum (figure 5.8 (b)). This change is perfectly synchronized with the XRD peak shiftings (figure

5.8 (e)) in terms of the temperature. Note that the XRD peak shift takes place around 100 °C when the heat cycling is performed under ambient (figure 5.7 (a)). Similar to R-T and Raman measurements, the 2θ position shifts back to the original value at room temperature upon venting the XRD chamber with air.

The combination of R-T, Raman and XRD measurements in vacuum through heat cycling convey relatively fast water in/de-intercalation into the nanosheet structure. Taking into account the 557 cm^{-1} peak evolution under presence or absence of crystal water, we track the changes over a large K-MnO_2 crystal, comparing its response at different locations (edge and center) to evaluate how water enters into the structure. Accordingly, under a controlled vacuum environment, series of Raman scatterings collected by parking the laser at edge or center of the crystal shown in figure 5.8 (a). At the end of the heat cycling in vacuum, the chamber is vented with argon (99.999% purity) or air at room temperature, and in both cases the 557 cm^{-1} peak retrieved back while spotting the edge region of the crystal. However, the 557 cm^{-1} peak remains missing while measuring the center regions after sending the Ar gas. Despite the purity of the Ar gas, we consider moisture out-gassing of the chamber and the vacuum lines introducing a small dose of moisture. This lets us follow the Raman response of the center region in time (rather than fast response in venting the chamber). The 557 cm^{-1} peak reappears from the edges of the crystal within a few minutes (our measurement duration is limited by the time to collect the Raman spectrum) and after several minutes, it reappears at the center of the crystal. This experiment evidences the fast reversible water intercalation at the edges but slower at the center regions of the crystal. Furthermore, it points out that the back and forth water cooperation is the intercalated one (water crystal) rather than the adsorbed moisture.

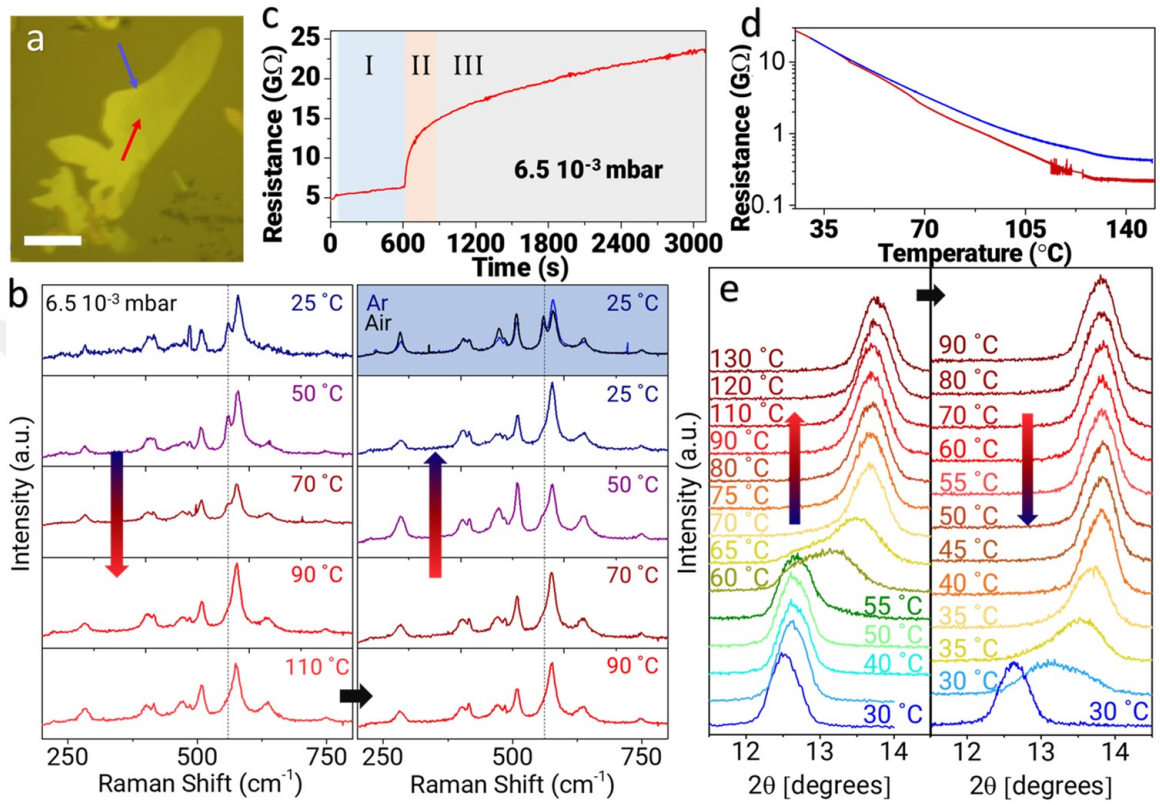

Figure 5.8: Measurements under vacuum environment. (a) Optical image of a large K-MnO_2 crystal used for high-temperature Raman measurements in vacuum. The position of the Raman spectra collected over the crystal is indicated with blue and red arrows corresponding to the edge and center, respectively. (b) Raman scatterings taken at various temperatures under vacuum and after venting the chamber with air and Ar. The arrows show the increasing and decreasing temperatures. The dashed lines in both left and right panels indicate the position of the 557 cm^{-1} peaks. (c) Resistance versus time measurements when the measurement chamber is pumped with i. rotary vane pump (10^{-1} mbar) ii. speeding of turbo molecular pump, iii. final pressure of the chamber (6.5×10^{-3} mbar). Resistance of the device increases over a course of an hour. (d) Resistance versus temperature (R-T) graph shows the resistance change of the device during heating (red) and the cooling (blue). The slight slope change of the heating curve around 65 °C coincides with the changes observed in Raman and XRD measurements. (e) XRD θ-2θ scan obtained at various temperatures under vacuum and after breaking the vacuum at 30 °C. The blue lines in both left and right panels are taken under ambient. Upon heating, at the onset of 60 °C, the (001) peak exhibits a shift. Upon cooling, the peak is reverted to the pristine position around 30 °C and fully recovers after venting the chamber with air.

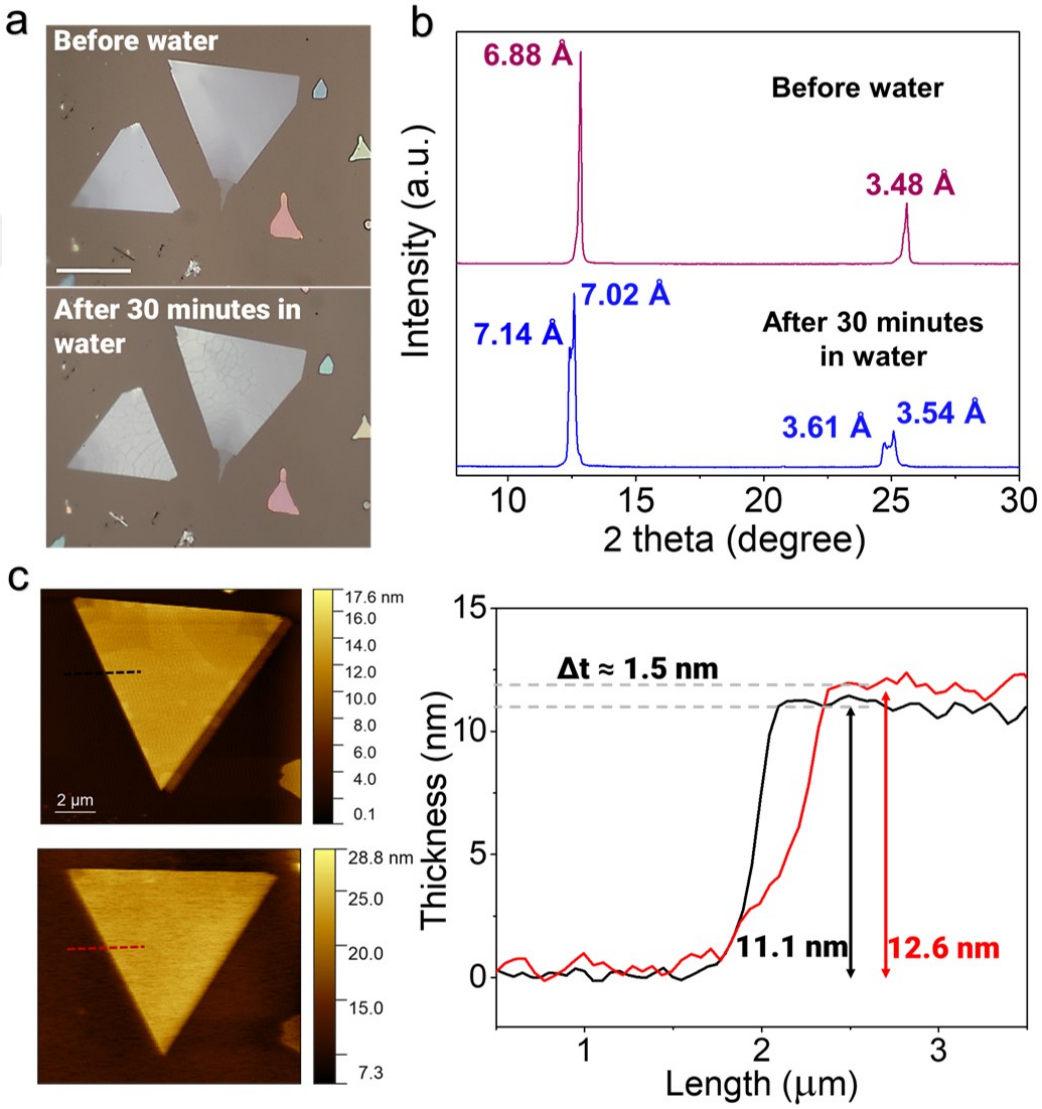

Figure 5.9: Effect of water exposure on K-MnO_2 crystals. (a) Optical microscope micrographs of K-MnO_2 crystals before and after 30 minutes of immersion in water. (b) XRD patterns taken before and after 30 minutes water immersion. (c) AFM scans of a K-MnO_2 crystal before and after water immersion. The height difference complies with the increase in the interlayer spacing of the crystal.

5.3.5 Serving excess water to K-MnO_2 crystals

So far, incorporation of moisture form ambient is shown to alter the properties of K-MnO_2 nanosheets. Rationally speaking, a question arises that how the level of water exposure may affect the crystals. I would like to note that the K-MnO_2 crystals are not fully water-proof. When the crystals are dipped in water for extended durations (30 minutes), they show significant changes in their morphology, thickness and interlayer spacing determined by XRD and AFM measurements. Figure 5.9 (a) compares the optical images taken before and after serving water. The XRD results show an increase in the interlayer spacing. The broadening of the peaks after immersion can be attributed to slight variations in the water concentrations of various crystals as XRD spectrum is collected from a large area of the substrate with many crystals. The optically visible cracks along with the expansion observed in XRD and AFM result (b and c), make us to avoid water exposure (for example washing the growth samples with water) before all the characterizations or device fabrications.

5.3.6 Electric-field induced phase transitions in K-MnO_2 devices

The dominant conduction of K ions in K-MnO_2 devices, manifests itself as a clear optical contrast change when sufficiently large electric-field is applied. Thanks to the optical access over the 2D active area in the devices, we are able to observe and study the contrast changes which imply phase transitions during the electrical measurements. Figure 5.10 (a) shows a series of optical microscope images taken over the course of 20 minutes when the device is biased with 10 V across the contacts. Reversible color contrast changes are observed near the electrodes, depending on the polarity of the applied biased. A bright contrast region appears in the vicinity of the positively applied electrode (10 V) and expands towards the ground terminal with time. The color change disappears by bias removal and reappears near the ground terminal if a negative bias is applied. Raman analysis of the different contrasty phases discloses the bright phase to have distinctly

different Raman spectrum than the pristine crystal, corresponding to the Raman scattering reported on the synthetic birnessite with only water water intercalated across the layers but not cations[183]. This phase is termed "watery phase" in the following text. The low-wavenumber Raman band around 280 cm^{-1} (attributed to the stretching modes of KO_6 groups) is mainly diminished (figure 5.10 (c) blue curve), indicating effectively moved K ions accompiend with the separation of the hydration layer. According to these observations, the formation of the watery phase and K ions movement is quite reversible. When the bias is removed, crystal reverts to the pristine phase, or application of negative biases forms the watery phase near the ground counter electrode. The reversibility arises from the in-plane motion of K ions. Considering halide perovskite as a ionic conductor example, due to the random 3D walk of iodide ions under the applied electric-field, the pristine phase cannot be obtained after effective movement of iodides[197]. However, in our case, as demonstrated in schematics (figure 5.10 (b)), K ions can enter the electrode reservoir under bias, forming behind the watery phase which moves the opposite, and eventually this structural change can revert to its pristine or form the other way around by the reverse polarity applied biases.

Sweeping the voltage incrementally across the electrodes, we observe a hysteresis in the I-V curve. The induction of structural change with respect to the voltage magnitude is the key to generate a hysteric I-V, as it is linear in a shorter range I-V sweeps (figure 5.6 (a)). Through large bias (16 V) applied to a gold contacted device, a significant clockwise hysteresis appears in the IV curve. Figure 5.10 (d) shows three consecutive I-V cycles. This implies that disturbance of the K ions from their equilibrium along with their slow motion leads to the observed hysteresis. I would like to note that under mild applied voltages, a large hysteric I-V can be obtained via laser illumination. This adds up another interesting privilege to study the optoelectronic properties of K-MnO_2 which requires further investigations.

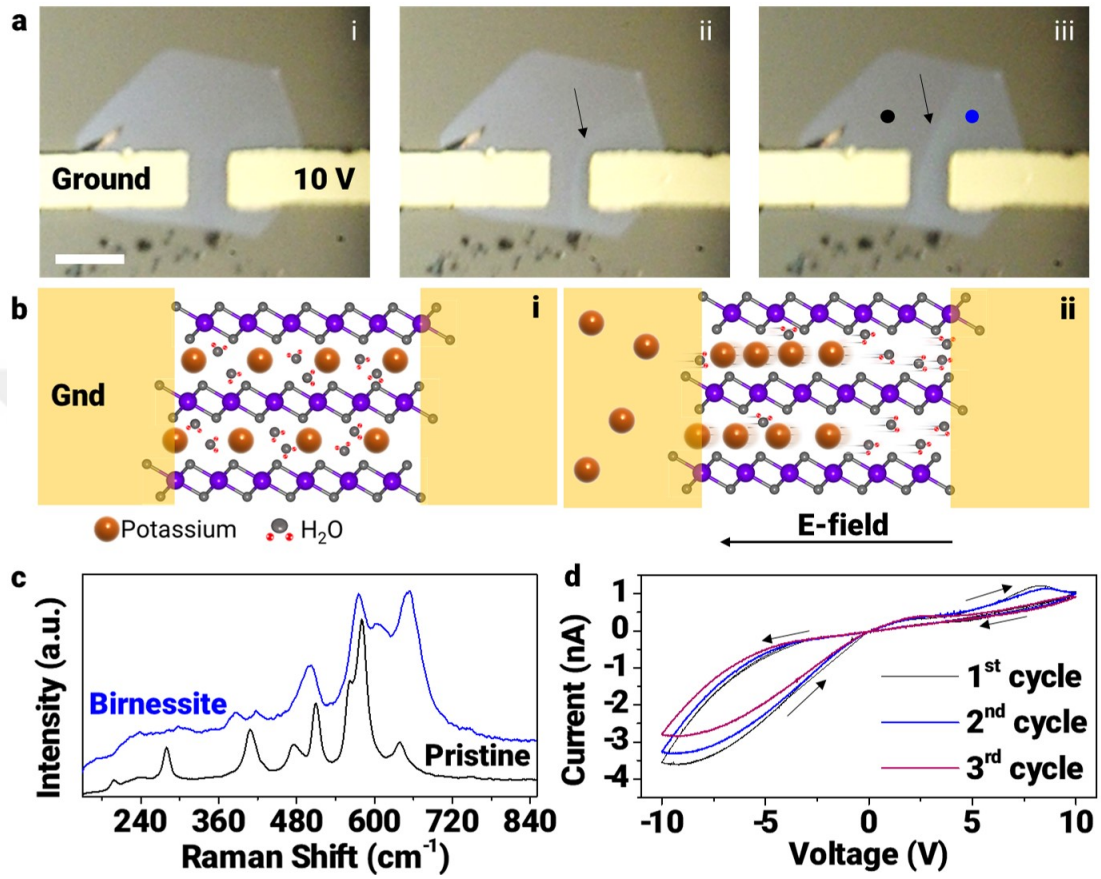

Figure 5.10: Electric-field induce phase transition due to ion separation. (a) A series of optical microscope images taken under 10 V bias over the course of 20 minutes shows the appearance of a bright contrast region near the positive electrode. i. shows the image captured when the bias is applied, ii. after 10 minutes and iii. after 20 minutes. The black arrows point to the boundary of the bright and dark contrast regions. Black and blue dots marked on the image indicate the positions that Raman spectra are taken from. Crystal thickness is 6.6 nm. The scale bar is 20 μm (b) Schematics depict the condition when i. no bias is applied and ii. when bias is applied. The potassium ions and their hydration layer get separated under the electric field. Accordingly, the bright contrast region on the right electrode corresponds to the birnessite formation with no potassium ions. (c) Raman spectra taken from the different contrast regions of the crystal under bias as marked in a-iii with black and blue dots matches with the pristine (black curve) and with the birnessite (blue curve) reported in the literature. Absence of 280 cm^{-1} in the spectra from the bright contrast region indicates no K-O stretching. (d) Three consecutive I-V cycles taken from a device after application of 16 V. A broad hysteresis in clockwise direction appears. This can be explained by the sluggish response of ion movement from the contacts to the material and separation of water and potassium within the material. The large asymmetry in the I-V curve can be explained by the asymmetry of the contact configuration.

5.3.7 Memristive behavior via layered to spinel phase transition

Taking into account the structural schematics shown in figure 5.1, we hypothesize that through effectively large depletion of K ions and water molecules, the spinel phase can be promoted out of the layered structure. The size of vacant position in the tunnel structure is typically too small to accommodate any ions or molecules. We realize that with the application of huge biases (> 100 V), a dramatic color change and accordingly a phase change can take place. An example of such a dramatic reversible phase transition is experimentally demonstrated in figure 5.11 on a highly biased K-MnO_2 device. The bright and dark contrasty regions are being moved back and forth between the contact electrodes (i-v), based on the bias polarity (see supplementary movie 4 for the entire video).

The Raman spectrum obtained from the dark contrasty phase (figure 5.11 (b)) does not match with neither the pristine nor the watery phase. This implies formation of a different phase upon severe torturing the device with the application of huge voltages. Along with the *in-situ* optical observations, we notice that the device resistance significantly jumps while the dark contrasty phase is promoting, and drops in case of bright phase reappearing . This intimates emergence of low resistance and high resistance states (LRS and HRS), controlled by the history of the applied bias; therefore, potentially a memristor. However, the magnitude of the applied voltages to change the state of the device is far too large to compete with analogous memristors. Especially, when two-dimensionality is taken into account, the expectation is much higher in terms of energy consumption. Although a hysteric I-V can be obtained via gold contact devices (figure 5.10 (d)), the LRS/HRS (known as ON/OFF) ratio as well as the memory volatility are serious issues restraining the desired figure of merits. To tackle these challenges, contact engineering of K-MnO_2 devices should be investigated. Besides Au, we tried Cr, In and Al but no significant progress attained. The reservoir energy towards K ions is still high enough to be kicked by the application of low biases. At this point, considering graphene as one the famous preferred cathode for K-ion batteries[198], we hypothesize that If multi-layer (ML) graphene with more

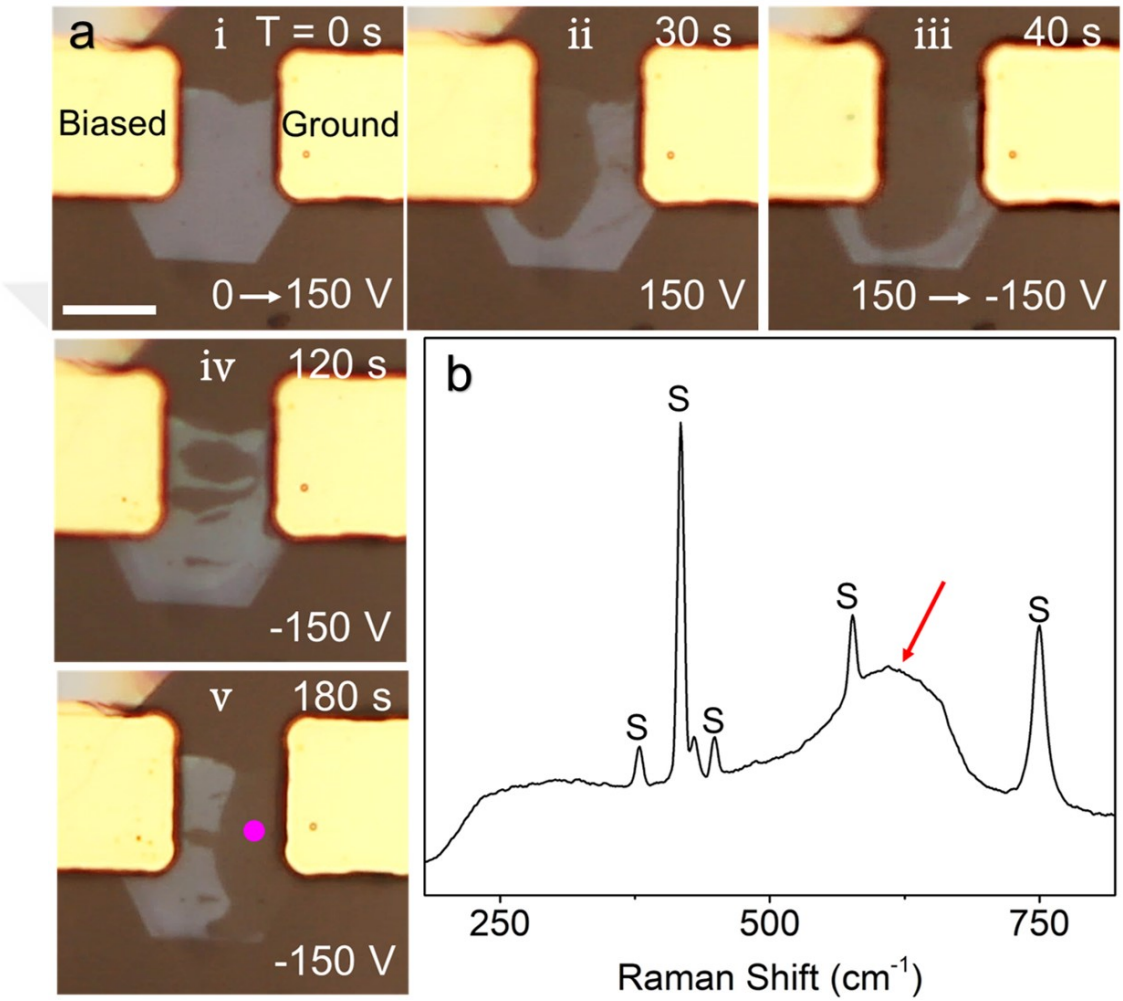

Figure 5.11: *in-situ* observation of layered to spinel phase transition in a highly biased device. (a) Series of optical microscope images taken during biasing of a two-terminal device of K-MnO_2. The scale bar is 10 μm. The first image (i) shows the moment just before applying 150 V (T = 0 s) and the consecutive images show the evolution of optical contrast of the crystal. After 30 seconds (ii), more than half of the crystal shows less contrast with respect to the substrate. At 40 seconds (iii), the bias is reversed, -150 V with respect to ground is applied. Within 80 seconds (iv) a phase with different contrast than the pristine crystal appears. Finally (v), the less contrasty phase appears near the ground electrode. (b) Raman spectrum taken at the pink circle point marked in (v). The broad peak around 640 cm^{-1} is marked with the red arrow. The intense peaks marked with S are due to the sapphire substrate.

affinity towards potassium is chosen, the bias at which the charge depletion takes place can be lowered.

Figure 5.12 shows the I-V curve taken from the inset Gr/K-MnO_2/Gr device at room temperature in ambient. We exfoliated ML graphene electrodes from bulk graphite using the sticky tape method and transferred the graphene flakes over the K-MnO_2 crystals via a deterministic stamping method. Then, indium needles are placed over graphite electrodes at elevated temperatures for electrical contacts. A large clockwise hysteresis compared to the gold contact devices is obtained via using Gr electrodes. Beginning from 0 V to positively applied biases, the device is in low resistance state (LRS) up to 5 V (i) until the negative differential resistance (NDR) appears. In the NDR range (marked in the I-V graph), the resistance switching takes place (LRS to HRS). The device maintain its state while sweeping from 8 V to 0 V (ii). In the negative sweeping cycle, a large deviation observed while scanning from 0 V to -4 V. Further decreasing the bias (iii), again a large NDR is observed and thus LRS to HRS switching. While sweeping back to 0V and fulfilling the I-V curve (iv), the device stays in its HRS which can be referred to the reset state.

Such an interesting hysteric I-V curve potentially implies forming a memory which depends on the history of applied biases and thus a memristor. Before establishing a technical memristor application, we investigate the mechanisms behind the obtained hysteresis to understand the physical changes over I-V scans. It is well-known that the ML graphene can reversibly take alkali ions to form alkali-carbons and modulate the charge transport by causing reversible phase transitions[199]. Taking this into account, via optical the access to the 2D K-MnO_2 devices, we optically track the changes on devices and perform *in-situ* Raman spectroscopy during the I-V cycling. Furthermore, Electrostatic Force Microscopy (EFM) and TEM characterizations are employed to explain the electrical and physical changes pertaining to the switching mechanism.

The optical observations during I-V cycling are shown in figure 5.13 (a) (see supplementary movie 5 for the entire video). One of the Gr electrode is fixed to the ground while the voltage is swept through the other one. As shown in figure

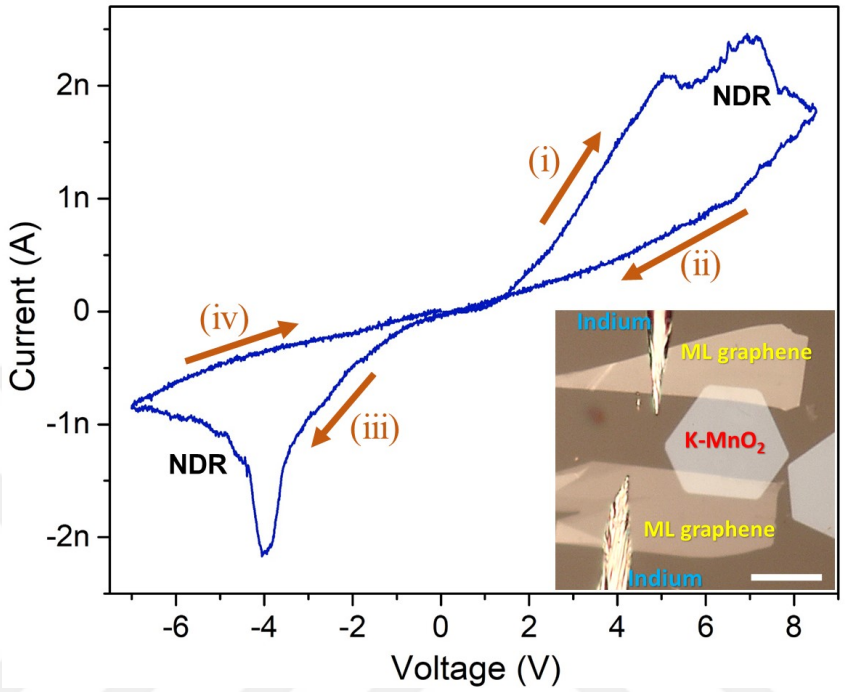

Figure 5.12: A typical I-V curve taken from a representative Gr/K-MnO_2/Gr device (shown in the inset). The scan paths are marked on the clockwise hysteresis. the scale bar for the inset is 20 μm.

5.12, beyond a certain voltage the device exhibits NDR. The current through the device decreases with the increasing voltage, and the device switches from LRS to HRS. Interestingly, the onset of this switching accompiend with a significant optical changes. A depletion motion is clear from the biased to the ground electrode, developing the dark contrasty phase. Likewise the gold contact devices, the watery phase emerges near the biased electrode. Upon sweeping back to 0 V (HRS), no optical change (phase transitions) is observed and the device preserves its state. While sweeping in the negative half-scan, again the optical changes appear while entering the NDR region. Conversely to the positive half-scan, the dark phase relocates from the ground to the biased Gr electrode and vice versa for the watery phase. This reversible color changes (phase transitions) along with the observed hysteric I-V curve, implies a non-volatile memory whose LRS to HRS (set and reset) switching relies on dynamic phase transitions induced by electric-field.

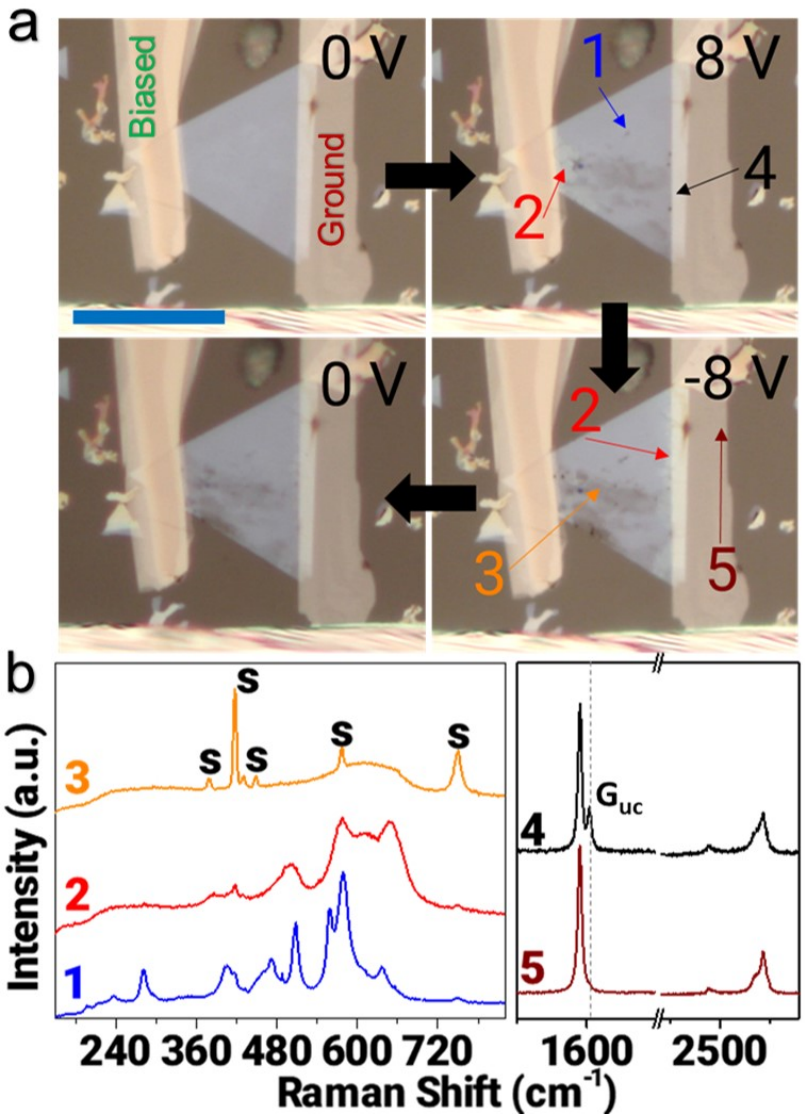

Figure 5.13: *in-situ* observation of electric-field induced phase transitions. (a) Optical microscope images taken during the I-V cycling show contrast changes on K-MnO_2 at different biases. Upper left panel shows the pristine crystal. The bias sweeping is followed by the black arrows. Colored numbers with arrows show the positions where Raman spectra are collected on the sample during the I-V cycling. Scale bar is 20 μm. (b) Raman spectra collected from points marked on a. Blue line (1) matches with the Raman peaks of the pristine K-MnO_2. Red line (2) taken from near the positive electrode (i.e. the electrode with higher potential) shows the birnessite Raman. Orange line (3) taken from the less contrasty region near the negative electrode shows a very broad Raman band near 600 cm^{-1}. All the sharp peaks in the spectrum belongs to the sapphire substrate, marked with "S". Black line (4) is taken from the graphite electrode over the crystal. The peak indicated with a grey dashed line shows the Raman band corresponding to KC_{72}. Maroon line (5) shows the Raman spectrum over graphite at a distance to the crystal. KC_{72} peak is missing.

The observed NDR and its concurrence with the optical contrast changes can be interrupted by two phenomena: (1) Deficiency of charge transport contribution of partially depleted K ions which migrate to the Gr electrodes. (2) Layered structural collapse as a result of of hydrated potassium depletion and transition to spinel-like structure. The first point is proven via Raman spectra (figure 5.13 (b)) collected from the graphene electrode after taking a half-cycled I-V. The emergence of a new peak (G_{uc}) in the G band confirms formation of potassium-carbon species and effectively intercalated graphite crystal by K ion, matching with KC_{72} reported in the literature[199].

To prove the second point, firstly, the different contrasty regions are studied by Raman. As depicted in figure 5.13 (b), three different Raman scatterings are detected out of the three contrasty phase, namely the pristine phase (1), the watery phase (2) and the dark phase (3). The dark phase Raman lacks characteristic sharp peaks to be clear identified and just show a very broad Raman band near 600 cm^{-1} that can be attributed to mixture of various structures (all the sharp peaks in the spectrum belong to the sapphire substrate, marked with "S"). When this dark region is illuminated for several minutes with high intensity laser beam, a sharp Raman peak gradually evolves that can be attributed to the formation of like Mn_3O_4[173]. Figure 5.14 (b) shows the evolution of the Raman peaks (starting from the dark contrast phase in 1) upon illumination with a few mW 525 nm laser beam (laser spot marked in (a)). A peak around 659 cm^{-1} gets intense by repeating the Raman measurements. The final Raman spectrum (graph 5) can be attributed to the spinel-like Mn_3O_4 phase. It has been reported that under severe depletion of K ions and water from the structure, layered-to-spinel phase transition can take place in a reversible fashion[174][200][201]. To further support this claim, we mimic a same structure by transferring crystals over TEM grids and illuminating them with high intensity laser beam. We optically observe a significant color contrast change after collecting the Raman spectra (figure 5.14 (c)). Figure 5.14 (d) shows the Raman evolution (starting from the pristine phase in 1), indicating almost the similar final Raman scattering as panel (b). Much smaller laser intensity is sufficient for the phase transition here due to the free-standing configuration of the crystals and lack of heat dissipation.

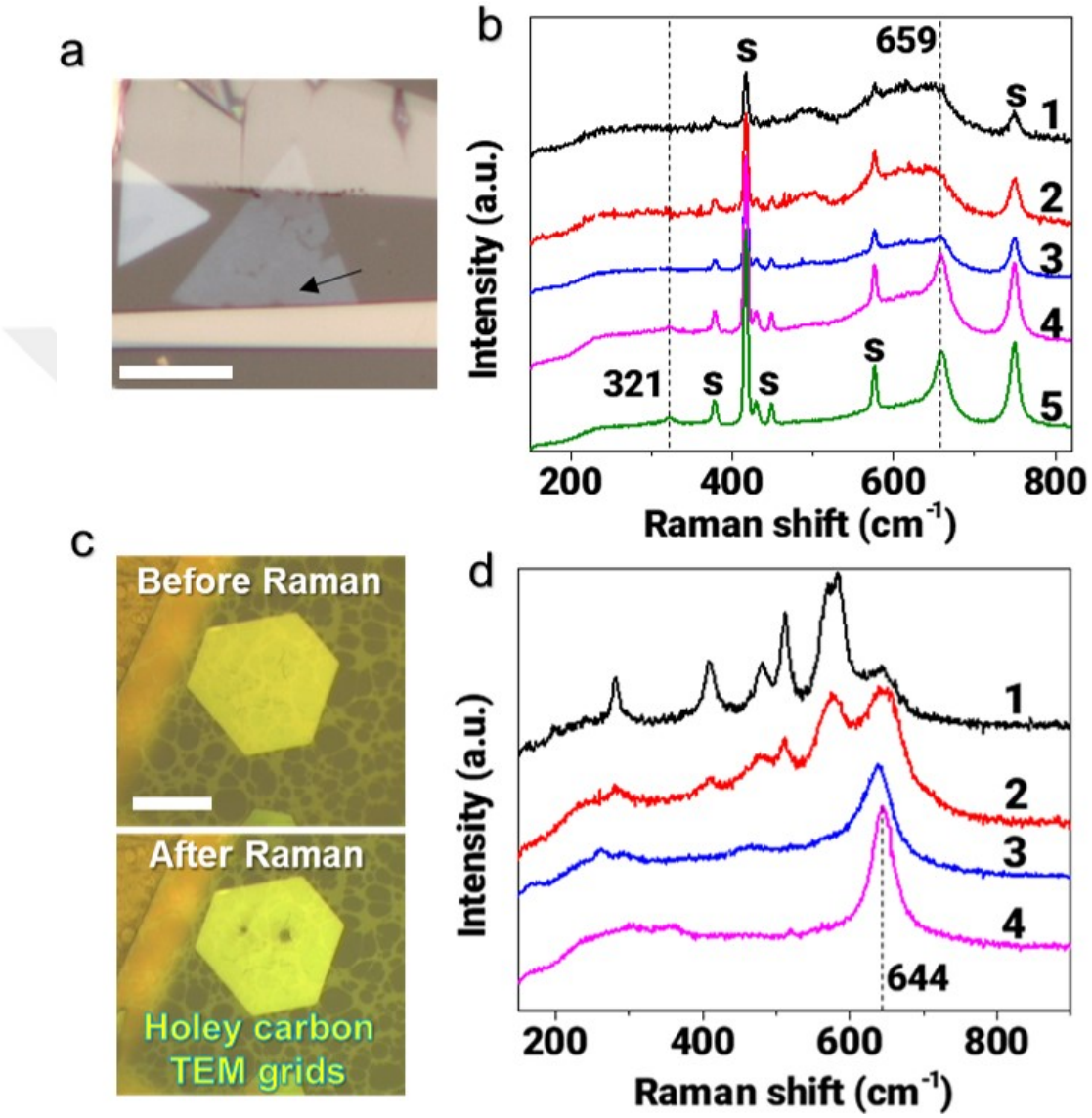

Figure 5.14: Raman evolutions under the emergence of spinel-like Mn_3O_4 phase. (a) Optical microscope image of a Gr/K-MnO_2/Gr device. The arrow indicates the region where Raman spectra are collected. (b) Raman spectra taken from the same spot over 4 cycles with a few mW laser power at 532 nm. The spectrum after the 4th cycle matches with Mn_3O_4. Dashed lines indicate positions of 659 and 321 cm^{-1} that are the characteristic peaks of Mn_3O_4. The sapphire substrate peaks are labeled as "S". (c) Optical microscope images before and after the Raman measurement of a K-MnO_2 crystal suspended over a holey carbon TEM grid. Notice the dark contrast region over the crystal, where the spectra are collected. (d) Evolution of the Raman spectra over gradual illuminations exhibits a similar trend to the device shown in a. The scale bar for (a) is 20 μm and 10 μm for (c).

Both samples (shown in figure 5.14) have undergone optical and Raman changes under laser illumination, merging into a relatively same final Raman response at the final state. However, one can argue about the oxidation or severe damage of the crystals rather than layered to spinel-like transitions. To clarify this, we have analyzed the TEM samples w/o laser illumination. We create some parallel-line patterns over a large suspended crystal and study them in TEM with respect to the pristine regions. Figure 5.15 (a-d) shows HR-TEM images and SAED patterns taken from the pristine and illuminated regions.

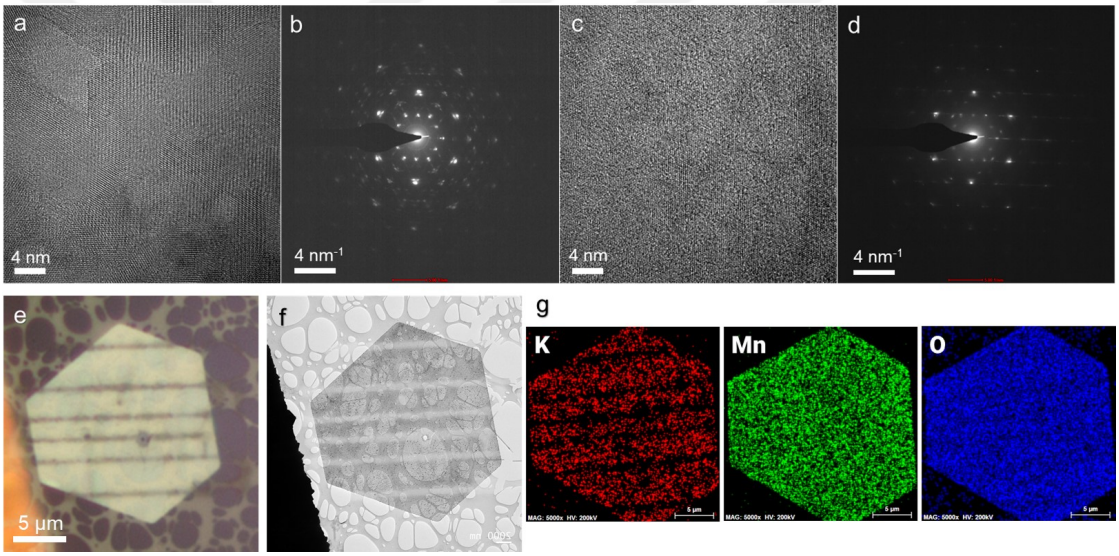

Figure 5.15: Laser-induced layered to spinel-like phase transition. (a) HR-TEM image taken over the laser illuminated regions shows patches with different crystal orientation. (b) Corresponding SAED pattern shows polycrystallinity. (c) HR-TEM image taken from the same crystal, at a pristine region. (d) No polycrystallinity is evident. (e). Optical microscope image of a purposefully patterned crystal and corresponding (f) bright field TEM image shows contrast in the electron transmission corresponding to the lines created with illumination. (g) Strikingly, the EDS maps collected from the crystal show lack of potassium over the laser-patterned regions.

HR-TEM from the illuminated regions demonstrates formation of islands with different orientations whose polycrystallinity can be realized by its corresponding SAED (b). The pristine regions exhibit more uniformity and single-crystallinity in (c) and (d), respectively. It has been shown that larger Mn_2O_3 crystallite size intensifies the 660 cm^{-1} Raman peak[202], which is quite consistent with

the Raman evolution observed under longer laser illumination. Accordingly, the polycrystallinity distinguished in the illuminated sample can be interpreted by the Mn_3O_4 crystallites grown by the local laser heating. Moreover, the tunnels in the spinel-like structure are too small to accompiend any cations. Therefore, it is expected to detect no K ions in the illuminated regions. EDS maps (g) taken from the deterministically laser-patterned crystal (e) reveals absence of K ions in the illuminated regions. This observation further supports the similarity of the phase transitions in TEM samples and Gr contact devices in which layered to spinel-like transitions induced by severe depletion of K ions.

Thanks to the access to the active area of the 2D Gr/K-MnO_2/Gr devices, the optical contrast changes upon the phase transitions and thus resistance switching can be further studied by Electrostatic Force Microscopy (EFM). This analysis enables exploring the mesoscopic mechanisms responsible for the observed memristive-switching characteristics synchronized with the layered MnO_2 to spinel-like Mn_3O_4 transition. Upon all the EFM scans (figure 5.16 (g-f)), 3 V is applied to the cantilever while the voltage across the device is tuned via the source Gr electrode. The color contrast changes are visible in (c) compared to the pristine (b). I would like to note that no thickness variation is observed upon the color changes (phase transitions) and the 22 nm thick crystal maintains all over the EFM scans. The resistance of the device is monitored during the scans. Upon application of negative biases up to -4 V, no significant potential changes were observed and the device sustains in LRS. Once -5 V applied to the source, the resistance starts increasing, implying LRS to HRS switching and thus NDR state. The line profile graph (g) shows a potential drop (larger field) at the source in the reversed-biased HRS compared to the forward-biased LRS. Nap phase potential scan at -5 V demonstrates significant variations (d), especially near the source electrode. A large potential drop is observed within the crystal at the boundary where the layered transits to the tunnel structure. Since the negative biases are being applied to the source electrode, the positively charged K ions drive to the lower graphite, hence the ion depletion and phase transition occur mostly around the negatively biased electrode. The abrupt change of the cantilever phase in the EFM images across phase boundary indicates that the

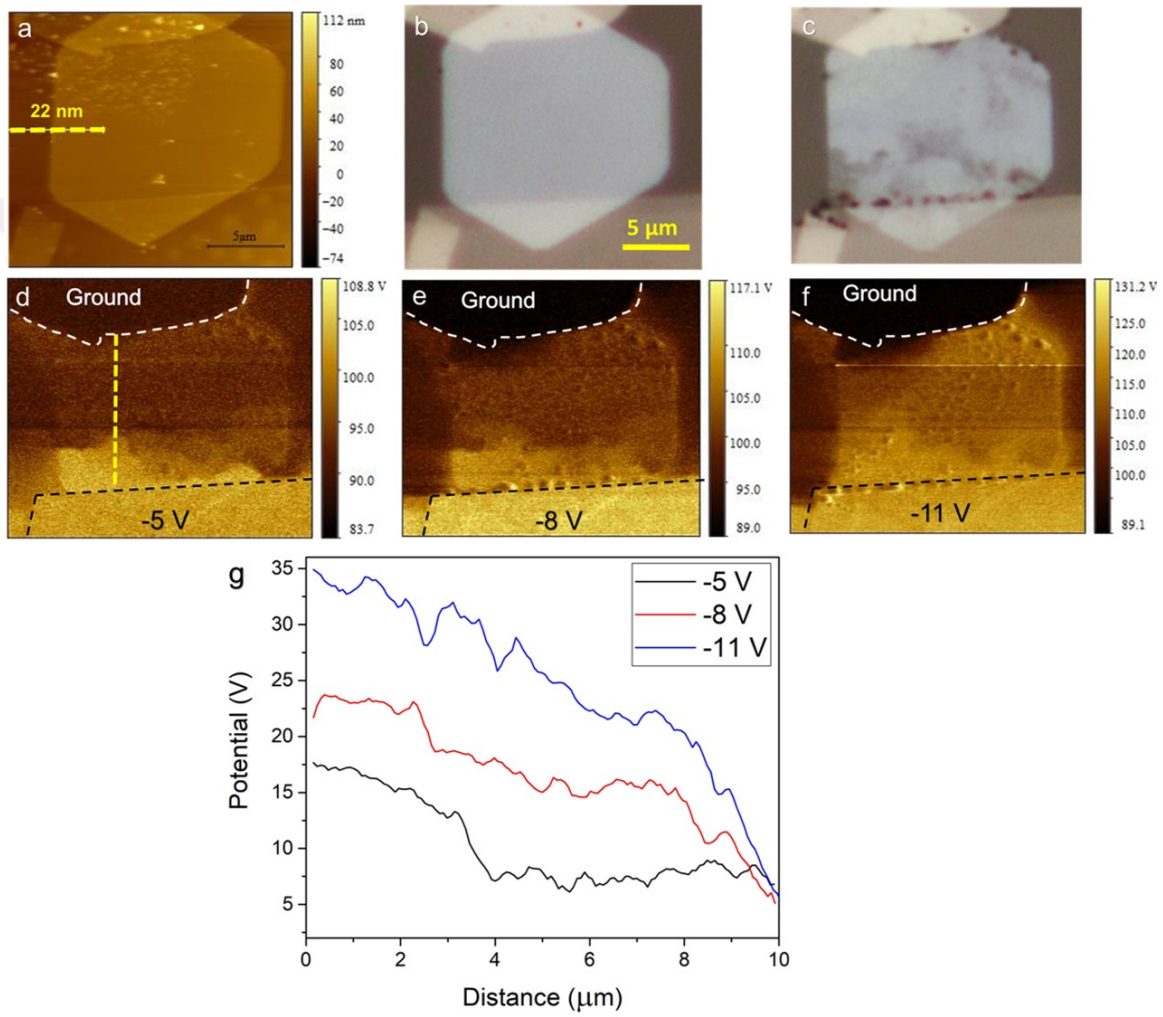

Figure 5.16: EFM analysis of the electric-field induced phase transitions. (a) AFM height trace map of a Gr/K-MnO_2/Gr device. The thickness through the whole crystal maintains 22 nm upon all the applied biases. (b) and (c) Optical microscope images taken before and after the EFM measurements, respectively. (d-f) Nap phase potential maps taken at different negative biases applied to the source electrode, while the tip is biased by 3 V. (g) Potential changes over the dashed line (shown in d) from the biased Gr electrode towards the ground one.

electrostatic potential drops primarily at the boundary (that is, the boundary is resistive). Around 3 μm further from the biased electrode, the potential drops fast as seen in the black curve shown in (g). Such an abrupt potential change (corresponding to the boundary of layered and tunnel phases) becomes shallower in the scans when larger negative biases are applied (e and f). At these scan, the LRS to HRS switching rate becomes almost saturated and the resistance still decreases but much slower. Comparing the -5 V and -11 V scans, it is clear that the potential drop at the phase boundaries has decayed. This is due to the development of the tunnel phase towards the ground electrode due to the departure of more ions upon larger biasing. Analysis of multiple line profiles verifies that the sharp potential change in the vicinity of the Gr electrodes is the key information related to the LRS to HRS switchings. This dynamic switching manifest itself as differential negative resistance in I-V curve, whose onset coincides with the onset of the MnO_2 layered to Mn_3O_4 spinel-like phase transitions.

With all the Raman, TEM and EFM as well as *in-situ* optical analyses taken into account, the electric-field induced phase transitions along with the in-plane ion motions play the dominant role in the resistance-switching mechanism of 2D K-MnO_2 memristors. For such a reverse transition, moisture from the ambient is required[154]. As the bias is reversed, potassium ions migrate from the ground electrode to the crystal. This creates a charge imbalance in the structure and attracts moisture in the ambient to compensate the deficit[175]. One optical observation of such a phenomenon is the appearance of small water droplets near the Gr electrodes after many I-V cyclings (figure 5.17 (a)). To experimentally demonstrate this, we perform electrical measurements under lack of moisture around. Under high vacuum environment, neither hysteresis nor phase transition observed upon I-V cycling, even with the assist of high laser power illumination. Moreover, when the devices I-V cycled at elevated temperatures in ambient (figure 5.17 (b)), the hysteresis starts diminishing above 100 °C, the temperature which is the onset of water removal according to the XRD results in ambient. After cooling down to the room temperature, the hysteresis is totally collapsed and a linear I-V is obtained (figure 5.17 (c)). All the discussed observations are consistent with the fact that potassium ions depleted from the structure requires

ambient moisture to enter the crystal again.

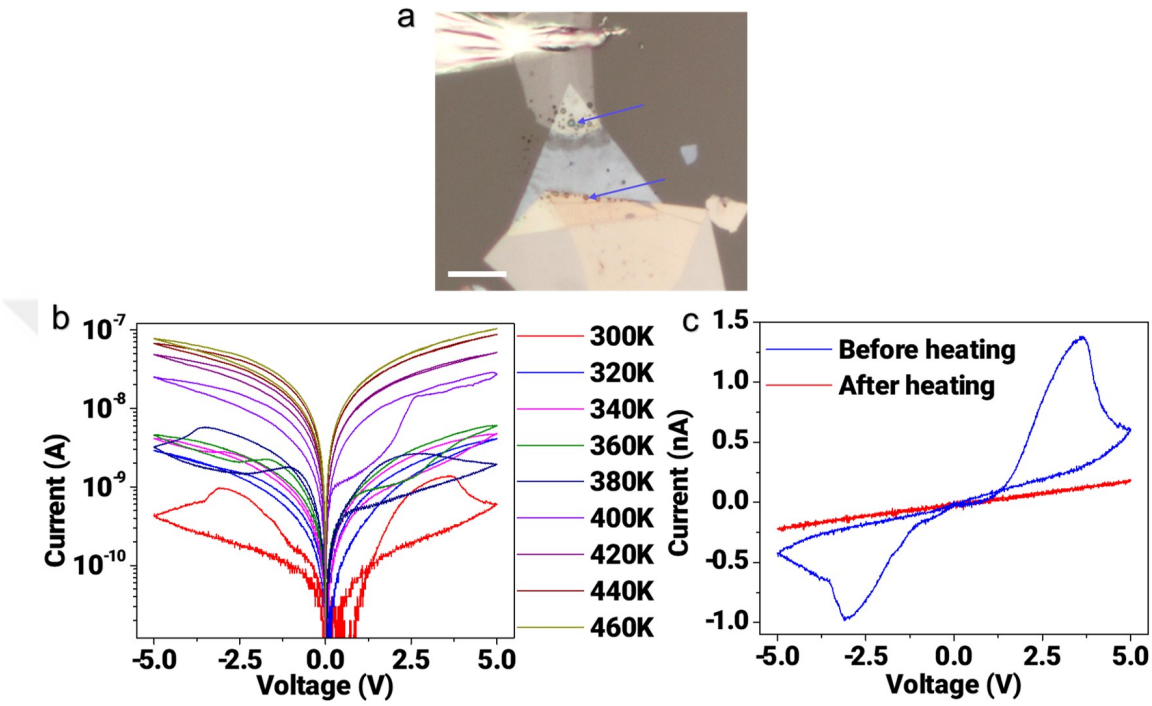

Figure 5.17: Role of water moisture in resistance-switching mechanism. (a) Optical microscope micrograph of a device after several I-V cycling showing small droplets near the Gr electrodes. Blue arrows indicate the droplets whose formation is visible under optical microscope during I-V cycling. (b) I-V curves taken at various high temperatures. The hysteresis persists up to 380-400 K and diminishes at higher temperatures. (c) I-V scans before and after the high-temperature I-V cyclings. Room-temperature scan after heating shows a linear I-V curve where the hysteresis is entirely lost.

5.3.8 Artificial neuromorphic synapse mimicking

So far, intrinsic ionic transport and modulation properties have been discussed in graphite contact K-MnO_2 devices. Realizing these features in 2D materials may open up new approaches for bio-mimicking neuromorphic devices[130]. The synapse is a junction between two neurons, which controls their interactions through controlling passage of electrical or chemical signals across the neurons and plays a central role in information processing and storage of neural networks[203]. A schematic of a synaptic junction in a network is depicted in

Figure 5.18 (a). Mimicking synapses with artificial components may enable integration of large-scale neural networks with low power consumption. The synapses interact through the sparks in tens of milliseconds by injection/depletion of neurotransmitters. As a result of their interactions, neuron plasticity is modulated through competition for neurotransmitters, so-called Plasticity Related Particles (PRPs). There have been many efforts with different strategies[204][205][206] to mimic the synapse plasticity modulation via PRP transmitting. The dynamic weight of plasticity can be analogous to the conductance of the artificial devices. The conductance of the artificial device should be capable of being incrementally increased/decreased via pulsed trains, corresponding to the synaptic excitation/depression respectively. In addition, the device should maintain its functionality through torturing by large number of excitation/depression cycles, namely Endurance test. To demonstrate the neuromorphic capabilities of K-MnO_2 based devices, we conduct a series of experiments including potentiation, depression, and endurance. Figure 5.18 (b) shows a typical hysteric I-V obtained from the device shown in the inset. The main objective is to catch the intermediate states between LRS and HRS to tune the device conductance incrementally. To test this ability, first we monitor the conductance change by single or double bias pulses. Two pulses of 25 ms temporal width at pulsing voltage V_P= 4 V separated by 1.5 second causes a gradual change in the conductance of the device, i.e., facilitation of the synapse. Read voltage $+V_R$ is set to 1 V to prevent changes in the resistance state of the device. As shown in (c), the device conductance has been increasing incrementally although the major change caused by the input pulses is lost. This indicates a large forgetting curve, yet non-volatile depending on the pulse magnitude. This small conductance modulation (0.13 to 0.14 nS) can perfectly mimic Short Term Potentiation (STP) of a single synaptic junction, in which the major processed information is forgotten but not the minor ones. When the number of input pulses increases, we observe larger conductance changes. This modulation depends on the pulse magnitude and duration, which can reversibly switch between low and high conductance states, implicating the discussed reversible phase transitions. Long term potentiation (LTP) and depression (LTD) are successfully accomplished with respect to the amplitude (d) and duration (e) fo the input pulses. This enables varying degrees of conductance

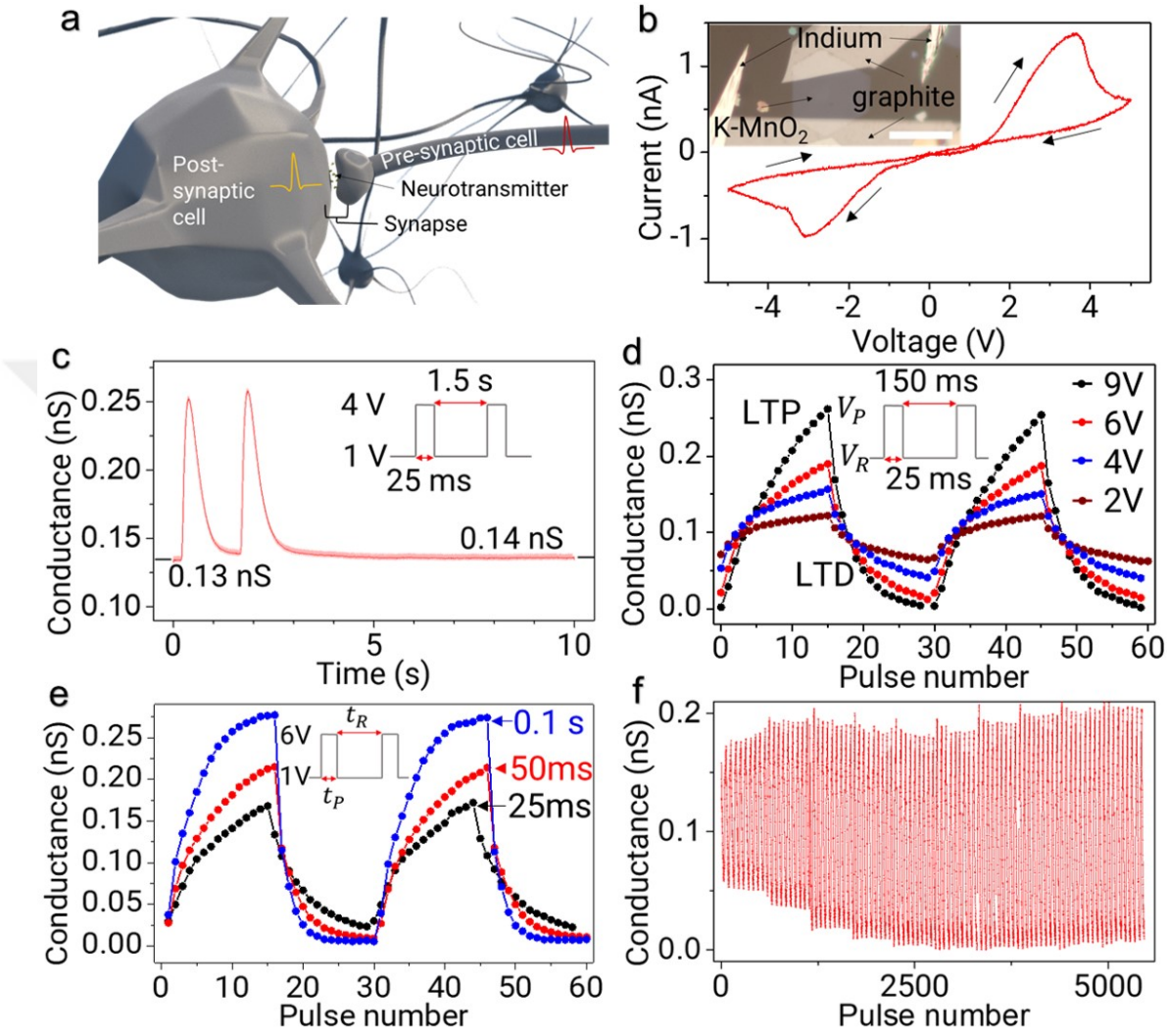

Figure 5.18: Artificial synaptic emulation via Gr/K-MnO_2/Gr devices. (a) Schematic depiction of a synapse in a neural network. K ion motions may mimic the role of neurotransmitters in an organic synapse. (b) I-V cycle from a Gr/K-MnO_2/Gr memristive device. Sweep direction is indicated with black arrows on the I-V curve. Inset shows a typical device. Scale bar is 20 μm. (c) Short-term potentiation (STP) of the device with 26 nm crystal shows a gradual change in the conductance of the K-MnO_2 memristor. The inset shows the pulse train. The conductance value is read with 1 V. Two spikes that are 1.5 s apart at 4 V with 25 ms temporal width are sent to induce the change. (d) Long-term potentiation (LTP) and depression (LTD) are shown in the figure. LTP is shown with postive pulse voltages (+V_P) and LTD with negative ones (-V_P) while the read voltage V_R=-1 V. Pulses are separated by 150 ms and lasted for 25 ms. (e) Effect of pulse duration on LTP and LTD is shown. Longer pulse durations result in more significant facilitation of the synapse plasticity. (f) Result of the Endurance test. Conductance modulation via LTP and LTD shows endurance up to 5600 pulses.

modulation, demonstrated by two consecutive courses of pulse trains in (d) and (e). By repeating these course, the endurance of the devices has been evaluated. Potentiation and depression repeated over more than 5500 cycles shown in (f), verifying acceptable endurance of the devices upon cycling.

The above-discussed artificial synaptic mimicking concept is succeeded for a single synapse (single Gr/K-MnO_2/Gr device). However, there are billions of neurons in the brain, each of which has on average 7,000 synaptic connections to other neurons[207]. Accordingly, mimicking a single synapse might be interesting but pretty much useless for large integration and scalable information processing. Despite fabricating numerous memristors with neuromorphic synapse computing capability, due to the lack of emulating the communication between synapses, the devices end up with an impractical neuromorphic application. In this regard, we experimentally demonstrate tha the Gr/K-MnO_2/Gr devices can interact with each other. We fabricate two-synapse devices by integrating them with a common graphite electrode. the optical microscope image of the device is shown in figure 5.19 (a). To evaluate the ionic coupling between the connected devices, S1 is undergone stimulation by pulsing and then S2 response is measured. Note that the common Gr electrode is kept grounded during the measurements, thus while pulsing S1, no bias is being applied to S2. Before pulsing, the initial resistance of S2 is measured via a short-range I-V cycle (blue curve in figure 5.19 (b).). The voltage range is limited to -0.5 to 0.7 V in order to prevent any resistance changes upon the I-V cycling. This short-range sweeping is repeated couple of times to assure that the resistance stays unchanged. subsequently, S1 is stimulated by 100 pulses of 50 ms with 5 V amplitude. Despite the fact that S2 was untouched during stimulation, its resistance jumps from 2.3 to 4.3 giga ohms. After applying each pulse course to S1, the resistance of S2 is measured. While S1 undertakes larger pulse magnitude, the resistance of S2 increases further (figure 5.19 (b)). This observation conveys the possibility of ionic coupling between two K-MnO_2 synapses configuration.

The results imply that, in principle, it is possible to use graphite as an ion transport channel acrossthe memristors to mimic synaptic competition and cooperation behaviors. A more detailed study is required to elucidate the mechanisms underlying the coupling effect.

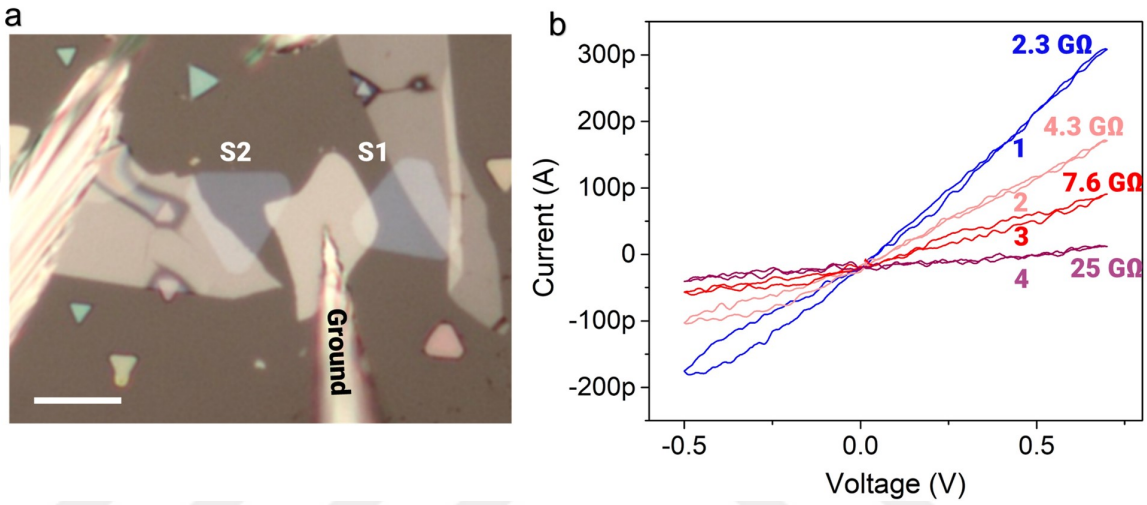

Figure 5.19: Ionic coupling effect in integrated K-MnO_2 devices. (a) Optical microscope image of a two-synapse device to illustrate the synaptic competition. S1 is the first synapse that is undergone pulsing, S2 is the second synapse that responses to the pulsing. the scale bar is 20 μm. (b) Monitoring the resistance of S2 by short range voltage I-V sweepings. The reduction in the conductance of the S2 due to the pulsing of S1 is clear. The voltage range is limited to -0.5 to 0.7 V to prevent any changes occur due to the I-V cycling. (1) is the first I-V cycle on S2 before pulsing S1. I-V on S2 after pulsing S1 with 100 pulses of 50 ms with 5 V amplitude (2), after 100 pulses of 50 ms with 10 V amplitude (3) and after 100 pulses of 50 ms with 15 V amplitude (4). Resistance after each cycling is noted on the graphs.

At the end of this chapter, I would like to emphasize that the CVD grown 2D K-MnO_2 crystals are quite immune towards oxidation with excellent stability in ambient. As synthesized K-MnO_2 crystals are exceptionally stable under the ambient conditions as studied by Raman and electrical measurements over four months-old samples (figure 5.20).

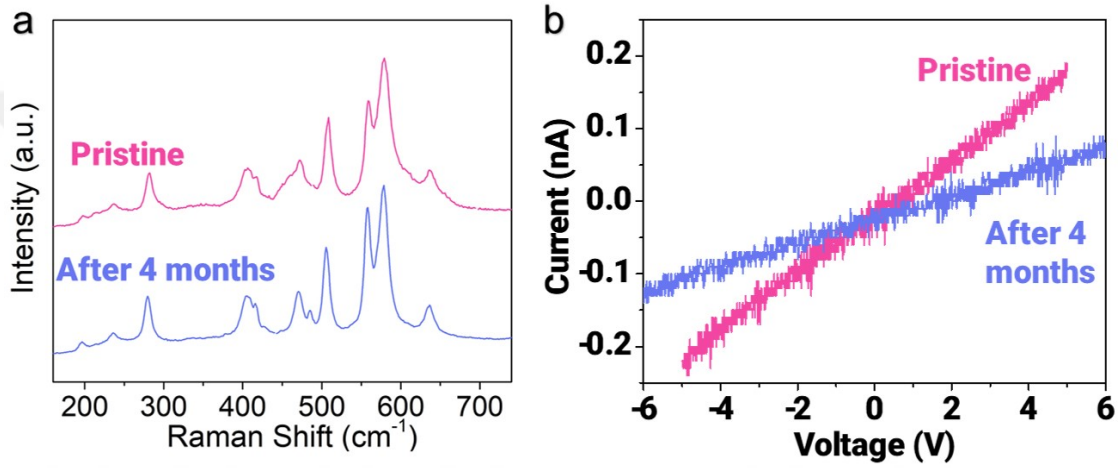

Figure 5.20: Long-term stability of K-MnO_2 crystals. (a) Raman spectrum from a crystal right after the growth and after four months in the ambient. 557 cm^{-1} peak intensified slightly as compare to the pristine crystal. This might be explained by further intercalation of water across the layers. (b) I-V curve from a device after several measurements and after four months in the ambient. the device became slightly more resistive, consistent with higher water content across the layers.

Chapter 6

Conclusion and future prospects

Synthesis of atomically thin transition metal dichalcogenides (TMDCs) using chemical vapour deposition (CVD) techniques has been gaining ever growing attention as CVD may offer a scalable route to achieve the unique technological possibilities offered by TMDCs. Recently published papers on salt assisted CVD growth of TMDCs[26][28] are a mere demonstration of the significance of the topic. However, as mentioned in chapter 3, the underlying mechanisms behind the synthesis route still remain rather elusive. To elucidate this, for the first time, we monitor the CVD growth of TMDCs in real-time, allowing us to differentiate the dynamic effect of each mechanism as well as growth parameters. we study how a custom-made CVD furnace that allows real time optical observation and control of the crystal formation can be used to understand the growth of atomically thin TMDCs. As a demonstration of the versatility of our methods based on the custom-made CVD chamber, we work on a detailed analysis of WSe_2 monolayer synthesis and applied the knowledge we gained on synthesis of other atomically thin 2D materials such as $MoSe_2$. The real-time observation of the growth allows us to to pinpoint the reaction routes leading to vapour-solid-solid (VSS) and vapour-liquid-solid (VLS) growth modes for the salt-assisted TMDCs synthesis. In addition, realizing complicated effect of growth parameters is much straightforward as no event is missed during the growth. As an example, we study the role of H_2, introduced at different growth states. Finally, we identify

the growth condition to obtain both lateral and vertical WSe_2-$MoSe_2$ heterostructures, thanks to the unique *in-situ* control. Accordingly, by adjusting the growth temperature and controlling the precursor heater temperature, we show the control over the synthesis of lateral and vertical heterostructures. After publishing the results[29], other research groups take advantage of VLS growth modes employed in wafer-scale and deterministic patterned growth of TMDCs[55][208].

Realizing the VLS growth mode and the condition it is promoted over the VSS, may be a key to accomplish deterministic TMDC growth. More knowledge about the VLS mode can lead us to be in a new position to control the liquid intermediate compound to synthesize TMDCs in pre-determined patterns[209][210][55]. To potentially illustrate how our custom-made CVD chamber can be employed to study patterned crystal growth via directing sodium tungstate liquid, we fabricate HfO_2 channels on oxidized Si chips using standard optical and electron beam lithography. Figure 6.1 (a) shows a patterned substrate with channels formed by 10 μm wide, 24 nm tall HfO_2 walls. Fine NaCl:WO_3 mixture of 1:2 weight ratio is placed at one end of the channels. The reaction between the salt and the metal oxide precursor produces Na_2WO_4 droplets of various sizes on the substrate surface, whose viscosity depends on the unreacted WO_3 concentration in the droplet. As the temperature goes above 700 °C, Na_2WO_4 spreads through the channel upon contact with the channel ends due to the capillary action (figure 6.1 (b)). After the introduction of H_2 and Se, particularly the liquid that crawls along the channel walls forms WSe_2 crystals. Figure 6.1 (c) shows formation of crystals in circular channels. Although the monolayer formations presented here have multi-layer patches, it would be possible to control the layer thickness by adjusting the channel wall dimensions and the precursor concentration.

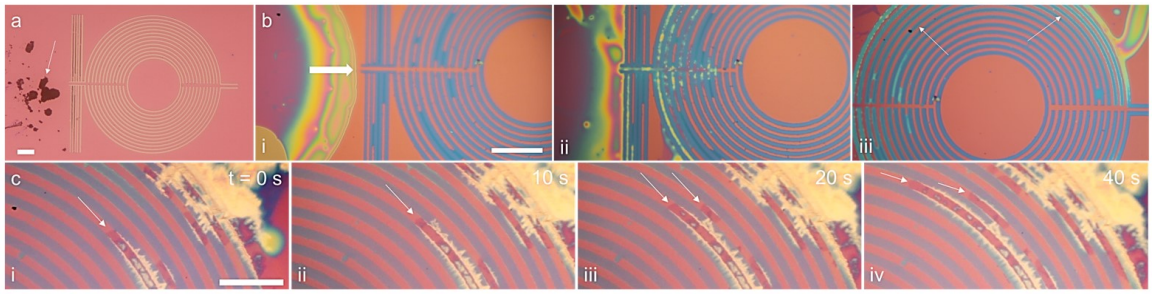

Figure 6.1: Control of the molten intermediate compound for deterministic patterned TMDC synthesis. (a) Optical micrograph of HfO_2 channels patterned on an oxidized silicon chip. The white arrow indicates 1:2 weight ratio mixture of NaCl:WO_3 grain. (b) A series of optical micrographs (i-iii) taken during the liquid Na_2WO_4 spreading through the channels at 750 °C. The white arrow in i indicates the direction liquid enters the channel and the arrows in iii show a thin liquid residue left on the channel walls. (c) A series of images (i-iv) taken several seconds apart, demonstrating how the liquid precursor turns into WSe_2 by following the channels. Scale bars are 100 μm in a, b, and 50 μm in c.

Optical observations can be accompanied by other spectroscopic measurement techniques that can be incorporated on to the chamber to provide real time spectroscopic information about the intermediate phases. The RTO-CVD method we demonstrate in chapter 3 can be extended to investigate any other material that can be synthesized using the CVD technique and the impact of this work may be much broader than the 2D materials community.

Chapter 4 embraces one of the most important studies on V_2O_3 in the past few years. The main reason for this claim is based on our novel findings for CVD synthesis of single-crystal V_2O_3 nanoplates that has been missing so far. By using these crystals, we unraveled new aspects of the supercritical state. A similar breakthrough happened 15 years ago for VO_2 via the synthesis of its nanobeams by Hongkun Park's group[67]. Use of high quality nanobeams resulted in increase of our understanding of the solid-state phase transitions as bulk and film samples of strongly correlated materials suffer from formation of domain structures in the vicinity of the phase transition boundaries. So far, the best way to obtain V_2O_3 has been epitaxial growth of the crystals over a lattice-matched substrate. However, this significantly limits the extend of studies that can be performed on

the films as the stresses induced by the substrate dictates the physical properties. One way to circumvent this problem is doping the crystals. Yet, there is increasingly more evidence that the nature of the phase transitions in doped and pristine V_2O_3 are inequivalent. Although, there have been numerous attempts to achieve high-quality V_2O_3 crystals that are smaller than the characteristic domain size, most chemical routes yield non-stoichiometric mixtures of different oxidation states.

Thanks to the *in-situ* control and observation of growth in RTO-CVD, in chapter 2, we developed a CVD recipe for single-crystalline V_2O_3 nanoplates synthesis. we characterized the synthesized V_2O_3 nanoplates in detail and studied the Raman response of as grown and exfoliated crystals from room temperature to the supercritical state where the phase boundary that separates the paramagnetic insulating and metallic phases disappears. We found that Raman active modes along the corundum c-axis become independent of the stress and the initial phase the crystal was in. We explained this observation based on crystal field theory. We observed emergence of a novel crystal structure upon electron beam heating in selected area electron diffraction experiments consistent with the Raman measurements. Finally, we illustrated the electrical properties of both as-grown and transferred V_2O_3 based devices. Besides these significant findings, we propose that a few nanometer thick V_2O_3 plates would be a very suitable test platform for field-effect experiments based on various regions of the phase diagram. High-quality V_2O_3 nanoplates that we introduce in this work can be both tensiley and compressively stressed. This may provide a unique opportunity to study the phase stability diagram of pristine V_2O_3. In particular, these crystals may enable a detailed study of supercritical state and cross-over along the Widom line[211] that separates the Mott insulator like and correlated metal like regions.

The V_2O_3 nanoplates can be used in the study of van der Waals-like novel heterostructures for reconfigurable thermals, electronics and optoelectronics[212][213][214]. As an example, we measured thermal conductivity of metallic V_2O_3 crystals, to demonstrate the applicability of our new methodology by which thermal conductivity measurements in nanosheets via bolometric effect is demonstrated[215]. The thermal conductivity of the PM phase has been

reported as 4.5 $W.m^{-1}.K^{-1}$ at room temperature[216]. The results are in an excellent agreement with the value reported in the literature.

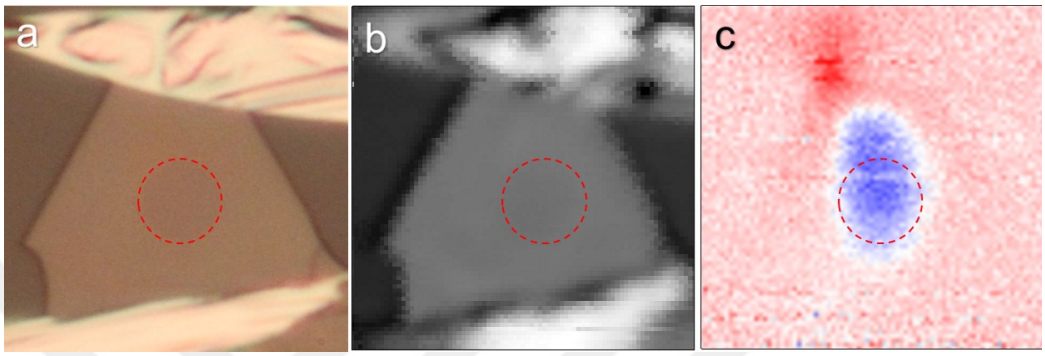

Figure 6.2: Bolometric photocurrent methodology for calculating thermal conductivity of V_2O_3 crystal (a) Optical micrograph of V_2O_3 crystal. The dashed red circle denotes the position of the hole, over which the crystal is suspended. (b) Reflection map and (c) the photocurrent map. Slight elongation of the bolometric response towards the contact is possibly due to an air pocket trapped under the crystal[215].

In chapter 5, for the first time, we showed synthesis of spontaneous ion intercalated 2D nanosheets, accomplished by the RTO-CVD chamber as a robust platform to develop synthesis recipe for unknown materials. we demonstrated the synthesis of ultra-thin single crystal large area two-dimensional K-MnO_2 spontaneously intercalated with potassium ions via CVD, and this enabled new characterization tools to be employed in the study of the material unlike before. We investigated the structural and electrical properties of MnO_2. Among our findings, we found that charge in K-MnO_2 is dominantly carried by interlayer ions. Moreover, we showed that the moisture in the ambient enters the interlayer spacing and contribute to the charge transport. The interlayer ions can be mobilized via an in-plane external electric field, that results in a reversible phase transition from potassium intercalated structure to birnessite structure accompanied by an optical contrast change. In the case of excessive depletion of ions, a reversible phase transition to spinel is observed. It is possible to control these phase transitions via an external in-plane electric field. K-MnO_2 two-terminal devices with graphite contacts exhibit memristive properties, whose switching mechanisms is elucidated via real-time measurements. Finally, the intriguing ionic charge transport coupled with structural changes demonstrated potentially to be used in mimicking

the synaptic response for neuromorphic computing. Our results are scientifically rigorous thanks to our international collaboration in KAIST university, and will have significant impact in a wide range of fields including two-dimensional materials, MnO_2 based devices and neuromorphic computing.

Our results in chapter 5 also may shed some light on the energy storage and releasing properties of MnO_2. Manganese is an abundant material and cheaper alternative to many other transition metals. A 2D form of such material could be noteworthy in many applications including energy storage, catalysis, and water splitting. Moreover, similar materials with different intercalants such as Li, Na, Mg etc. can be synthesized in large areas using the similar methods employed in chapter 5 for catalysis and supercapacitor applications. As an example, by exchanging the salt type ()KI with NaI) and following the same growth recipe, we were able to obtain Na-MnO_2 ultra thin crystals. Figure 6.3 (a) shows the optical microscope image of a Na-MnO_2 crystal with its corresponding Raman response in (b), matching with the previously reported Na-birnessite Raman in the literature[217]. Theoretical structural prediction made by Mendoza-Cortes et al[179] suggests stability of various birnessite types (with different intercalated cations) down to the single layer. Indeed, our CVD procedure can be extended to the other birnessite types and open up the entry to the new class of layered 2D materials.

The outcome products of the RTO-CVD is not limited to the discussed materials in this thesis. As another example, high quality 2D MoO_2 crystals have been synthesized using MoO_3 precursor. Figure 6.4 shows the viability MoO_2 growth both on sapphire (a) and oxidized silicon (b) substrates. We were able to obtain ultra-thin crystals down to 3 nm thickness. This is an on-going research project for studying the thermal conductivity and young modulus of thin MoO_2 nanoplates as they are predicted to exhibit superb thermal and mechanical properties[218].

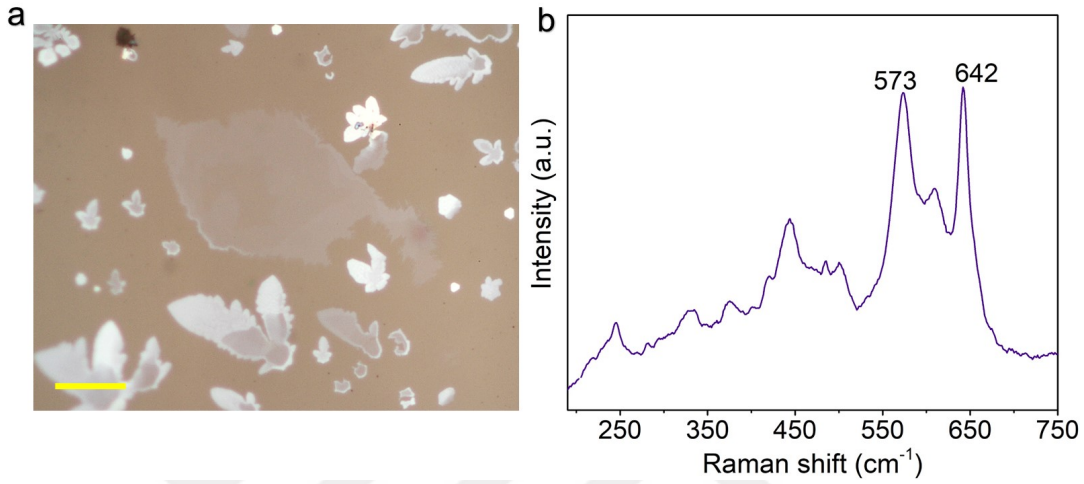

Figure 6.3: Na-MnO_2 crystals obtained using the same CVD approach. (a) Optical microscope image of the Na-MnO_2 crystals on sapphire substrate. The scale bar in 20 μm. (b) Raman spectrum taken from the as-grown crystals, matching with the reported N-birnessite in the literature.

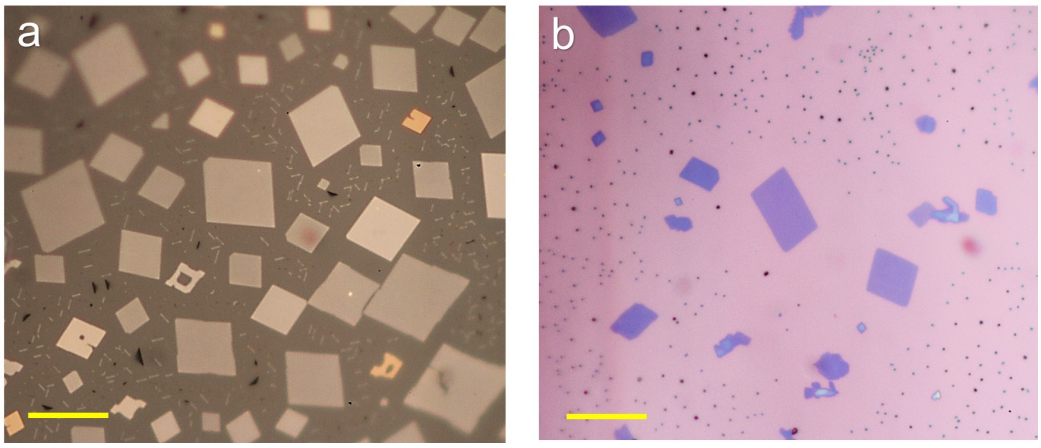

Figure 6.4: Ultra-thin single-crystal MoO_2 nanoplates synthesized via RTO-CVD method. (a) and (b) Optical microscope images taken from the as-grown MoO_2 crystals on sapphire and oxidized silicon substrates respectively. The scale bar in both images is 20 μm.

Bibliography

[1] K. S. Novoselov, A. K. Geim, S. V. Morozov, D. Jiang, Y. Zhang, S. V. Dubonos, I. V. Grigorieva, and A. A. Firsov, "Electric field effect in atomically thin carbon films," *science*, vol. 306, no. 5696, pp. 666–669, 2004.

[2] F. Bonaccorso, Z. Sun, T. Hasan, and A. Ferrari, "Graphene photonics and optoelectronics," *Nature photonics*, vol. 4, no. 9, p. 611, 2010.

[3] D. A. Brownson, D. K. Kampouris, and C. E. Banks, "An overview of graphene in energy production and storage applications," *Journal of Power Sources*, vol. 196, no. 11, pp. 4873–4885, 2011.

[4] M. Pumera, "Graphene in biosensing," *Materials today*, vol. 14, no. 7-8, pp. 308–315, 2011.

[5] K. Zhang, Y. Feng, F. Wang, Z. Yang, and J. Wang, "Two dimensional hexagonal boron nitride (2d-hbn): synthesis, properties and applications," *Journal of Materials Chemistry C*, vol. 5, no. 46, pp. 11992–12022, 2017.

[6] S. Zhao, T. Hotta, T. Koretsune, K. Watanabe, T. Taniguchi, K. Sugawara, T. Takahashi, H. Shinohara, and R. Kitaura, "Two-dimensional metallic nbs2: growth, optical identification and transport properties," *2D Materials*, vol. 3, no. 2, p. 025027, 2016.

[7] K. F. Mak, C. Lee, J. Hone, J. Shan, and T. F. Heinz, "Atomically thin mos 2: a new direct-gap semiconductor," *Physical review letters*, vol. 105, no. 13, p. 136805, 2010.

[8] A. K. Geim and I. V. Grigorieva, "Van der waals heterostructures," *Nature*, vol. 499, no. 7459, pp. 419–425, 2013.

[9] J. N. Coleman, M. Lotya, A. O'Neill, S. D. Bergin, P. J. King, U. Khan, K. Young, A. Gaucher, S. De, R. J. Smith, *et al.*, "Two-dimensional nanosheets produced by liquid exfoliation of layered materials," *Science*, vol. 331, no. 6017, pp. 568–571, 2011.

[10] Q. Zhang, L. Mei, X. Cao, Y. Tang, and Z. Zeng, "Intercalation and exfoliation chemistry of transition metal dichalcogenides," *Journal of Materials Chemistry A*, 2020.

[11] F. Bonaccorso and Z. Sun, "Solution processing of graphene, topological insulators and other 2d crystals for ultrafast photonics," *Opt. Mater. Express*, vol. 4, pp. 63–78, Jan 2014.

[12] Z. Cai, B. Liu, X. Zou, and H.-M. Cheng, "Chemical vapor deposition growth and applications of two-dimensional materials and their heterostructures," *Chemical reviews*, vol. 118, no. 13, pp. 6091–6133, 2018.

[13] M. Chhowalla, H. S. Shin, G. Eda, L.-J. Li, K. P. Loh, and H. Zhang, "The chemistry of two-dimensional layered transition metal dichalcogenide nanosheets," *Nature chemistry*, vol. 5, no. 4, pp. 263–275, 2013.

[14] S. J. McDonnell and R. M. Wallace, "Atomically-thin layered films for device applications based upon 2d tmdc materials," *Thin Solid Films*, vol. 616, pp. 482–501, 2016.

[15] Z. Li and S. L. Wong, "Functionalization of 2d transition metal dichalcogenides for biomedical applications," *Materials Science and Engineering: C*, vol. 70, pp. 1095–1106, 2017.

[16] X. Li, W. Cai, J. An, S. Kim, J. Nah, D. Yang, R. Piner, A. Velamakanni, I. Jung, E. Tutuc, *et al.*, "Large-area synthesis of high-quality and uniform graphene films on copper foils," *science*, vol. 324, no. 5932, pp. 1312–1314, 2009.

[17] J. Yu, J. Li, W. Zhang, and H. Chang, "Synthesis of high quality two-dimensional materials via chemical vapor deposition," *Chemical science*, vol. 6, no. 12, pp. 6705–6716, 2015.

[18] L. Fei, S. Lei, W.-B. Zhang, W. Lu, Z. Lin, C. H. Lam, Y. Chai, and Y. Wang, "Direct tem observations of growth mechanisms of two-dimensional mos 2 flakes," *Nature communications*, vol. 7, no. 1, pp. 1–7, 2016.

[19] C. B. López-Posadas, Y. Wei, W. Shen, D. Kahr, M. Hohage, and L. Sun, "Direct observation of the cvd growth of monolayer mos2 using in situ optical spectroscopy," *Beilstein journal of nanotechnology*, vol. 10, no. 1, pp. 557–564, 2019.

[20] Z. Liu, Y.-C. Lin, C.-C. Lu, C.-H. Yeh, P.-W. Chiu, S. Iijima, and K. Suenaga, "In situ observation of step-edge in-plane growth of graphene in a stem," *Nature communications*, vol. 5, no. 1, pp. 1–7, 2014.

[21] Z.-J. Wang, G. Weinberg, Q. Zhang, T. Lunkenbein, A. Klein-Hoffmann, M. Kurnatowska, M. Plodinec, Q. Li, L. Chi, R. Schloegl, *et al.*, "Direct observation of graphene growth and associated copper substrate dynamics by in situ scanning electron microscopy," *ACS nano*, vol. 9, no. 2, pp. 1506–1519, 2015.

[22] S. Li, S. Wang, D.-M. Tang, W. Zhao, H. Xu, L. Chu, Y. Bando, D. Golberg, and G. Eda, "Halide-assisted atmospheric pressure growth of large wse2 and ws2 monolayer crystals," *Applied Materials Today*, vol. 1, no. 1, pp. 60–66, 2015.

[23] H. Wang, X. Huang, J. Lin, J. Cui, Y. Chen, C. Zhu, F. Liu, Q. Zeng, J. Zhou, P. Yu, *et al.*, "High-quality monolayer superconductor nbse 2 grown by chemical vapour deposition," *Nature communications*, vol. 8, no. 1, pp. 1–8, 2017.

[24] H. Wang, Y. Chen, M. Duchamp, Q. Zeng, X. Wang, S. H. Tsang, H. Li, L. Jing, T. Yu, E. H. T. Teo, *et al.*, "Large-area atomic layers of the

charge-density-wave conductor tise2," *Advanced Materials*, vol. 30, no. 8, p. 1704382, 2018.

[25] C. Sikalidis, *Advances in ceramics: synthesis and characterization, processing and specific applications*. BoD–Books on Demand, 2011.

[26] J. Zhou, J. Lin, X. Huang, Y. Zhou, Y. Chen, J. Xia, H. Wang, Y. Xie, H. Yu, J. Lei, *et al.*, "A library of atomically thin metal chalcogenides," *Nature*, vol. 556, no. 7701, pp. 355–359, 2018.

[27] Y. Nie, C. Liang, K. Zhang, R. Zhao, S. M. Eichfeld, P.-R. Cha, L. Colombo, J. A. Robinson, R. M. Wallace, and K. Cho, "First principles kinetic monte carlo study on the growth patterns of wse2 monolayer," *2D Materials*, vol. 3, no. 2, p. 025029, 2016.

[28] S. Li, Y.-C. Lin, W. Zhao, J. Wu, Z. Wang, Z. Hu, Y. Shen, D.-M. Tang, J. Wang, Q. Zhang, *et al.*, "Vapour–liquid–solid growth of monolayer mos 2 nanoribbons," *Nature materials*, vol. 17, no. 6, pp. 535–542, 2018.

[29] H. R. Rasouli, N. Mehmood, O. Çakıroğlu, and T. S. Kasırga, "Real time optical observation and control of atomically thin transition metal dichalcogenide synthesis," *Nanoscale*, vol. 11, no. 15, pp. 7317–7323, 2019.

[30] S. Wang, Y. Rong, Y. Fan, M. Pacios, H. Bhaskaran, K. He, and J. H. Warner, "Shape evolution of monolayer mos2 crystals grown by chemical vapor deposition," *Chemistry of Materials*, vol. 26, no. 22, pp. 6371–6379, 2014.

[31] H. Suzuki, T. Kaneko, Y. Shibuta, M. Ohno, Y. Maekawa, and T. Kato, "Wafer-scale fabrication and growth dynamics of suspended graphene nanoribbon arrays," *Nature communications*, vol. 7, no. 1, pp. 1–10, 2016.

[32] Q. Yan, Y. Wang, Y. Jin, and Y. Chen, "Methane oxidative coupling over na 2 wo 4/sio 2," *Catalysis letters*, vol. 13, no. 3, pp. 221–228, 1992.

[33] G. Halada and C. Clayton, "Comparison of mo–n and w–n synergism during passivation of stainless steel through x-ray photoelectron spectroscopy

and electrochemical analysis," *Journal of Vacuum Science & Technology A: Vacuum, Surfaces, and Films*, vol. 11, no. 4, pp. 2342–2347, 1993.

[34] C. L. Lima, G. Saraiva, P. Freire, M. Maczka, W. Paraguassu, F. De Sousa, and J. Mendes Filho, "Temperature-induced phase transformations in na2wo4 and na2moo4 crystals," *Journal of Raman Spectroscopy*, vol. 42, no. 4, pp. 799–802, 2011.

[35] L. L. CHANG and S. SACHDEV, "Alkali tungstates: Stability relations in the systems a2o wo3-wo3," *Journal of the American Ceramic Society*, vol. 58, no. 7-8, pp. 267–270, 1975.

[36] Y. Zhang, Y. Zhang, Q. Ji, J. Ju, H. Yuan, J. Shi, T. Gao, D. Ma, M. Liu, Y. Chen, *et al.*, "Controlled growth of high-quality monolayer ws2 layers on sapphire and imaging its grain boundary," *ACS nano*, vol. 7, no. 10, pp. 8963–8971, 2013.

[37] Y. Li, F. Wang, D. Tang, J. Wei, Y. Li, Y. Xing, and K. Zhang, "Controlled synthesis of highly crystalline cvd-derived monolayer mose2 and shape evolution mechanism," *Materials Letters*, vol. 216, pp. 261–264, 2018.

[38] Y. Sheng, H. Tan, X. Wang, and J. H. Warner, "Hydrogen addition for centimeter-sized monolayer tungsten disulfide continuous films by ambient pressure chemical vapor deposition," *Chemistry of Materials*, vol. 29, no. 11, pp. 4904–4911, 2017.

[39] H. Wang, D. Zhu, F. Jiang, P. Zhao, H. Wang, Z. Zhang, X. Chen, and C. Jin, "Revealing the microscopic cvd growth mechanism of mose2 and the role of hydrogen gas during the growth procedure," *Nanotechnology*, vol. 29, no. 31, p. 314001, 2018.

[40] Y. Gong, G. Ye, S. Lei, G. Shi, Y. He, J. Lin, X. Zhang, R. Vajtai, S. T. Pantelides, W. Zhou, *et al.*, "Synthesis of millimeter-scale transition metal dichalcogenides single crystals," *Advanced Functional Materials*, vol. 26, no. 12, pp. 2009–2015, 2016.

[41] P. Dickens and M. Whittingham, "The tungsten bronzes and related compounds," *Quarterly Reviews, Chemical Society*, vol. 22, no. 1, pp. 30–44, 1968.

[42] Y. Xue, Y. Zhang, and P. Zhang, "Theory of the color change of na x wo 3 as a function of na-charge doping," *Physical Review B*, vol. 79, no. 20, p. 205113, 2009.

[43] J.-N. Chazalviel, M. Campagna, G. Wertheim, and H. Shanks, "Final-state effects in the x-ray photoelectron spectra of cubic sodium-tungsten bronzes," *Physical Review B*, vol. 16, no. 2, p. 697, 1977.

[44] J.-S. Lee, H. Liu, G.-D. Peng, and Y. Tseng, "Facile synthesis and structure characterization of hexagonal tungsten bronzes crystals," *Journal of Crystal Growth*, vol. 465, pp. 27–33, 2017.

[45] J. Hoffmann and M. King, "Selenium and selenium compounds," *Kirk-Othmer Encyclopedia of Chemical Technology*, 2000.

[46] H. J. Reich and R. J. Hondal, "Why nature chose selenium," *ACS chemical biology*, vol. 11, no. 4, pp. 821–841, 2016.

[47] E. E. Battin and J. L. Brumaghim, "Antioxidant activity of sulfur and selenium: a review of reactive oxygen species scavenging, glutathione peroxidase, and metal-binding antioxidant mechanisms," *Cell biochemistry and biophysics*, vol. 55, no. 1, pp. 1–23, 2009.

[48] Y. Saito and T. Sakiyama, "Kinetic effect on 2d dendritic growth," *Journal of crystal growth*, vol. 128, no. 1-4, pp. 224–228, 1993.

[49] B. Liu, M. Fathi, L. Chen, A. Abbas, Y. Ma, and C. Zhou, "Chemical vapor deposition growth of monolayer wse2 with tunable device characteristics and growth mechanism study," *ACS nano*, vol. 9, no. 6, pp. 6119–6127, 2015.

[50] W. Shi, M.-L. Lin, Q.-H. Tan, X.-F. Qiao, J. Zhang, and P.-H. Tan, "Raman and photoluminescence spectra of two-dimensional nanocrystallites of monolayer ws2 and wse2," *2D Materials*, vol. 3, no. 2, p. 025016, 2016.

[51] J.-K. Huang, J. Pu, C.-L. Hsu, M.-H. Chiu, Z.-Y. Juang, Y.-H. Chang, W.-H. Chang, Y. Iwasa, T. Takenobu, and L.-J. Li, "Large-area synthesis of highly crystalline wse2 monolayers and device applications," *ACS nano*, vol. 8, no. 1, pp. 923–930, 2014.

[52] S. M. Eichfeld, L. Hossain, Y.-C. Lin, A. F. Piasecki, B. Kupp, A. G. Birdwell, R. A. Burke, N. Lu, X. Peng, J. Li, *et al.*, "Highly scalable, atomically thin wse2 grown via metal–organic chemical vapor deposition," *ACS nano*, vol. 9, no. 2, pp. 2080–2087, 2015.

[53] S. Lippert, L. M. Schneider, D. Renaud, K. N. Kang, O. Ajayi, J. Kuhnert, M.-U. Halbich, O. M. Abdulmunem, X. Lin, K. Hassoon, *et al.*, "Influence of the substrate material on the optical properties of tungsten diselenide monolayers," *2D Materials*, vol. 4, no. 2, p. 025045, 2017.

[54] H. Zhou, C. Wang, J. C. Shaw, R. Cheng, Y. Chen, X. Huang, Y. Liu, N. O. Weiss, Z. Lin, Y. Huang, *et al.*, "Large area growth and electrical properties of p-type wse2 atomic layers," *Nano letters*, vol. 15, no. 1, pp. 709–713, 2015.

[55] S. Li, Y.-C. Lin, X.-Y. Liu, Z. Hu, J. Wu, H. Nakajima, S. Liu, T. Okazaki, W. Chen, T. Minari, *et al.*, "Wafer-scale and deterministic patterned growth of monolayer mos 2 via vapor–liquid–solid method," *Nanoscale*, vol. 11, no. 34, pp. 16122–16129, 2019.

[56] J. C. Shaw, H. Zhou, Y. Chen, N. O. Weiss, Y. Liu, Y. Huang, and X. Duan, "Chemical vapor deposition growth of monolayer mose 2 nanosheets," *Nano Research*, vol. 7, no. 4, pp. 511–517, 2014.

[57] Y.-H. Chang, W. Zhang, Y. Zhu, Y. Han, J. Pu, J.-K. Chang, W.-T. Hsu, J.-K. Huang, C.-L. Hsu, M.-H. Chiu, *et al.*, "Monolayer mose2 grown by chemical vapor deposition for fast photodetection," *ACS nano*, vol. 8, no. 8, pp. 8582–8590, 2014.

[58] N. Bahlawane and D. Lenoble, "Vanadium oxide compounds: structure, properties, and growth from the gas phase," *Chemical Vapor Deposition*, vol. 20, no. 7-8-9, pp. 299–311, 2014.

[59] F. Morin, "Oxides which show a metal-to-insulator transition at the neel temperature," *Physical review letters*, vol. 3, no. 1, p. 34, 1959.

[60] H. Harashina, K. Kodama, S.-i. Shamoto, S. Taniguchi, T. Nishikawa, M. Sato, K. Kakurai, and M. Nishi, "Spin structure of s= 1/2 quantum spin system cav_3o_7," *Journal of the Physical Society of Japan*, vol. 65, no. 6, pp. 1570–1573, 1996.

[61] L. Krusin-Elbaum, D. Newns, H. Zeng, V. Derycke, J. Sun, and R. Sandstrom, "Room-temperature ferromagnetic nanotubes controlled by electron or hole doping," *Nature*, vol. 431, no. 7009, pp. 672–676, 2004.

[62] T. Yamauchi, Y. Ueda, and N. Môri, "Pressure-induced superconductivity in β- n a 0.33 v 2 o 5 beyond charge ordering," *Physical review letters*, vol. 89, no. 5, p. 057002, 2002.

[63] D. Ruzmetov, S. D. Senanayake, V. Narayanamurti, and S. Ramanathan, "Correlation between metal-insulator transition characteristics and electronic structure changes in vanadium oxide thin films," *Physical Review B*, vol. 77, no. 19, p. 195442, 2008.

[64] A. Pergament, G. Stefanovich, and A. Velichko, "Oxide electronics and vanadium dioxide perspective: A review," *Journal on Selected Topics in Nano Electronics and Computing*, vol. 1, no. 1, pp. 24–43, 2013.

[65] E. Dagotto, "Complexity in strongly correlated electronic systems," *Science*, vol. 309, no. 5732, pp. 257–262, 2005.

[66] A. Pustogow, A. S. McLeod, Y. Saito, D. N. Basov, and M. Dressel, "Internal strain tunes electronic correlations on the nanoscale," *Science advances*, vol. 4, no. 12, p. eaau9123, 2018.

[67] B. S. Guiton, Q. Gu, A. L. Prieto, M. S. Gudiksen, and H. Park, "Single-crystalline vanadium dioxide nanowires with rectangular cross sections," *Journal of the American Chemical Society*, vol. 127, no. 2, pp. 498–499, 2005.

[68] J. Wei, Z. Wang, W. Chen, and D. H. Cobden, "New aspects of the metal–insulator transition in single-domain vanadium dioxide nanobeams," *Nature nanotechnology*, vol. 4, no. 7, pp. 420–424, 2009.

[69] V. Andreev, F. Chudnovskiy, J. Honig, and P. Metcalf, "Electrical conductivity in the antiferromagnetic insulating phase of v 2 o 3," *Physical Review B*, vol. 70, no. 23, p. 235124, 2004.

[70] M. M. Fadlelmula, E. C. Surmeli, M. Ramezani, and T. S. Kasırga, "Effects of thickness on the metal–insulator transition in free-standing vanadium dioxide nanocrystals," *Nano Letters*, vol. 17, no. 3, pp. 1762–1767, 2017.

[71] A. D. Raj, P. S. Kumar, Q. Yang, and D. Mangalaraj, "Synthesis and gas sensors behavior of surfactants free v2o5 nanostructure by using a simple precipitation method," *Physica E: Low-dimensional Systems and Nanostructures*, vol. 44, no. 7-8, pp. 1490–1494, 2012.

[72] M. Shandilya, R. Rai, and J. Singh, "hydrothermal technology for smart materials," *Advances in Applied Ceramics*, vol. 115, no. 6, pp. 354–376, 2016.

[73] W. Zeng, W. Chen, Z. Li, H. Zhang, and T. Li, "Rapid and sensitive ethanol sensor based on hollow au/v2o5 nanotubes via emulsion-electrospinning route," *Materials Research Bulletin*, vol. 65, pp. 157–162, 2015.

[74] E. A. Olivetti, J. H. Kim, D. R. Sadoway, A. Asatekin, and A. M. Mayes, "Sol- gel synthesis of vanadium oxide within a block copolymer matrix," *Chemistry of materials*, vol. 18, no. 12, pp. 2828–2833, 2006.

[75] Q. Su, C. Huang, Y. Wang, Y. Fan, B. Lu, W. Lan, Y. Wang, and X. Liu, "Formation of vanadium oxides with various morphologies by chemical vapor deposition," *Journal of alloys and compounds*, vol. 475, no. 1-2, pp. 518–523, 2009.

[76] T. D. Vu, Z. Chen, X. Zeng, M. Jiang, S. Liu, Y. Gao, and Y. Long, "Physical vapour deposition of vanadium dioxide for thermochromic smart window applications," *Journal of Materials Chemistry C*, vol. 7, no. 8, pp. 2121–2145, 2019.

[77] C. Ramana, R. Smith, O. Hussain, and C. Julien, "On the growth mechanism of pulsed-laser deposited vanadium oxide thin films," *Materials Science and Engineering: B*, vol. 111, no. 2-3, pp. 218–225, 2004.

[78] T. Singh, S. Wang, N. Aslam, H. Zhang, S. Hoffmann-Eifert, and S. Mathur, "Atomic layer deposition of transparent vox thin films for resistive switching applications," *Chemical vapor deposition*, vol. 20, no. 7-8-9, pp. 291–297, 2014.

[79] S. Chen, H. Ma, S. Wang, N. Shen, J. Xiao, H. Zhou, X. Zhao, Y. Li, and X. Yi, "Vanadium oxide thin films deposited on silicon dioxide buffer layers by magnetron sputtering," *Thin Solid Films*, vol. 497, no. 1-2, pp. 267–269, 2006.

[80] T. S. Kasirga, *Experiments on a strongly correlated material: photoresponse, phase diagram and hydrogen doping of vanadium dioxide*. PhD thesis, University of Washington, Jan. 2013.

[81] J. Feinleib and W. Paul, "Semiconductor-to-metal transition in v 2 o 3," *Physical Review*, vol. 155, no. 3, p. 841, 1967.

[82] G. Thomas, D. Rapkine, S. Carter, A. Millis, T. Rosenbaum, P. Metcalf, and J. Honig, "Observation of the gap and kinetic energy in a correlated insulator," *Physical review letters*, vol. 73, no. 11, p. 1529, 1994.

[83] P. Limelette, A. Georges, D. Jérome, P. Wzietek, P. Metcalf, and J. Honig, "Universality and critical behavior at the mott transition," *Science*, vol. 302, no. 5642, pp. 89–92, 2003.

[84] J. S. Brockman, L. Gao, B. Hughes, C. T. Rettner, M. G. Samant, K. P. Roche, and S. S. Parkin, "Subnanosecond incubation times for electric-field-induced metallization of a correlated electron oxide," *Nature nanotechnology*, vol. 9, no. 6, p. 453, 2014.

[85] G. F. Schneider, V. E. Calado, H. Zandbergen, L. M. Vandersypen, and C. Dekker, "Wedging transfer of nanostructures," *Nano letters*, vol. 10, no. 5, pp. 1912–1916, 2010.

[86] R. Baddour-Hadjean, A. Boudaoud, S. Bach, N. Emery, and J.-P. Pereira-Ramos, "A comparative insight of potassium vanadates as positive electrode materials for li batteries: influence of the long-range and local structure," *Inorganic chemistry*, vol. 53, no. 3, pp. 1764–1772, 2014.

[87] G. Xu, X. Wang, X. Chen, and L. Jiao, "Facile synthesis and phase transition of v 2 o 3 nanobelts," *RSC advances*, vol. 5, no. 23, pp. 17782–17785, 2015.

[88] M. Foguel and R. Grajower, "Flux growth of v2o3 single crystals by reduction of v2o5 in a graphite crucible," *Journal of Crystal Growth*, vol. 11, no. 3, pp. 280–282, 1971.

[89] L. Deng, X. Niu, G. Ma, Z. Yang, L. Zeng, Y. Zhu, and L. Guo, "Layered potassium vanadate k0. 5v2o5 as a cathode material for nonaqueous potassium ion batteries," *Advanced Functional Materials*, vol. 28, no. 49, p. 1800670, 2018.

[90] H. R. Rasouli, N. Mehmood, O. Çakıroğlu, E. C. Sürmeli, and T. S. Kasırga, "Synthesis of v 2 o 3 nanoplates for the exploration of the correlated supercritical state," *Physical Review B*, vol. 100, no. 16, p. 161107, 2019.

[91] M. Tachibana, "Mechanisms of crystal growth from fluxed solutions," in *Beginner's Guide to Flux Crystal Growth*, pp. 23–41, Springer, 2017.

[92] A. P. Balan, S. Radhakrishnan, C. F. Woellner, S. K. Sinha, L. Deng, C. de los Reyes, B. M. Rao, M. Paulose, R. Neupane, A. Apte, *et al.*, "Exfoliation of a non-van der waals material from iron ore hematite," *Nature nanotechnology*, vol. 13, no. 7, pp. 602–609, 2018.

[93] A. Puthirath Balan, S. Radhakrishnan, R. Kumar, R. Neupane, S. K. Sinha, L. Deng, C. A. de los Reyes, A. Apte, B. M. Rao, M. Paulose, *et al.*, "A non-van der waals two-dimensional material from natural titanium mineral ore ilmenite," *Chemistry of Materials*, vol. 30, no. 17, pp. 5923–5931, 2018.

[94] G. Sawatzky and D. Post, "X-ray photoelectron and auger spectroscopy study of some vanadium oxides," *Physical Review B*, vol. 20, no. 4, p. 1546, 1979.

[95] G. Silversmit, D. Depla, H. Poelman, G. B. Marin, and R. De Gryse, "Determination of the v2p xps binding energies for different vanadium oxidation states (v5+ to v0+)," *Journal of Electron Spectroscopy and Related Phenomena*, vol. 135, no. 2-3, pp. 167–175, 2004.

[96] D. McWhan and J. Remeika, "Metal-insulator transition in (v 1- x cr x) 2 o 3," *Physical Review B*, vol. 2, no. 9, p. 3734, 1970.

[97] E. Hryha, E. Rutqvist, and L. Nyborg, "Stoichiometric vanadium oxides studied by xps," *Surface and interface analysis*, vol. 44, no. 8, pp. 1022–1025, 2012.

[98] H. Nohira, W. Tsai, W. Besling, E. Young, J. Pétry, T. Conard, W. Vandervorst, S. De Gendt, M. Heyns, J. Maes, *et al.*, "Characterization of alcvd-al2o3 and zro2 layer using x-ray photoelectron spectroscopy," *Journal of non-crystalline solids*, vol. 303, no. 1, pp. 83–87, 2002.

[99] P. Dernier and M. Marezio, "Crystal structure of the low-temperature antiferromagnetic phase of v 2 o 3," *Physical Review B*, vol. 2, no. 9, p. 3771, 1970.

[100] P. Dernier, "The crystal structure of v2o3 and (v0. 962cr0. 0382) 2o3 near the metal-insulator transition," *Journal of Physics and chemistry of solids*, vol. 31, no. 11, pp. 2569–2575, 1970.

[101] M. I. B. Utama, F. J. Belarre, C. Magen, B. Peng, J. Arbiol, and Q. Xiong, "Incommensurate van der waals epitaxy of nanowire arrays: a case study with zno on muscovite mica substrates," *Nano letters*, vol. 12, no. 4, pp. 2146–2152, 2012.

[102] B. Allimi, S. Alpay, C. Xie, B. Wells, J. Budnick, and D. Pease, "Resistivity of v 2 o 3 thin films deposited on a-plane (110) and c-plane (001) sapphire by pulsed laser deposition," *Applied Physics Letters*, vol. 92, no. 20, p. 202105, 2008.

[103] D. McWhan, A. Menth, J. Remeika, W. Brinkman, and T. Rice, "Metal-insulator transitions in pure and doped v 2 o 3," *Physical Review B*, vol. 7, no. 5, p. 1920, 1973.

[104] P. Hansmann, A. Toschi, G. Sangiovanni, T. Saha-Dasgupta, S. Lupi, M. Marsi, and K. Held, "Mott–hubbard transition in v2o3 revisited," *physica status solidi (b)*, vol. 250, no. 7, pp. 1251–1264, 2013.

[105] F. Lechermann, N. Bernstein, I. Mazin, and R. Valentí, "Uncovering the mechanism of the impurity-selective mott transition in paramagnetic v 2 o 3," *Physical review letters*, vol. 121, no. 10, p. 106401, 2018.

[106] C. Tatsuyama and H. Fan, "Raman scattering and phase transitions in v 2 o 3 and (v 1- x cr x) 2 o 3," *Physical Review B*, vol. 21, no. 7, p. 2977, 1980.

[107] N. Kuroda and H. Fan, "Raman scattering and phase transitions of v 2 o 3," *Physical Review B*, vol. 16, no. 11, p. 5003, 1977.

[108] L. Eckert and R. Bradt, "Thermal expansion of corundum structure ti2o3 and v2o3," *Journal of Applied Physics*, vol. 44, no. 8, pp. 3470–3472, 1973.

[109] R. Gaillac, P. Pullumbi, and F.-X. Coudert, "Elate: an open-source online application for analysis and visualization of elastic tensors," *Journal of Physics: Condensed Matter*, vol. 28, no. 27, p. 275201, 2016.

[110] Y. Sato and S.-i. Akimoto, "Hydrostatic compression of four corundum-type compounds: α-al2o3, v2o3, cr2o3, and α-fe2o3," *Journal of Applied Physics*, vol. 50, no. 8, pp. 5285–5291, 1979.

[111] H. J. Zeiger, "Unified model of the insulator-metal transition in ti 2 o 3 and the high-temperature transitions in v 2 o 3," *Physical Review B*, vol. 11, no. 12, p. 5132, 1975.

[112] A. Okamoto, Y. Fujita, and C. Tatsuyama, "Raman study on the high temperature transition in v2o3," *Journal of the Physical Society of Japan*, vol. 52, no. 1, pp. 312–317, 1983.

[113] H. Guo, M. Khan, C. Cheng, W. Fan, C. Dames, J. Wu, and A. Minor, "Vanadium dioxide nanowire-based microthermometer for quantitative evaluation of electron beam heating," *Nature communications*, vol. 5, no. 1, pp. 1–5, 2014.

[114] J. Wu, Q. Gu, B. S. Guiton, N. P. De Leon, L. Ouyang, and H. Park, "Strain-induced self organization of metal- insulator domains in single-crystalline vo2 nanobeams," *Nano letters*, vol. 6, no. 10, pp. 2313–2317, 2006.

[115] H. Kuwamoto, H. Keer, J. Keem, S. Shivashankar, L. Van Zandt, and J. Honig, "Electrical transitions in pure and doped v2o3," *Le Journal de Physique Colloques*, vol. 37, no. C4, pp. C4–35, 1976.

[116] H. Kuwamoto, J. Honig, and J. Appel, "Electrical properties of the (v 1- x cr x) 2 o 3 system," *Physical Review B*, vol. 22, no. 6, p. 2626, 1980.

[117] L. O. M. Chua, "The missing circuit element. circuit theory," *IEEE Trans*, vol. 18, pp. 507–519, 1971.

[118] D. B. Strukov, G. S. Snider, D. R. Stewart, and R. S. Williams, "How we found the missing memristor," *Nature*, vol. 453, pp. 80–83, 2008.

[119] S. Hu, S. Wu, W. Jia, Q. Yu, L. Deng, Y. Q. Fu, Y. Liu, and T. P. Chen, "Review of nanostructured resistive switching memristor and its applications," *Nanoscience and Nanotechnology Letters*, vol. 6, no. 9, pp. 729–757, 2014.

[120] V. K. Sangwan, D. Jariwala, I. S. Kim, K.-S. Chen, T. J. Marks, L. J. Lauhon, and M. C. Hersam, "Gate-tunable memristive phenomena mediated by grain boundaries in single-layer mos 2," *Nature nanotechnology*, vol. 10, no. 5, pp. 403–406, 2015.

[121] A. J. Mannix, B. Kiraly, M. C. Hersam, and N. P. Guisinger, "Synthesis and chemistry of elemental 2d materials," *Nature Reviews Chemistry*, vol. 1, no. 2, pp. 1–14, 2017.

[122] S. J. Kim, K. Choi, B. Lee, Y. Kim, and B. H. Hong, "Materials for flexible, stretchable electronics: graphene and 2d materials," *Annual Review of Materials Research*, vol. 45, pp. 63–84, 2015.

[123] J. Deng, D. Deng, and X. Bao, "Robust catalysis on 2d materials encapsulating metals: concept, application, and perspective," *Advanced Materials*, vol. 29, no. 43, p. 1606967, 2017.

[124] H. Song, J. Liu, B. Liu, J. Wu, H.-M. Cheng, and F. Kang, "Two-dimensional materials for thermal management applications," *Joule*, vol. 2, no. 3, pp. 442–463, 2018.

[125] P. J. Jeon, J. S. Kim, J. Y. Lim, Y. Cho, A. Pezeshki, H. S. Lee, S. Yu, S.-W. Min, and S. Im, "Low power consumption complementary inverters with n-mos2 and p-wse2 dichalcogenide nanosheets on glass for logic and light-emitting diode circuits," *ACS applied materials & interfaces*, vol. 7, no. 40, pp. 22333–22340, 2015.

[126] R. Tetzlaff, *Memristors and memristive systems*. Springer, 2013.

[127] X. Yan, Q. Zhao, A. P. Chen, J. Zhao, Z. Zhou, J. Wang, H. Wang, L. Zhang, X. Li, Z. Xiao, *et al.*, "Vacancy-induced synaptic behavior in 2d ws2 nanosheet–based memristor for low-power neuromorphic computing," *Small*, vol. 15, no. 24, p. 1901423, 2019.

[128] L. Wang, W. Liao, S. L. Wong, Z. G. Yu, S. Li, Y.-F. Lim, X. Feng, W. C. Tan, X. Huang, L. Chen, *et al.*, "Artificial synapses based on multiterminal memtransistors for neuromorphic application," *Advanced Functional Materials*, vol. 29, no. 25, p. 1901106, 2019.

[129] P. Cheng, K. Sun, and Y. H. Hu, "Memristive behavior and ideal memristor of 1t phase mos2 nanosheets," *Nano letters*, vol. 16, no. 1, pp. 572–576, 2016.

[130] X. Zhu, D. Li, X. Liang, and W. D. Lu, "Ionic modulation and ionic coupling effects in mos 2 devices for neuromorphic computing," *Nature materials*, vol. 18, no. 2, pp. 141–148, 2019.

[131] M. Yoshida, R. Suzuki, Y. Zhang, M. Nakano, and Y. Iwasa, "Memristive phase switching in two-dimensional 1t-tas2 crystals," *Science advances*, vol. 1, no. 9, p. e1500606, 2015.

[132] Q. A. Vu, H. Kim, V. L. Nguyen, U. Y. Won, S. Adhikari, K. Kim, Y. H. Lee, and W. J. Yu, "A high-on/off-ratio floating-gate memristor array on a flexible substrate via cvd-grown large-area 2d layer stacking," *Advanced Materials*, vol. 29, no. 44, p. 1703363, 2017.

[133] W. Lv, H. Wang, L. Jia, X. Tang, C. Lin, L. Yuwen, L. Wang, W. Huang, and R. Chen, "Tunable nonvolatile memory behaviors of pcbm–mos2 2d nanocomposites through surface deposition ratio control," *ACS applied materials & interfaces*, vol. 10, no. 7, pp. 6552–6559, 2018.

[134] F. Wu, S. Si, P. Cao, W. Wei, X. Zhao, T. Shi, X. Zhang, J. Ma, R. Cao, L. Liao, *et al.*, "Interface engineering via mos2 insertion layer for improving resistive switching of conductive-bridging random access memory," *Advanced Electronic Materials*, vol. 5, no. 4, p. 1800747, 2019.

[135] K. Zhu, X. Liang, B. Yuan, M. A. Villena, C. Wen, T. Wang, S. Chen, F. Hui, Y. Shi, and M. Lanza, "Graphene–boron nitride–graphene cross-point memristors with three stable resistive states," *ACS applied materials & interfaces*, vol. 11, no. 41, pp. 37999–38005, 2019.

[136] S. M. Shinde, G. Kalita, and M. Tanemura, "Fabrication of poly (methyl methacrylate)-mos2/graphene heterostructure for memory device application," *Journal of Applied Physics*, vol. 116, no. 21, p. 214306, 2014.

[137] A. A. Bessonov, M. N. Kirikova, D. I. Petukhov, M. Allen, T. Ryhänen, and M. J. Bailey, "Layered memristive and memcapacitive switches for printable electronics," *Nature materials*, vol. 14, no. 2, pp. 199–204, 2015.

[138] M. Wang, S. Cai, C. Pan, C. Wang, X. Lian, Y. Zhuo, K. Xu, T. Cao, X. Pan, B. Wang, *et al.*, "Robust memristors based on layered two-dimensional materials," *Nature Electronics*, vol. 1, no. 2, pp. 130–136, 2018.

[139] B. Wang, H. Luo, X. Wang, E. Wang, Y. Sun, Y.-C. Tsai, H. Zhu, P. Liu, K. Jiang, and K. Liu, "Bifunctional nbs2-based asymmetric heterostructure for lateral and vertical electronic devices," *ACS nano*, vol. 14, no. 1, pp. 175–184, 2019.

[140] M. Zhao, R. Li, and J. Xue, "Atomic bridge memristor based on silver and two-dimensional gese," *AIP Advances*, vol. 10, no. 4, p. 045003, 2020.

[141] J. Wan, S. D. Lacey, J. Dai, W. Bao, M. S. Fuhrer, and L. Hu, "Tuning two-dimensional nanomaterials by intercalation: materials, properties and applications," *Chemical Society Reviews*, vol. 45, no. 24, pp. 6742–6765, 2016.

[142] J. Zhang, A. Yang, X. Wu, J. van de Groep, P. Tang, S. Li, B. Liu, F. Shi, J. Wan, Q. Li, *et al.*, "Reversible and selective ion intercalation through the top surface of few-layer mos 2," *Nature communications*, vol. 9, no. 1, pp. 1–9, 2018.

[143] J. Park, J.-S. Kim, J.-W. Park, T.-H. Nam, K.-W. Kim, J.-H. Ahn, G. Wang, and H.-J. Ahn, "Discharge mechanism of mos2 for sodium ion battery: Electrochemical measurements and characterization," *Electrochimica Acta*, vol. 92, pp. 427–432, 2013.

[144] J. Wan, W. Bao, Y. Liu, J. Dai, F. Shen, L. Zhou, X. Cai, D. Urban, Y. Li, K. Jungjohann, *et al.*, "in situ investigations of li-mos2 with planar batteries," *Advanced Energy Materials*, vol. 5, no. 5, p. 1401742, 2015.

[145] Y. Yu, F. Yang, X. F. Lu, Y. J. Yan, Y.-H. Cho, L. Ma, X. Niu, S. Kim, Y.-W. Son, D. Feng, *et al.*, "Gate-tunable phase transitions in thin flakes of 1t-tas 2," *Nature nanotechnology*, vol. 10, no. 3, pp. 270–276, 2015.

[146] F. Xiong, H. Wang, X. Liu, J. Sun, M. Brongersma, E. Pop, and Y. Cui, "Li intercalation in mos2: in situ observation of its dynamics and tuning optical and electrical properties," *Nano letters*, vol. 15, no. 10, pp. 6777–6784, 2015.

[147] J. Yao, K. J. Koski, W. Luo, J. J. Cha, L. Hu, D. Kong, V. K. Narasimhan, K. Huo, and Y. Cui, "Optical transmission enhacement through chemically tuned two-dimensional bismuth chalcogenide nanoplates," *Nature communications*, vol. 5, no. 1, pp. 1–7, 2014.

[148] Y. Wang, J. Z. Ou, S. Balendhran, A. F. Chrimes, M. Mortazavi, D. D. Yao, M. R. Field, K. Latham, V. Bansal, J. R. Friend, *et al.*, "Electrochemical control of photoluminescence in two-dimensional mos2 nanoflakes," *ACS nano*, vol. 7, no. 11, pp. 10083–10093, 2013.

[149] J. Z. Ou, A. F. Chrimes, Y. Wang, S.-y. Tang, M. S. Strano, and K. Kalantar-zadeh, "Ion-driven photoluminescence modulation of quasi-two-dimensional mos2 nanoflakes for applications in biological systems," *Nano letters*, vol. 14, no. 2, pp. 857–863, 2014.

[150] Y. Gong, H. Yuan, C.-L. Wu, P. Tang, S.-Z. Yang, A. Yang, G. Li, B. Liu, J. van de Groep, M. L. Brongersma, *et al.*, "Spatially controlled doping of two-dimensional sns 2 through intercalation for electronics," *Nature nanotechnology*, vol. 13, no. 4, pp. 294–299, 2018.

[151] J. J. Cha, K. J. Koski, K. C. Huang, K. X. Wang, W. Luo, D. Kong, Z. Yu, S. Fan, M. L. Brongersma, and Y. Cui, "Two-dimensional chalcogenide nanoplates as tunable metamaterials via chemical intercalation," *Nano letters*, vol. 13, no. 12, pp. 5913–5918, 2013.

[152] K. Li, T.-H. Chang, Q. Xie, Y. Cheng, H. Yang, J. Chen, and P.-Y. Chen, "Tunable magnetic response in 2d materials via reversible intercalation of paramagnetic ions," *Advanced Electronic Materials*, vol. 5, no. 6, p. 1900040, 2019.

[153] J. Wang, G. Zhang, and P. Zhang, "Layered birnessite-type mno 2 with surface pits for enhanced catalytic formaldehyde oxidation activity," *Journal of Materials Chemistry A*, vol. 5, no. 12, pp. 5719–5725, 2017.

[154] K. W. Nam, S. Kim, S. Lee, M. Salama, I. Shterenberg, Y. Gofer, J.-S. Kim, E. Yang, C. S. Park, J.-S. Kim, *et al.*, "The high performance of crystal water containing manganese birnessite cathodes for magnesium batteries," *Nano letters*, vol. 15, no. 6, pp. 4071–4079, 2015.

[155] X. Shan, F. Guo, D. S. Charles, Z. Lebens-Higgins, S. A. Razek, J. Wu, W. Xu, W. Yang, K. L. Page, J. C. Neuefeind, *et al.*, "Structural water

and disordered structure promote aqueous sodium-ion energy storage in sodium-birnessite," *Nature communications*, vol. 10, no. 1, pp. 1–11, 2019.

[156] J. E. Post, "Manganese oxide minerals: Crystal structures and economic and environmental significance," *Proceedings of the National Academy of Sciences*, vol. 96, no. 7, pp. 3447–3454, 1999.

[157] H. Zhu, J. Luo, H. Yang, J. Liang, G. Rao, J. Li, and Z. Du, "Birnessite-type mno2 nanowalls and their magnetic properties," *The Journal of Physical Chemistry C*, vol. 112, no. 44, pp. 17089–17094, 2008.

[158] S. Zhu, W. Huo, X. Liu, and Y. Zhang, "Birnessite based nanostructures for supercapacitors: challenges, strategies and prospects," *Nanoscale Advances*, vol. 2, no. 1, pp. 37–54, 2020.

[159] N. Qiu, H. Chen, Z. Yang, S. Sun, and Y. Wang, "Low-cost birnessite as a promising cathode for high-performance aqueous rechargeable batteries," *Electrochimica Acta*, vol. 272, pp. 154–160, 2018.

[160] B. Lin, X. Zhu, L. Fang, X. Liu, S. Li, T. Zhai, L. Xue, Q. Guo, J. Xu, and H. Xia, "Birnessite nanosheet arrays with high k content as a high-capacity and ultrastable cathode for k-ion batteries," *Advanced Materials*, vol. 31, no. 24, p. 1900060, 2019.

[161] X. Zhang, P. Yu, H. Zhang, D. Zhang, X. Sun, and Y. Ma, "Rapid hydrothermal synthesis of hierarchical nanostructures assembled from ultrathin birnessite-type mno2 nanosheets for supercapacitor applications," *Electrochimica Acta*, vol. 89, pp. 523–529, 2013.

[162] H. Xia, X. Zhu, J. Liu, Q. Liu, S. Lan, Q. Zhang, X. Liu, J. K. Seo, T. Chen, L. Gu, *et al.*, "A monoclinic polymorph of sodium birnessite for ultrafast and ultrastable sodium ion storage," *Nature communications*, vol. 9, no. 1, pp. 1–10, 2018.

[163] S. Ching, D. J. Petrovay, M. L. Jorgensen, and S. L. Suib, "Sol- gel synthesis of layered birnessite-type manganese oxides," *Inorganic Chemistry*, vol. 36, no. 5, pp. 883–890, 1997.

[164] S. Ching, S. M. Hughes, T. P. Gray, and E. J. Welch, "Manganese oxide thin films prepared by nonaqueous sol–gel processing: preferential formation of birnessite," *Microporous and mesoporous materials*, vol. 76, no. 1-3, pp. 41–49, 2004.

[165] Y. Liu, D. Yan, R. Zhuo, S. Li, Z. Wu, J. Wang, P. Ren, P. Yan, and Z. Geng, "Design, hydrothermal synthesis and electrochemical properties of porous birnessite-type manganese dioxide nanosheets on graphene as a hybrid material for supercapacitors," *Journal of power sources*, vol. 242, pp. 78–85, 2013.

[166] T. Jakubek, C. Hudy, J. Gryboś, H. Manyar, and A. Kotarba, "Thermal transformation of birnessite (ol) towards highly active cryptomelane (oms-2) catalyst for soot oxidation," *Catalysis Letters*, vol. 149, no. 8, pp. 2218–2225, 2019.

[167] J. Shin, J. K. Seo, R. Yaylian, A. Huang, and Y. S. Meng, "A review on mechanistic understanding of mno2 in aqueous electrolyte for electrical energy storage systems," *International Materials Reviews*, vol. 65, no. 6, pp. 356–387, 2020.

[168] X. Duan, J. Yang, H. Gao, J. Ma, L. Jiao, and W. Zheng, "Controllable hydrothermal synthesis of manganese dioxide nanostructures: shape evolution, growth mechanism and electrochemical properties," *CrystEngComm*, vol. 14, no. 12, pp. 4196–4204, 2012.

[169] B.-R. Chen, W. Sun, D. A. Kitchaev, J. S. Mangum, V. Thampy, L. M. Garten, D. S. Ginley, B. P. Gorman, K. H. Stone, G. Ceder, *et al.*, "Understanding crystallization pathways leading to manganese oxide polymorph formation," *Nature communications*, vol. 9, no. 1, pp. 1–9, 2018.

[170] D. A. Kitchaev, S. T. Dacek, W. Sun, and G. Ceder, "Thermodynamics of phase selection in mno2 framework structures through alkali intercalation and hydration," *Journal of the American Chemical Society*, vol. 139, no. 7, pp. 2672–2681, 2017.

[171] Y. Yuan, K. He, B. W. Byles, C. Liu, K. Amine, J. Lu, E. Pomerantseva, and R. Shahbazian-Yassar, "Deciphering the atomic patterns leading to mno2 polymorphism," *Chem*, vol. 5, no. 7, pp. 1793–1805, 2019.

[172] J. Hao, J. Mou, J. Zhang, L. Dong, W. Liu, C. Xu, and F. Kang, "Electrochemically induced spinel-layered phase transition of mn3o4 in high performance neutral aqueous rechargeable zinc battery," *Electrochimica Acta*, vol. 259, pp. 170–178, 2018.

[173] N. Birkner and A. Navrotsky, "Rapidly reversible redox transformation in nanophase manganese oxides at room temperature triggered by changes in hydration," *Proceedings of the National Academy of Sciences*, vol. 111, no. 17, pp. 6209–6214, 2014.

[174] S. Kim, K. W. Nam, S. Lee, W. Cho, J.-S. Kim, B. G. Kim, Y. Oshima, J.-S. Kim, S.-G. Doo, H. Chang, *et al.*, "Direct observation of an anomalous spinel-to-layered phase transition mediated by crystal water intercalation," *Angewandte Chemie*, vol. 127, no. 50, pp. 15309–15314, 2015.

[175] S. Kim, S. Lee, K. W. Nam, J. Shin, S. Y. Lim, W. Cho, K. Suzuki, Y. Oshima, M. Hirayama, R. Kanno, *et al.*, "On the mechanism of crystal water insertion during anomalous spinel-to-birnessite phase transition," *Chemistry of Materials*, vol. 28, no. 15, pp. 5488–5494, 2016.

[176] Y. Omomo, T. Sasaki, L. Wang, and M. Watanabe, "Redoxable nanosheet crystallites of mno2 derived via delamination of a layered manganese oxide," *Journal of the American Chemical Society*, vol. 125, no. 12, pp. 3568–3575, 2003.

[177] M. Tu, H. Lu, S. Luo, H. Peng, S. Li, Y. Ke, S. Yuan, W. Huang, W. Jie, and J. Hao, "Reversible transformation between bipolar memory switching and bidirectional threshold switching in 2d layered k-birnessite nanosheets," *ACS applied materials & interfaces*, vol. 12, no. 21, pp. 24133–24140, 2020.

[178] Z. Liu, R. Ma, Y. Ebina, K. Takada, and T. Sasaki, "Synthesis and delamination of layered manganese oxide nanobelts," *Chemistry of Materials*, vol. 19, no. 26, pp. 6504–6512, 2007.

[179] K. P. Lucht and J. L. Mendoza-Cortes, "Birnessite: A layered manganese oxide to capture sunlight for water-splitting catalysis," *The Journal of Physical Chemistry C*, vol. 119, no. 40, pp. 22838–22846, 2015.

[180] W. Xiao, D. Wang, and X. W. Lou, "Shape-controlled synthesis of mno2 nanostructures with enhanced electrocatalytic activity for oxygen reduction," *The Journal of Physical Chemistry C*, vol. 114, no. 3, pp. 1694–1700, 2010.

[181] V. A. Drits, E. Silvester, A. I. Gorshkov, and A. Manceau, "Structure of synthetic monoclinic na-rich birnessite and hexagonal birnessite: I. results from x-ray diffraction and selected-area electron diffraction," *American Mineralogist*, vol. 82, no. 9-10, pp. 946–961, 1997.

[182] X. Chen, S. Yan, N. Wang, S. Peng, C. Wang, Q. Hong, X. Zhang, and S. Dai, "Facile synthesis and characterization of ultrathin delta-mno 2 nanoflakes," *RSC advances*, vol. 7, no. 88, pp. 55734–55740, 2017.

[183] C. Julien, M. Massot, R. Baddour-Hadjean, S. Franger, S. Bach, and J. Pereira-Ramos, "Raman spectra of birnessite manganese dioxides," *Solid State Ionics*, vol. 159, no. 3-4, pp. 345–356, 2003.

[184] V. Di Castro and G. Polzonetti, "Xps study of mno oxidation," *Journal of Electron Spectroscopy and Related Phenomena*, vol. 48, no. 1, pp. 117–123, 1989.

[185] P. Gao, P. Metz, T. Hey, Y. Gong, D. Liu, D. D. Edwards, J. Y. Howe, R. Huang, and S. T. Misture, "The critical role of point defects in improving the specific capacitance of δ-mno 2 nanosheets," *Nature communications*, vol. 8, no. 1, pp. 1–10, 2017.

[186] S. Dang, Y. Wen, T. Qin, J. Hao, H. Li, J. Huang, D. Yan, G. Cao, and S. Peng, "Nanostructured manganese dioxide with adjustable mn3+/mn4+ ratio for flexible high-energy quasi-solid supercapacitors," *Chemical Engineering Journal*, vol. 396, p. 125342, 2020.

[187] M. Nakayama, S. Konishi, H. Tagashira, and K. Ogura, "Electrochemical synthesis of layered manganese oxides intercalated with tetraalkylammonium ions," *Langmuir*, vol. 21, no. 1, pp. 354–359, 2005.

[188] H. Nesbitt, G. Canning, and G. Bancroft, "Xps study of reductive dissolution of 7å-birnessite by h3aso3, with constraints on reaction mechanism," *Geochimica et Cosmochimica Acta*, vol. 62, no. 12, pp. 2097–2110, 1998.

[189] A. Gao, M. Li, N. Guo, D. Qiu, Y. Li, S. Wang, X. Lu, F. Wang, and R. Yang, "K-birnessite electrode obtained by ion exchange for potassium-ion batteries: Insight into the concerted ionic diffusion and k storage mechanism," *Advanced Energy Materials*, vol. 9, no. 1, p. 1802739, 2019.

[190] E. S. Ilton, J. E. Post, P. J. Heaney, F. T. Ling, and S. N. Kerisit, "Xps determination of mn oxidation states in mn (hydr) oxides," *Applied Surface Science*, vol. 366, pp. 475–485, 2016.

[191] M. Oku, K. Hirokawa, and S. Ikeda, "X-ray photoelectron spectroscopy of manganese—oxygen systems," *Journal of Electron Spectroscopy and Related Phenomena*, vol. 7, no. 5, pp. 465–473, 1975.

[192] R. Giovanoli, E. Stähli, and W. Feitknecht, "Über oxidhydroxide des vierwertigen mangans mit schichtengitter 2. mitteilung: Mangan (iii)-manganat (iv)," *Helvetica Chimica Acta*, vol. 53, no. 3, pp. 453–464, 1970.

[193] J. E. Post and D. R. Veblen, "Crystal structure determinations of synthetic sodium, magnesium, and potassium birnessite using tem and the rietveld method," *American Mineralogist*, vol. 75, no. 5-6, pp. 477–489, 1990.

[194] A. Manceau, A. I. Gorshkov, and V. A. Drits, "Structural chemistry of mn, fe, co, and ni in manganese hydrous oxides: Part ii. information from exafs spectroscopy and electron and x-ray diffraction," *American Mineralogist*, vol. 77, no. 11-12, pp. 1144–1157, 1992.

[195] S. Zhu, L. Li, J. Liu, H. Wang, T. Wang, Y. Zhang, L. Zhang, R. S. Ruoff, and F. Dong, "Structural directed growth of ultrathin parallel birnessite on β-mno2 for high-performance asymmetric supercapacitors," *ACS nano*, vol. 12, no. 2, pp. 1033–1042, 2018.

[196] J. Wang, Y. Dang, A. G. Meguerdichian, S. Dissanayake, T. Kankanam-Kapuge, S. Bamonte, Z. M. Tobin, L. A. Achola, and S. L. Suib, "Water harvesting from the atmosphere in arid areas with manganese dioxide," *Environmental Science & Technology Letters*, vol. 7, no. 1, pp. 48–53, 2019.

[197] C. Li, A. Guerrero, Y. Zhong, A. Gräser, C. A. M. Luna, J. Köhler, J. Bisquert, R. Hildner, and S. Huettner, "Real-time observation of iodide ion migration in methylammonium lead halide perovskites," *Small*, vol. 13, no. 42, p. 1701711, 2017.

[198] M. Sha, L. Liu, H. Zhao, and Y. Lei, "Review on recent advances of cathode materials for potassium-ion batteries," *Energy & Environmental Materials*, vol. 3, no. 1, pp. 56–66, 2020.

[199] J. C. Chacon-Torres, L. Wirtz, and T. Pichler, "Manifestation of charged and strained graphene layers in the raman response of graphite intercalation compounds," *ACS nano*, vol. 7, no. 10, pp. 9249–9259, 2013.

[200] M. R. Jo, Y. Kim, J. Yang, M. Jeong, K. Song, Y.-I. Kim, J.-M. Lim, M. Cho, J.-H. Shim, Y.-M. Kim, *et al.*, "Triggered reversible phase transformation between layered and spinel structure in manganese-based layered compounds," *Nature communications*, vol. 10, no. 1, pp. 1–9, 2019.

[201] E. Yang, H. Kim, S. Kim, I. Kim, J. Kim, H. Ji, J. W. Choi, and Y. Jung, "Origin of unusual spinel-to-layered phase transformation by crystal water," *Chemical science*, vol. 9, no. 2, pp. 433–438, 2018.

[202] J. Zuo, C. Xu, Y. Liu, and Y. Qian, "Crystallite size effects on the raman spectra of mn3o4," *Nanostructured materials*, vol. 10, no. 8, pp. 1331–1335, 1998.

[203] S. Royer and D. Paré, "Conservation of total synaptic weight through balanced synaptic depression and potentiation," *Nature*, vol. 422, no. 6931, pp. 518–522, 2003.

[204] H. Han, H. Yu, H. Wei, J. Gong, and W. Xu, "Recent progress in three-terminal artificial synapses: from device to system," *Small*, vol. 15, no. 32, p. 1900695, 2019.

[205] D. Kuzum, S. Yu, and H. P. Wong, "Synaptic electronics: materials, devices and applications," *Nanotechnology*, vol. 24, no. 38, p. 382001, 2013.

[206] Y. Li, Z. Wang, R. Midya, Q. Xia, and J. J. Yang, "Review of memristor devices in neuromorphic computing: materials sciences and device challenges," *Journal of Physics D: Applied Physics*, vol. 51, no. 50, p. 503002, 2018.

[207] Y. Tang, J. R. Nyengaard, D. M. De Groot, and H. J. G. Gundersen, "Total regional and global number of synapses in the human brain neocortex," *Synapse*, vol. 41, no. 3, pp. 258–273, 2001.

[208] H. Liu, G. Qi, C. Tang, M. Chen, Y. Chen, Z. Shu, H. Xiang, Y. Jin, S. Wang, H. Li, *et al.*, "Growth of large-area homogeneous monolayer transition-metal disulfides via a molten liquid intermediate process," *ACS applied materials & interfaces*, vol. 12, no. 11, pp. 13174–13181, 2020.

[209] H. Li, P. Li, J.-K. Huang, M.-Y. Li, C.-W. Yang, Y. Shi, X.-X. Zhang, and L.-J. Li, "Laterally stitched heterostructures of transition metal dichalcogenide: chemical vapor deposition growth on lithographically patterned area," *ACS nano*, vol. 10, no. 11, pp. 10516–10523, 2016.

[210] F. Lu, A. Karmakar, S. Shahi, and E. Einarsson, "Selective and confined growth of transition metal dichalcogenides on transferred graphene," *RSC advances*, vol. 7, no. 59, pp. 37310–37314, 2017.

[211] E. Brézin, J. Le Guillou, and J. Zinn-Justin, "Phase transitions and critical phenomena," *Domb and hi-S-Green Eds.(Acadeiuic, New York, 197G) Vol*, vol. 5, pp. 90197–4, 1976.

[212] S. Dai, Z. Fei, Q. Ma, A. Rodin, M. Wagner, A. McLeod, M. Liu, W. Gannett, W. Regan, K. Watanabe, *et al.*, "Tunable phonon polaritons in atomically thin van der waals crystals of boron nitride," *Science*, vol. 343, no. 6175, pp. 1125–1129, 2014.

[213] A. M. Dubrovkin, B. Qiang, H. N. Krishnamoorthy, N. I. Zheludev, and Q. J. Wang, "Ultra-confined surface phonon polaritons in molecular layers

of van der waals dielectrics," *Nature communications*, vol. 9, no. 1, pp. 1–6, 2018.

[214] T. G. Folland, A. Fali, S. T. White, J. R. Matson, S. Liu, N. A. Aghamiri, J. H. Edgar, R. F. Haglund, Y. Abate, and J. D. Caldwell, "Reconfigurable infrared hyperbolic metasurfaces using phase change materials," *Nature communications*, vol. 9, no. 1, pp. 1–7, 2018.

[215] O. Çakıroğlu, N. Mehmood, M. M. Çiçek, A. Aikebaier, H. R. Rasouli, E. Durgun, and T. S. Kasırga, "Thermal conductivity measurements in nanosheets via bolometric effect," *2D Materials*, vol. 7, no. 3, p. 035003, 2020.

[216] V. Andreev, F. Chudnovskij, A. Petrov, and E. Terukov, "Thermal conductivity of vo 2, v 3 o 5, and v 2 o 3," *Physica Status Solidi. A, Applied Research*, vol. 48, no. 2, pp. K153–K156, 1978.

[217] T. Lavra, L. Silva, K. Cavalcante, K. Marinho, B. Figueira, and J. Mercury, "Microwave radiation influence on the thermal and spectroscopic properties of na-birnessite-type material," *Cerâmica*, vol. 65, no. 376, pp. 547–553, 2019.

[218] L. M. Vogl, P. Schweizer, M. Wu, and E. Spiecker, "Transforming layered mos 2 into functional moo 2 nanowires," *Nanoscale*, vol. 11, no. 24, pp. 11687–11695, 2019.